POLITECNICO DI TORINO

Master's Degree in Agritech Engineering

Politecnico di Torino

Master's Degree Thesis

Laboratory Evaluation of a Low-Cost Metal Oxide Sensor Platform for Monitoring Herbivore Induced VOCs in Maize

Supervisors

Prof. Danilo DEMARCHI

Dr. Umberto GARLANDO

Dr. Ralph STOOP

Dr. Camilo CHIANG

Dr. Dani LUCAS-BARBOSA

Candidate

Saverio FRANDINO

December 2025

Abstract

Early detection of plant stress and pest infestation is a key enabler of sustainable and precise crop management. Volatile organic compounds (VOCs) emitted by plants provide a valuable, non-invasive means of monitoring physiological changes, yet their implementation in real-time sensing remains limited by the high cost, complexity, and laboratory confinement of conventional analytical methods such as GC-MS (Gas Chromatography–Mass Spectrometry).

This thesis investigates the potential of a low-cost MOS (Metal Oxide Semiconductor) gas sensor platform for detecting plant-emitted VOCs under controlled laboratory conditions. The system was tested across two main experiments designed to characterize the sensor response to biological volatile emissions. A preliminary validation was performed using sheep wool samples to assess system performance and stability under known conditions. The main experiment involved maize (*Zea mays* L.) plants subjected to herbivory by larvae of *Spodoptera littoralis* (Boisduval), a polyphagous lepidopteran pest widely used in studies of herbivore-induced plant volatiles. The experimental setup allowed simultaneous monitoring of eight plants for approximately twenty-four hours, including a two-hour period of dynamic headspace collection for GC-MS analysis.

The results demonstrate that the tested MOS sensors can qualitatively detect the presence of plant-emitted VOC under herbivory. Although the sensor signals did not allow for discrimination of individual compounds, clear differences in response magnitude were observed between plants exhibiting high and low VOC emissions, as confirmed by GC-MS. This indicates that commercial MOS sensors are sensitive enough to capture large variations in volatile release associated with biotic stress, even without chemical selectivity. The responses were highly dependent on the degree of feeding activity and overall VOC concentration, highlighting the need for improved control of biological variability in future experiments.

While GC-MS remains indispensable for compound identification, this study demonstrates that low-cost MOS sensors can serve as portable, complementary tools for real-time plant monitoring. Their affordability and simplicity make them promising candidates for integration into distributed sensing networks for greenhouse or field-scale applications. The work establishes an experimental and methodological foundation for future development of low-cost electronic systems aimed at early detection of plant stress through continuous monitoring of volatile emissions, contributing to the broader vision of precision and data-driven agriculture.

ACKNOWLEDGMENTS

I would like to express my sincere gratitude to Agroscope for hosting me during the development of this thesis. Working within the Digital Production group has been an invaluable experience, and I am deeply thankful for the opportunity to conduct my research in such a stimulating and supportive environment.

I am extremely grateful to Dr. Ralph Stoop for his guidance, scientific input, and continuous support throughout this work. His steady assistance during my stay made a decisive difference, and I appreciate the trust and autonomy he gave me in navigating the project.

I am equally indebted to Dr. Camilo Chiang, whose passion and knowledge helped me grow, both academically and personally. His ideas, critical perspective, and encouragement pushed me to approach problems from new angles and laid the foundations for my future development. The expertise and enthusiasm of both Ralph and Camilo shaped this project at every stage, from experimental design to data interpretation.

This endeavor would not have been possible without Dr. Dani Lucas Barbosa (FiBL and University of Zurich) and her essential support with the chemical analyses, laboratory procedures, and GC–MS work. Her expertise in chemical ecology and analytical workflows was fundamental to the success of this thesis.

I would also like to thank all colleagues in Tänikon for contributing to a fantastic working environment and for making me feel welcomed, included, and supported during my stay. In particular, I am grateful to Dr. Thomas Anker and Dr. Michael Simmler for their guidance and help across the many aspects of the project.

I am also thankful to Valentin, Karina, and Olga for their warm presence during my time in Tänikon. Their company made daily life more enjoyable and helped me feel at home.

Finally, I am deeply grateful to my family and friends for their unwavering support. My parents and my girlfriend Matilde have encouraged me throughout this journey and have been a constant source of motivation. I also want to thank my brother Sebastiano, who helped me settle into life in Switzerland while I was working on this thesis and whose presence made that transition much smoother.

Table of Contents

List of Figures

Acronyms

VOC	Volatile Organic Compound
HIPV	Herbivore Induced Plant Volatile
GLV	Green Leaf Volatile
DMNT	(*E*)-4,8-dimethyl-1,3,7-nonatriene
MeSA	Methyl Salicylate
JA	Jasmonic Acid
GC	Gas Chromatography
GC-MS	Gas Chromatography–Mass Spectrometry
PTR-TOF-MS	Proton Transfer Reaction–Time of Flight–Mass Spectrometry
AI	Arithmetic retention Indices
MOS	Metal Oxide Semiconductor
SMON	Semiconductor Metal Oxide Nanostructure
CNT	Carbon Nanotube
rGO	Reduced Graphene Oxide
TCO	Temperature-cycled Operation

DSR	Differential Surface Reduction
PTFE	Polytetrafluoroethylene
RPi	Raspberry Pi
SBC	Single Board Computer
I^2C	Inter Integrated Circuit
CSV	Comma Separated Value
SSH	Secure Shell
NTP	Network Time Protocol
CRC	Cyclic Redundancy Check
IoT	Internet of Things
PCB	Printed Circuit Board
IPM	Integrated Pest Management
FAO	Food and Agriculture Organization of the United Nations
RH	Relative Humidity

Chapter 1

Introduction

Agriculture, the foundation of human survival and economic stability, faces increasing threats from pests and plant diseases that cause global yield losses of 20–40% annually [1, 2, 3, 4]. Climate change, agricultural intensification, and globalization further exacerbate these risks by facilitating pest proliferation and the spread of invasive species such as the fall armyworm (*Spodoptera frugiperda*), responsible for an estimated USD 9.4 billion in annual damage across Africa [2].

The widespread use of synthetic pesticides has become environmentally unsustainable, leading to soil and water contamination, pest resistance, and the decline of pollinators. A shift toward sustainable and eco-friendly crop protection is therefore essential [5, 3].

Plants possess diverse intrinsic defense mechanisms against pests. Central to these are VOCs, airborne compounds that mediate ecological communication and defense signaling, often referred to as semiochemicals [6]. Because VOC emissions can reveal early physiological changes before visible symptoms appear, they offer a promising, non-invasive basis for sustainable IPM strategies [7, 5]. Many stress-induced emissions occur rapidly and transiently (over minutes to hours) which means that continuous, high-temporal-resolution monitoring is crucial for early detection.

Despite the rapid growth of VOC-based plant diagnostics, the translation of laboratory findings into practical agricultural tools remains limited. Conventional analytical technologies provide unparalleled chemical resolution but fall short of operational requirements in the field. GC-MS remains the gold standard for comprehensive VOC profiling, while PTR-TOF-MS enables real-time, high-sensitivity detection [7]. However, both are costly, bulky, and require specialized infrastructure. Even “portable” GC-MS units weigh 15–20 kg, have high power demands, and rely on complex, discrete sampling workflows spanning hours to days [8]. These constraints prevent continuous monitoring and make them unsuitable for integration into precision agriculture or dense sensor networks. As a result, VOC detection

remains largely confined to centralized laboratories [9].

To bridge this gap, there is growing interest in low-cost, miniaturized gas sensors capable of continuous, in-situ detection. Among the available portable sensing technologies, MOS gas sensors are particularly appealing due to their low cost, compactness, and compatibility with battery-powered or embedded systems. Their sensitivity to a wide range of reducing gases makes them strong candidates for monitoring the complex volatilome emitted by plants. However, MOS sensors also present well-known challenges: limited chemical selectivity, strong cross-sensitivities to humidity and temperature, sensor drift, and nonlinear response behavior. Their output reflects broad chemical classes rather than individual compounds, meaning they capture the integrated "fingerprint" of the emitted VOCs blend rather than its detailed molecular composition [10]. Understanding these limitations is essential before deploying them in real agricultural environments.

More generally, the development of field-ready VOC sensing technologies faces several interconnected challenges:

Environmental and Biological Complexity
: Plant VOC emissions are highly sensitive to environmental drivers such as light, temperature, humidity, and atmospheric oxidants (e.g., ozone, NOx), which can rapidly degrade reactive volatiles [9]. Biological factors—including plant genotype, developmental stage, and the nature and timing of herbivory—produce large natural variability [11]. This variability complicates both sensor calibration and the identification of stress-specific signatures.

Selectivity
: Miniaturized sensors, including MOS devices and electronic noses, often struggle to distinguish specific target VOC within the highly complex plant volatilome. Many VOCs share similar reducing properties and produce overlapping responses, leading to low chemical specificity and interfering background signals [10]. Effective sensing therefore relies on capturing multi-dimensional response patterns rather than targeting individual molecules, which requires careful control of environmental conditions.

Data Analysis and Modeling
: Plant VOCs signals are chemically diverse, nonlinear, and heavily influenced by external conditions. Building robust, transferable models requires large, well-curated datasets and the application of multivariate statistics or machine learning [12]. However, the lack of standardized calibration mixtures and the strong dependence on experimental setup often limit reproducibility across studies and sensor platforms [13].

Because MOS sensors are intrinsically sensitive to environmental variables and prone to cross-sensitivities, a controlled experimental approach is essential as a

first step toward evaluating their suitability for VOC-based plant monitoring. Conducting experiments under stable and reproducible conditions allows the intrinsic sensor behavior to be characterized independently of atmospheric variability. Furthermore, coupling the sensor platform with a reference GC-MS system provides complementary chemical information: not to calibrate the sensor to individual compounds, but to confirm the presence and relative trends of plant-emitted VOCs, enabling more informed interpretation of sensor responses.

This work aims to contribute to the development of inexpensive, portable systems for continuous, non-invasive, and high-resolution monitoring of plant VOC. The long-term vision is to establish a foundational understanding of how low-cost MOS sensors respond to plant emissions, with the goal of enabling "smart farming" tools that provide timely, data-driven information to growers and support early intervention before visible damage occurs. By characterizing sensor performance under controlled conditions and comparing it with GC-MS measurements, this thesis evaluates the feasibility of using MOS sensors as a low-cost platform for real-time assessment of plant physiological status.

Chapter 2

Background

2.1 Metal Oxide Semiconductor (MOS) gas sensors

Metal–oxide semiconductor (MOS) gas sensors are among the most widely used technologies for low-cost VOC detection. Their operation relies on the interaction between gas molecules and the surface of a heated semiconducting oxide, where chemical reactions modulate the electrical conductivity of the material. Despite their simplicity and high sensitivity, these devices exhibit limitations such as poor selectivity, humidity dependence, and long-term drift. This section introduces the working principles, material considerations, operating modes, and performance characteristics of MOS sensors, providing the conceptual basis for interpreting the experimental results presented in this thesis.

2.1.1 Operating Principle

MOS sensors constitute a class of resistive gas sensors first introduced by Seiyama *et al.* using ZnO [14], and later commercialized by Taguchi using SnO_2. Their transduction mechanism originates from temperature-activated reactions occurring at the semiconductor surface, where gas adsorption influences charge transport.

When an n-type oxide such as SnO_2 is heated in air (typically 200 °C to 400 °C), oxygen molecules adsorb onto the surface and withdraw electrons from the semiconductor's conduction band. This process forms ionosorbed oxygen species, including O_2^-, O^-, and O^{2-}, whose relative abundance depends strongly on temperature [15]. At ∼150 °C, the dominant form is molecular O_2^-, while above 300 °C more reactive atomic species O^- and O^{2-} prevail.

Space-charge region and semiconductor physics

The withdrawal of electrons leads to the formation of a *space-charge region*, a concept central to semiconductor physics. The space-charge region describes the portion of the semiconductor in which mobile charge carriers have been depleted or rearranged, creating an internal electric field. In n-type oxides, this forms a depletion layer, characterized by a reduced concentration of free electrons.

Depending on the surface conditions and dopants, the surface region may also exhibit:

- **Accumulation**: an excess of majority carriers at the surface,
- **Inversion**: a surface layer where minority carriers dominate.

These regimes are well described in classical models by Madou and Morrison [16]. The band bending effects associated with depletion, and accumulation are illustrated schematically in Figure 2.1, which shows the electronic structure of n- and p-type semiconducting metal oxides under exposure to reducing gases.

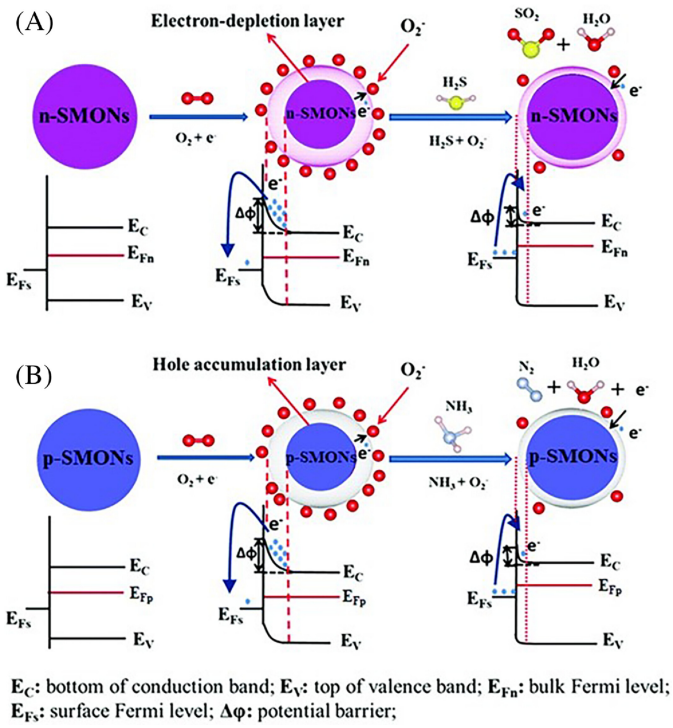

Figure 2.1: Gas sensing mechanism of (A) n- and (B) p-type semiconducting metal oxide nanostructures SMONs upon exposure of reducing gases [17, 18].

The position of the *Fermi level*, the electrochemical potential of electrons in the material, determines the distribution of electrons in the bands and strongly

influences the sensor's electrical response. Adsorption of oxygen or analyte gases perturbs the Fermi level, modulating the width of the space-charge region and thus the resistance.

Sensor structure and grain boundaries

In practical devices, the sensitive layer of a MOS sensor is a polycrystalline or nanocrystalline film deposited on an insulating substrate equipped with interdigitated electrodes and an integrated heater [15, 17, 19]. This film is composed of many small crystallites, or *grains*, typically in the nano- to micrometre range, separated by grain boundaries. In n-type oxides such as SnO_2, adsorption of oxygen on the grain surfaces creates depletion layers that extend into each grain. As a result, electrical conduction is largely controlled by the potential barriers that form at the grain boundaries, i.e. the *inter-grain* regions through which electrons must pass to contribute to the measured conductivity [15, 20].

Reaction with target gases

When a reducing gas (e.g. H_2, CO, hydrocarbons, or plant-emitted VOC) contacts the heated surface, it reacts with the ionosorbed oxygen species. This reaction releases the previously trapped electrons back into the conduction band, narrowing the depletion region and lowering the potential barriers at the grain boundaries (inter-grain barriers). As a result, the conductivity increases.

Conversely, oxidizing gases withdraw additional electrons, thickening the depletion region and reducing conductivity. The magnitude of this change depends on the gas concentration, surface catalytic activity, and operating temperature [17]. A simplified representation of these surface processes is shown in Figure 2.2, highlighting the ionosorption of oxygen and its reaction with incoming reducing gases.

Microstructure and conduction regimes

The sensitivity and dynamic behavior of a MOS sensor depend strongly on the microstructure of the sensing material. A critical parameter is the ratio between the grain size x_g and the Debye length λ_D, the characteristic length scale of the space-charge region [15]:

- **Large grains** ($x_g \gg \lambda_D$): only a thin shell near the surface is depleted; conduction is dominated by grain-boundary barriers.
- **Small grains or nanomaterials** ($x_g \lesssim \lambda_D$): the depletion region spans the entire grain, so even small perturbations to surface charge dramatically affect conductivity.

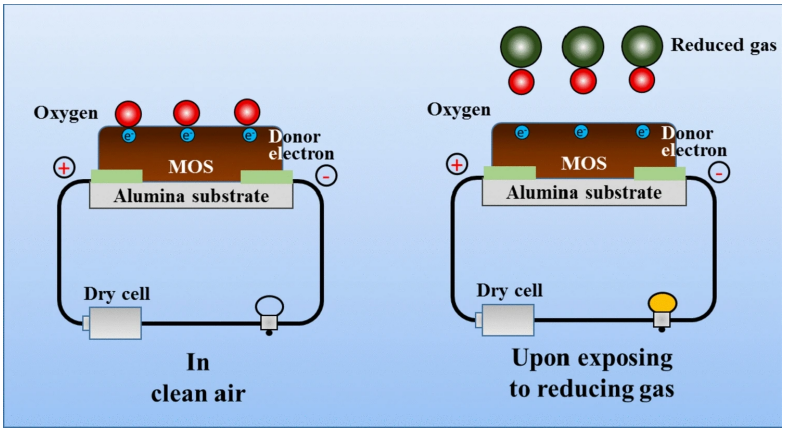

Figure 2.2: Mechanism of oxygen ionosorption and reaction of VOC on an n-type MOS surface [19].

This explains why nanostructured films, nanowires, and mesoporous oxides exhibit superior sensitivity [20, 17].

2.1.2 Material engineering strategies

The sensing performance can be greatly enhanced through purposeful modification of the oxide surface or bulk.

Catalysts and surface modifiers.

Noble metals such as Pt, Pd, or Au are often added to SnO_2 to promote selective reactions. Their effects arise through two principal mechanisms [16, 20]:

1. **Spillover effect**: gas molecules dissociate on the catalyst and migrate ("spill over") onto the oxide, lowering reaction activation energies.

2. **Fermi-level control**: nanoscale catalysts pin the semiconductor's Fermi level locally, modulating the space-charge region as the catalyst's work function shifts under gas exposure.

Catalyst choice tunes the surface kinetics and selectivity toward specific gases. For example, Pt and Pd enhance response to H_2 and CO, whereas Au or CuO improve performance towards sulfur-containing gases [20]. Of particular relevance for plant-stress detection, SnO_2/MXene composites have recently demonstrated high selectivity to methyl jasmonate, a key herbivory-related VOC [21].

Bulk doping and nanocomposites.

Bulk doping refers to the intentional incorporation of foreign atoms into the crystal lattice of the metal oxide. Unlike surface catalysts, which primarily modify reaction kinetics at the surface, bulk dopants alter the intrinsic electronic structure and microstructure of the oxide [16, 20]. Donor-type dopants (e.g. Sb^{5+} in SnO_2) increase the free-electron concentration and shift the Fermi level, influencing the width of the depletion layer and the baseline resistance. Such dopants also accelerate oxygen adsorption kinetics and can improve response and recovery behaviour [20].

Dopants play a crucial role in microstructural control. During high-temperature annealing, they may inhibit grain growth, promote the formation of thermally stable nanocrystalline structures, and increase porosity. Since maximum gas sensitivity occurs when the grain size is comparable to the Debye length, dopant-induced suppression of grain coarsening is a key optimisation strategy [15, 20]. A practical limitation is the narrow concentration range for effective doping: optimal sensing improvements typically occur at additive levels below $1-2\%$, whereas larger concentrations (5–10%) may stabilise the microstructure but degrade sensitivity by introducing recombination sites or excessive electronic screening [20].

Nanocomposite strategies further enhance sensing performance by creating hybrid materials that combine metal oxides with additional functional components. These approaches exploit interfacial charge-transfer phenomena, catalytic synergy, and enhanced adsorption sites.

- **Heterojunction formation.** Composites formed from two semiconductors with different Fermi levels (e.g. p–n or n–n junctions) exhibit charge transfer across the interface until equilibrium is reached, producing a depletion region highly sensitive to gas exposure. Heterojunction-based improvements in sensitivity, selectivity, and kinetics are widely documented in multi-oxide sensors [20]. A representative example is the CuO/MoS_2 composite, where exposure to H_2S induces the conversion of CuO into metallic CuS, collapsing the p–n junction and creating a large conductivity change [20].

- **Integration with carbon nanomaterials.** Carbon nanotubes CNTs and rGO (Reduced Graphene Oxide) provide high electrical conductivity, large surface area, and additional adsorption sites. Their incorporation improves response speed and enhances charge transfer between the adsorbed gas species and the oxide. CNT–oxide nanocomposites such as SnO_2/CNT and SnO_2/rGO hybrids are reported to improve sensitivity and reduce operating temperature, particularly for oxidizing gases such as NO_2 [20]. These composites also mitigate grain agglomeration and promote efficient percolation pathways for electrons.

- **Hybridization with two-dimensional materials.** Transition metal dichalcogenides (TMDs), including MoS_2, introduce highly accessible edge sites and layered structures that facilitate selective adsorption and rapid charge transfer. Their use as supporting matrices in MOS composites enhances both sensitivity and environmental stability by preventing nanoparticle agglomeration and providing additional conduction channels [20].
- **Noble metal functionalisation of nanostructures.** Noble metals can be incorporated not only as bulk dopants but also as surface decorations on nanowires, nanofibres, or nanosheets. These systems combine catalytic activation with modifications to local band alignment. Pd-functionalised SnO_2 nanowires, Au-decorated WO_3 nanofibres, and similar hybrid nanostructures show large enhancements in sensitivity and selectivity [17]. In the context of plant-related VOC monitoring, noble-metal-functionalised oxides have demonstrated strong responses to compounds such as methyl salicylate and methyl jasmonate [22, 21].

2.1.3 Morphology and device architecture

The morphology of the sensing film strongly affects sensitivity, stability, and reproducibility:

- **Thick films** (screen-printed or sintered): easy to fabricate but dominated by grain-boundary conduction.
- **Thin films**: improved homogeneity and lower power consumption.
- **1D nanostructures**: high surface-to-volume ratio, fast response, but challenging fabrication [20].

In systems coupled to GC or controlled-flow sampling, chamber design is critical: dead volume must be minimized to avoid peak broadening, and oxygen supply must remain constant to sustain the sensing reaction [23, 24].

2.1.4 Performance

MOS sensors are typically evaluated based on sensitivity, selectivity, transient response, stability, and operating temperature [17, 19].

Sensitivity and selectivity

Sensitivity describes how strongly the sensor's resistance changes in response to a gas. It is often expressed as:

$$S = \frac{R_g}{R_a}, \qquad S = \frac{R_a}{R_g}, \qquad S = \frac{\Delta R}{R_a}, \qquad S = \frac{\Delta R}{R_g},$$

where R_a is the baseline resistance, R_g the resistance under gas exposure, and

$$\Delta R = |R_g - R_a|.$$

Selectivity remains the principal weakness of MOS technology. Because many reducing gases interact similarly with surface oxygen, responses to different analytes often overlap. This is especially problematic in plant headspaces, where complex mixtures of VOCs are emitted with high variability [9].

Transient response

Response time (t_{90}) is the duration required for the signal to reach 90 % of its total change upon exposure. **Recovery time** is the corresponding duration needed after removal of the analyte. Both depend on adsorption/desorption kinetics, diffusion through the porous film, and operating temperature.

Stability and drift

Long-term stability is critical for field deployment. MOS sensors suffer from drift due to:

- **Grain growth and sintering** at high temperature [18];
- **Chemical poisoning** by siloxanes or sulfur species [13];
- **Bulk diffusion** and irreversible reactions [16];
- **Surface hydration** in humid environments [13].

In addition to physical drift, MOS sensors exhibit considerable sensor-to-sensor variability, requiring individual calibration. Recent advances use machine learning, transfer learning, and drift-resistant features to reduce calibration burden and improve long-term robustness [25].

Operating temperature and advanced modes

Operating temperature regulates the dominant surface oxygen species, the reaction rates, and the overall sensitivity of the sensor [26]. High-temperature "burn-off" cycles are often employed to desorb contaminants and restore surface reactivity.

Modern microhotplates enable TCO (Temperature-cycled Operation), where the sensor temperature is modulated over time according to a predefined waveform.

Each gas exhibits characteristic kinetic behavior during these temperature transitions, producing a time-dependent resistance "fingerprint" [12, 27]. TCO therefore transforms a single sensing element into a *virtual sensor array*, greatly improving selectivity—especially when combined with machine-learning analysis [10, 28].

A particularly powerful TCO method is the DSR (Differential Surface Reduction) approach introduced by Baur et al. The key idea is to exploit the non-equilibrium surface state generated after a rapid temperature jump. As illustrated in Figure 2.3a, the sequence proceeds as follows:

1. At equilibrium state (1), the sensor is held at a low temperature with relatively weak surface oxidation and low negative surface charge.

2. A rapid heating step to a high temperature, e.g. 400 °C (1→2), causes an instantaneous increase in conductance due to the temperature rise, while the surface population of adsorbed oxygen remains nearly unchanged.

3. During the subsequent relaxation at high temperature (2→3), rapid oxidation occurs: highly reactive oxygen species form on the surface, increasing the surface occupation and lowering conductance.

4. An abrupt cooling step (3→4) transfers this highly oxidized surface population to a low-temperature regime. The surface now has an *excess negative charge* compared to the low-temperature equilibrium.

At this point (state 4), the surface is in its most reduction-sensitive non-equilibrium state: reduction reactions with incoming reducing gases (e.g. H_2, CO, or plant-emitted VOCs) strongly dominate over further oxidation. For a short duration, the time derivative of the logarithmic conductance is directly proportional to the rate constant of surface reduction:

$$\frac{d \ln G}{dt} \propto k(t),$$

and at low concentrations the rate constant is proportional to the gas concentration [29]. This enables very sensitive detection of short gas pulses.

The implications for analytical systems such as GC are shown schematically in Figure 2.3b. A temperature jump from high to low temperature produces a characteristic relaxation curve in $\ln G$. When several concentration peaks with different widths but identical total dosage (concentration–time integral) pass over the sensor, their relaxation curves differ in slope but yield the same integrated shift in $\ln G$. Thus, under TCO operation the sensor output becomes directly proportional to the total gas dosage, enabling quantitative peak integration for short GC pulses [30].

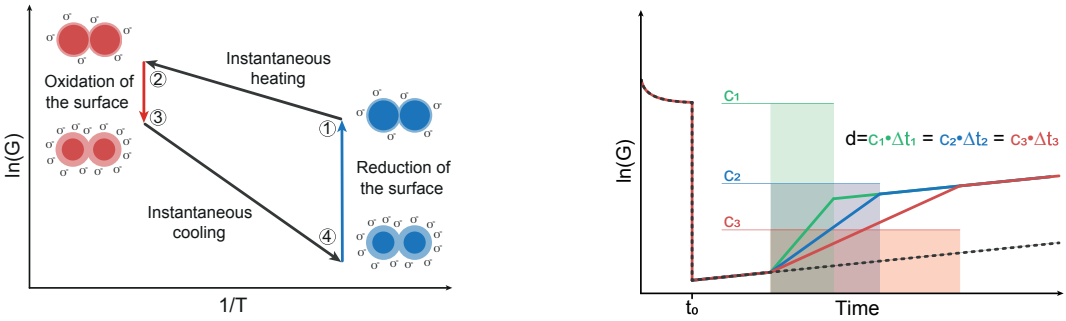

(a) Arrhenius plot illustrating the non-equilibrium states during a rapid temperature cycle.

(b) Conductance relaxation curves after a temperature drop for peaks of equal dosage but different width.

Figure 2.3: Illustration of TCO-based non-equilibrium operation in a MOS sensor. (a) Rapid heating and cooling drive the sensor into distinct non-equilibrium surface states, enabling differential surface reduction. (b) During the low-temperature relaxation phase, the slope of $\ln G$ encodes the concentration of reducing gases, and the integrated shift is proportional to the total gas dosage. Adapted from [31, 30].

Beyond controlled laboratory demonstrations, the practical applicability of TCO-based operation has been validated in real sensor systems. In particular, Koehne et al. [32] developed a modular platform for odor monitoring that integrates microhotplate-based MOS sensors operated under temperature modulation with embedded electronics, flow control, and on-board signal processing. Their system demonstrates that non-equilibrium approaches such as differential surface reduction can be robustly implemented outside the laboratory and applied to practical problems such as continuous raw milk quality assessment, where characteristic VOCs associated with spoilage must be detected at low concentrations in a humid, complex matrix. By exploiting temperature-dependent kinetic fingerprints, the platform achieved discrimination of milk freshness stages and environmental contaminants without relying on chromatographic separation. This work highlights the maturity of TCO-driven sensing for field-deployable applications and illustrates how microhotplate MOS sensors operated under advanced temperature schemes can support reliable, real-time monitoring in food quality control, environmental surveillance, and other applied settings.

Despite these promising results, such advanced operating modes also present notable practical limitations. First, TCO-based machine-learning models require extensive calibration data acquired under highly controlled conditions, including precise gas mixing, accurate humidity control, and reproducible VOC delivery. This often necessitates gas mixing apparatuses or permeation-based generators capable

of producing target analytes at controlled concentrations, along with reference-grade zero air. Second, reliable training data typically require a well-defined and low-volume sensor chamber with minimal dead volume, since residence time, flow distribution, and adsorption–desorption dynamics strongly influence the transient response used as ML input features. Even minor variations in flow rate, tubing materials, chamber geometry, or oxygen availability can introduce significant variability that decreases model transferability. Additionally, temperature modulation increases system complexity, imposes higher power consumption, and requires precise heater control to ensure cycle-to-cycle reproducibility. Finally, the reliance on data-driven calibration means that models may be sensitive to sensor aging, drift, or sensor-to-sensor variability, often requiring periodic retraining or transfer-learning strategies to maintain long-term stability [25]. These constraints highlight that, while TCO-enabled sensing platforms can achieve high performance in controlled environments, significant engineering effort is required to translate them into robust field-deployable instruments.

2.2 Plant Volatile Organic Compounds (VOCs)

Plant VOCs are low–molecular weight and lipophilic molecules with sufficiently high vapor pressures to diffuse into the surrounding environment. Rather than functioning as metabolic waste, they serve as information-rich chemical signals that mediate interactions with mutualists and antagonists and convey a plant's internal physiological status [7]. Their profiles consist of complex blends derived from multiple biosynthetic pathways, and their emission is tightly regulated by developmental, environmental, and stress-related cues.

2.2.1 Chemical Diversity and Biosynthetic Origins

The chemical diversity of plant VOCs reflects the metabolic pathways from which they arise. Terpenoids represent the largest class and dominate global biogenic emissions. Isoprene alone accounts for nearly seventy percent of global fluxes, while monoterpenes and sesquiterpenes contribute approximately eleven and two point five percent respectively [33]. Common representatives include α-pinene, β-pinene, myrcene, linalool, and β-ocimene, as well as sesquiterpenes such as caryophyllene, cis-α-bergamotene, and (E)$-$ β-farnesene. Plants also produce the homoterpenes DMNT and TMTT, compounds widely known for their ecological roles in attracting parasitoids [5].

A second major group consists of fatty acid–derived *green leaf volatiles* (GLVs), which include C6 aldehydes, alcohols, and esters such as (Z) 3 hexenol, (E) 2 hexenal, n-hexanal, and (Z) 3 hexenyl acetate. These compounds are responsible for the characteristic "cut grass" odor and are released within seconds of tissue disruption

[34]. Additional important VOCs include phenolics and benzenoids such as methyl salicylate (MeSA) and indole, both of which play key roles in defense and long-distance signaling.

The biosynthesis of many stress-related volatiles follows the oxylipin pathway. After mechanical injury or herbivore feeding, lipases release linoleic and α-linolenic acids from chloroplast membranes. These are converted by lipoxygenase (LOX) into 13-hydroperoxides, which are subsequently cleaved by 13-hydroperoxide lyase (13-HPL) to generate the C6 aldehydes n-hexanal and (Z) 3 hexenal [35]. This rapid biochemical sequence explains why GLVs are among the earliest detectable indicators of damage.

Importantly, the oxylipin pathway forms a metabolic branching point. The same 13-hydroperoxides required for GLV formation can alternatively feed into the allene oxide synthase (AOS) branch that produces jasmonic acid (JA). Experiments in *Nicotiana attenuata* have demonstrated a reciprocal trade-off between these branches: silencing AOS reduces JA accumulation but enhances GLV emission, whereas impairing HPL has the opposite effect [35]. This reflects a fine-scale regulation of metabolic flux depending on the type and immediacy of the stress.

2.2.2 Ecological and Functional Roles

The emission of VOCs serves both direct and indirect defensive roles. Many herbivore-induced plant volatiles (HIPVs) recruit predatory insects and parasitoids. In a classical field experiment, Kessler and Baldwin showed that artificially augmenting the VOC plume of wild tobacco increased predation of herbivore eggs and reduced overall herbivory by more than ninety percent [36]. Compounds such as β-ocimene attract parasitoids including *Aphytis melinus* and *Aphidius gifuensis*, as well as generalist predators, while methyl salicylate attracts spiders and predatory bugs and mites and hoverflies [5].

Several VOCs also act directly on pathogens or herbivores. GLVs inhibit fungal species including *Botrytis cinerea* and *Aspergillus flavus* [37], and terpenoids such as linalool reduce oviposition in lepidopteran moths [36]. Abiotic stressors likewise modulate volatile emissions: exposure to heat, ozone, or high light intensity increases VOC release, and some compounds contribute to membrane stabilization or antioxidant buffering. For example, certain GLVs mitigate cold-induced damage in maize seedlings [7].

Volatile signals also mediate plant–plant communication. Neighboring individuals can perceive and respond to volatiles emitted by damaged plants. In maize, airborne indole emitted by damaged plants is taken up by nearby individuals and converted into benzoxazinoid defense metabolites, providing enhanced protection against subsequent attack [38].

2.2.3 Determinants of VOC Emission Profiles

The qualitative and quantitative composition of a plant's VOC blend depends strongly on both the elicitor and ambient conditions. Biotic triggers include herbivore feeding such as by *Spodoptera littoralis* [39] and pathogen infection [40], while mechanical wounding alone is sufficient to generate a rapid GLV burst [11]. Abiotic elicitors such as heat and ozone further modulate the response [35].

Once induced, VOC emission rates depend on environmental parameters. Light availability is a dominant factor: emissions occur almost exclusively during the photophase and increase proportionally with light intensity. Temperature strongly modulates emission kinetics, with an optimal range around twenty-two to twenty-seven degrees Celsius, while humidity influences both stomatal conductance and volatilization. In controlled experiments on maize, maximum emission occurred around sixty percent relative humidity, and drought stress increased total volatile output. Nutrient availability also influences emission, as fertilized plants release higher amounts of volatiles independently of biomass [39].

2.2.4 Relevance for Biosensing

Because VOCs often constitute the earliest quantifiable indicators of plant stress and routinely precede visible symptoms [34], they represent an attractive target for noninvasive sensing. In engineering applications, detecting characteristic changes in volatile fingerprints enables early diagnosis of pest outbreaks or physiological stress. Low-cost metal oxide semiconductor (MOS) sensors can detect complex volatile mixtures and therefore serve as compact and real-time detectors of VOC emissions. Recent developments such as smartphone-based VOC sensors for the detection of tomato late blight highlight the potential for deploying volatile sensing technologies directly in agricultural environments [7].

This biological and ecological context motivates the central objective of this work: assessing whether commercial MOS sensors can detect plant VOC responses associated with biological activity under controlled experimental conditions.

2.2.5 Physicochemical Properties Relevant for VOC Sensing

The detectability of plant VOCs by MOS sensors is governed by their physicochemical properties, in particular vapor pressure, volatility, polarity, the presence of oxygenated functional groups, and overall reducing power [1, 41, 34]. Volatility determines how efficiently a compound partitions into the gas phase. According to leaf-level emission models, the flux of a given VOC is directly linked to its vapor pressure and diffusivity within the leaf, which is why highly volatile compounds

dominate the gas phase under typical environmental conditions [41, 42]. GLVs and many monoterpenes possess relatively high vapor pressures and therefore rapidly accumulate in the headspace where they can interact with the sensor surface [34, 37, 35]. Their partitioning behavior can be expressed in terms of Henry's constants, with nonoxygenated terpenes and isoprene exhibiting high values associated with strong tendencies to reside in the gas phase [41].

From the perspective of MOS sensors, oxygenated functional groups and their associated redox properties are equally important. GLVs are fatty acid derivatives composed mainly of C6 aldehydes and alcohols that act as reducing gases on typical n-type metal oxides [34, 37]. When these molecules are oxidized on the sensor surface, they donate electrons to the conduction band, decreasing the width of the depletion layer and thus reducing the sensor resistance [20, 1]. Similar redox-driven detection principles underlie many electrochemical and chemiresistive sensor platforms, which monitor changes in electrical signals caused by surface reactions of electroactive plant metabolites [43, 1].

Polarity further modulates adsorption and transport. More polar oxygenated compounds such as aldehydes and alcohols interact strongly with surfaces and water films, increasing their affinity for sensor and tubing surfaces but also leading to losses in sampling systems if lines are not heated or passivated [34, 44]. In contrast, less polar sesquiterpenes and larger terpenoids are more hydrophobic and therefore often transmitted less efficiently through sampling systems and may show slower equilibration with the gas phase [41, 34]. Overall, the combination of vapor pressure, polarity, and functional group chemistry produces compound-specific patterns of adsorption and redox reactivity on MOS sensors. These patterns give rise to characteristic response fingerprints for different VOC blends, providing the basis for using sensor arrays to detect stress-induced changes in plant emissions [1, 9, 10].

2.2.6 Temporal Dynamics and Biological Variability of VOC Emissions

The temporal dynamics of VOC emissions provide essential diagnostic information for biosensing applications because different chemical classes exhibit characteristic release patterns linked to the biochemical processes responsible for their formation [7]. GLVs constitute the fastest-emitted volatiles. Their production relies on rapid cleavage of hydroperoxides rather than on de novo synthesis, leading to release within seconds of herbivore attack or mechanical damage [35, 34, 37, 45]. In controlled wounding experiments, GLV emissions peak almost instantaneously and decay within minutes, forming a short transient pulse released both from damaged sites and from intact tissues [46, 40, 11]. This immediate burst is dominated by a narrow set of C6 aldehydes and alcohols and represents the sole volatile signature

during the earliest stage of damage [45].

By contrast, terpenoids and benzenoids require de novo synthesis and therefore accumulate more slowly [47, 40]. Their emission typically begins tens of minutes to several hours after elicitation, and induced sesquiterpenes often do not reach maximum levels until three to four hours following simulated herbivory [48, 45]. This delay forms a second temporal phase that follows the initial GLV burst, producing the well-established two-stage emission pattern characteristic of herbivory and detectable in time-series data from MOS-based systems [45, 7].

Superimposed on these kinetic differences is substantial biological variability in the intensity and composition of VOC emissions. Emission rates depend on genotype and phenotypic plasticity, leading to notable variation in herbivore-induced blends among plant varieties [9, 49]. Developmental stage is another important factor; for instance, younger maize plants can emit more than twice the amount of volatiles compared to older ones [50, 47]. Both damaged and undamaged tissues contribute to induced emissions, as systemic release is frequently observed across the plant canopy [51, 45]. Spatial heterogeneity also arises between above-ground and below-ground tissues; root herbivores can stimulate the release of volatiles such as (E) β-caryophyllene, which recruits natural enemies in the soil [6, 45]. Feeding location and insect species strongly influence the induced blend, producing distinct odor signatures for different herbivores and damage types [39, 52, 48]. Circadian regulation further modulates emissions, with terpenoids and benzenoids being released predominantly during the photophase and ceasing when the lights are off [39, 45].

This combination of kinetic and biological sources of variation leads to substantial heterogeneity in headspace VOC concentrations. Because plant responses integrate stress type, severity, insect density, injury duration, and developmental stage, they produce context-dependent volatile profiles that are challenging to standardize under field conditions [10]. For MOS-based systems, this variability underscores the need for multivariate sensing approaches that treat the VOC mixture as a dynamic chemical fingerprint rather than as a set of individual markers. Sensor arrays are capable of capturing these multidimensional patterns, enabling robust discrimination of stress-induced volatiles despite the inherent biological variability [1].

Chapter 3

Material and Methods

This chapter describes all experimental procedures, instrumentation, and data processing steps used throughout the thesis.

For clarity and to avoid redundancy, the setups for all experiments (sheep wool, greenhouse monitoring, and maize herbivory) are presented here, while their biological motivation and scientific context are provided in the corresponding Results sections (chapter 4).

3.1 Hardware

To address the challenge of VOC detection, the device implemented in this thesis uses commercially available off-the-shelf components, including development boards and SBC (Single Board Computer). This allowed for rapid production and use of the device.

3.1.1 Sensors

One sensing unit is composed of two individual sensors, one for gas and one for temperature and humidity. Both are integrated on individual breakout boards (Adafruit Industries, New York, NY, USA), which are then electrically connected using a perfboard support. Both sensors communicate with the I^2C (Inter Integrated Circuit) protocol, which requires only two wires, meaning a total of four, including power and ground, are needed for the complete connection. This is done using a four-conductor wire (Sensocord®-PUR $4 \times 0.34\ mm^2$)[1], a Wire to Board Terminal Block, and connectors to plug into a breadboard.

[1]Kabeltronik Arthur Volland GmbH, Denkendorf, Germany

(a) Adafruit SGP40 Air Quality Sensor Breakout

(b) Adafruit SHT31-D Temperature & Humidity Sensor Breakout

Figure 3.1: Breakout boards of the VOC and environmental sensors used for data collection adapted from Kattni Rembor, licensed under CC BY-SA 4.0

Gas sensor

The SGP40 (Sensirion AG, Stäfa, Switzerland) MOS gas sensor (see Figure 3.1a) was chosen as it provides a complete package of sensing elements, readout electronics and humidity compensation. The sensor has a low-power consumption (2.6 mA at 3.3 V), can be sourced at low-cost and has been shown to reach 50 ppb accuracy when used in conjunction with a GC (Gas Chromatography) column [32, 24]. The output signal is a 16-bit unsigned integer in arbitrary units defined by the manufacturer as *ticks*, proportional to the logarithm of the semiconductor's resistance. It includes a membrane to protect it from siloxane poisoning and four sensing pixels with different doping to target a wide range of VOC [53, 54], it has been shown that the protective membrane also affects the sensor's dynamics and sensitivity [55, 24].

Temperature and humidity sensor

The effect of water vapor on MOS sensors is similar to that of a reducing gas [15]; to decorrelate the output response, the SGP40 makes use of temperature and humidity values as input parameters when receiving commands from the I^2C master.
The SHT31 (Sensirion AG, Stäfa, Switzerland) digital humidity and temperature sensor (see Figure 3.1b) was selected for its good accuracy in both data outputs and the low cost [56]. The version chosen is also covered by a $100\mu m$ PTFE membrane that provides IP67 protection against dust and water allowing the use in harsh environments.

3.1.2 Single Board Computer

The sensor data was collected using a Raspberry Pi 4 Model B Rev 1.4, 8GB (Raspberry Pi Ltd., Cambridge, England), a SBC running Raspberry Pi OS Lite equipped with WiFi connectivity, I^2C bus and onboard storage with a Micro-SD card. The control loop for the sensors was performed with a C script logging time referenced data in a CSV (Comma Separated Value) file, the device terminal was accessed with SSH (Secure Shell).

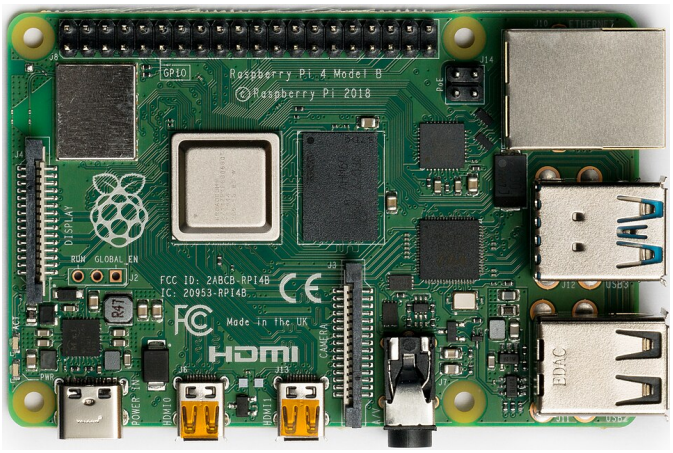

Figure 3.2: Raspberry Pi 4B by Laserlicht on Wikimedia Commons , licensed under CC BY-SA 4.0

3.1.3 Architecture

For the experimental setup, eight identical sensor modules needed to operate simultaneously on a single I^2C bus. Since the SHT31 can only use 0x44 or 0x45 and the SP40 has a fixed address of 0x59, a multiplexer was required to avoid address conflicts.

A simple I^2C multiplexer breakout board, the TCA9548A (Adafruit Industries, New York, NY, USA), was chosen for its availability, low cost, and because it provides eight controllable ports that forward all I^2C signals. Each port can be individually enabled or disabled by sending the corresponding command to the multiplexer's address, which defaults to 0x70. This address can be modified by shorting any of three pads on the PCB (Printed Circuit Board), allowing eight possible addresses and enabling up to 64 identical devices to be connected to the same I^2C bus.

This was mounted on a breadboard, which was then inserted in a 3D-printed

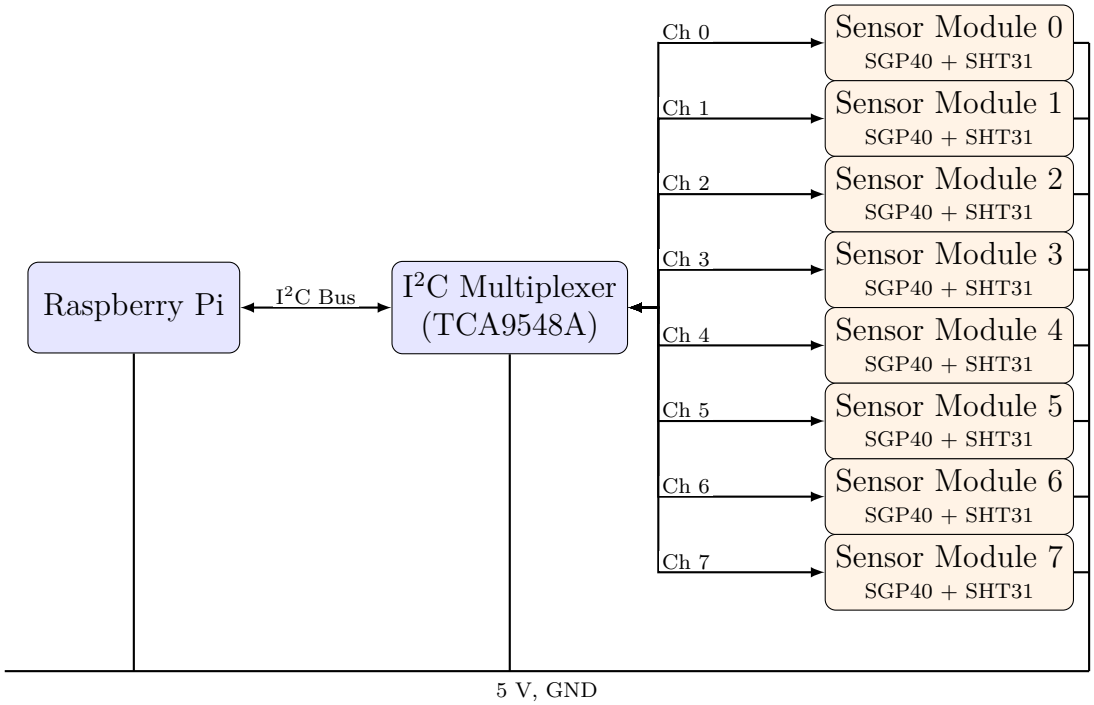

Figure 3.3: High-level schematic of the sensing setup. The Raspberry Pi communicates via an I²C multiplexer (TCA9548A) with eight sensor modules (channels 0–7), each containing an SGP40 and SHT31 sharing the same I²C bus and 5 V/GND lines.

support that also housed the RPi[2]. The assembly was then glued to a wooden board, and connections between the sensor modules and the breadboard were established using jumper wires. These wires were routed from the breadboard to lever-type terminal blocks, which were mounted on 3D-printed holders[3]. From the terminal blocks, proper cables described in subsection 3.1.1 were used to connect to the sensor modules, ensuring reliable electrical contact while allowing easy disconnection and reconfiguration of the setup, the simplified wiring diagram is included in Figure 3.3, while a picture of the setup is provided in Figure 3.4.

[2]By user nilok (Printables.com), licensed under CC BY-NC-SA 4.0 [57].

[3]Parametric lever wire connector mount by user TheOneTruePatrick (Printables.com), licensed under CC BY 4.0 [58].

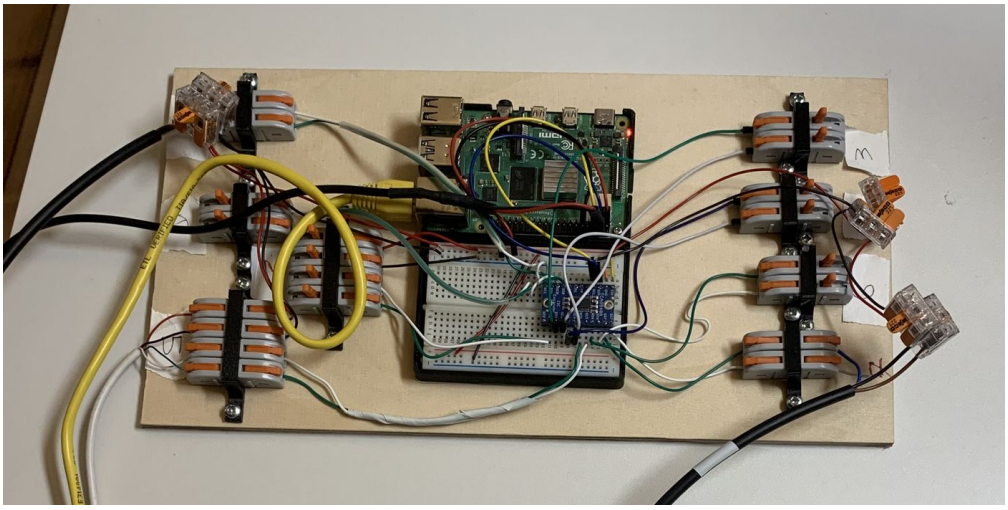

Figure 3.4: The experimental sensing platform developed for rapid connection of sensor modules with three of them connected.

3.2 Software

The software developed for this thesis consists of two main components, corresponding to the hardware on which it was executed and the specific role it fulfilled:

- **Data acquisition on the RPi.** The main logging program was written in C and relied on manufacturer-provided Sensirion libraries for low-level communication with the sensors, together with custom routines developed specifically for this project. The program handled sensor initialization, I^2C communication, timing, error checking, oversampling, and periodic storage of measurements in CSV format.
- **Data processing on a workstation.** All analysis was conducted in MATLAB R2025a (The MathWorks Inc., Natick, Massachusetts, USA). A collection of MATLAB scripts was implemented to import, visualize, and process the time-series data, including exploratory plotting, environmental correlation analysis, and GC-MS alignment for the herbivory experiment.

3.2.1 Data Acquisition

The embedded C program running on the RPi continuously read values from the SGP40 and SHT31 sensors through the I^2C multiplexer. Each acquisition cycle produced temperature, relative humidity, and VOC-related measurements, which were timestamped using the RPi's system clock and written to a local CSV file.

Timestamps followed the ISO 8601 format (e.g. 1999-03-22T05:06:07). For correct timekeeping, the RPi required an active network connection at least once after boot to synchronize with an NTP server, which occasionally posed challenges on restricted IoT-only networks.

Full source code is included in Appendix B; the description below summarizes the main logic.

Sensirion libraries

Communication with the SGP40 and SHT31 sensors was handled using the official Sensirion Raspberry Pi I²C driver libraries[4]. These libraries provide a hardware-agnostic abstraction layer for I²C communication, CRC validation, timing, and device-specific measurement commands. The following headers were included:

```
#include "libraries/sensirion_common.h"
#include "libraries/sensirion_i2c.h"
#include "libraries/sensirion_i2c_hal.h"
#include "libraries/sgp40_i2c.h"
#include "libraries/sht3x_i2c.h"
```

Their roles can be summarized as follows:

- `sensirion_common.h` — shared utilities (CRC checks, byte-order helpers, error codes).
- `sensirion_i2c.h` — generic I²C protocol functions used by all Sensirion devices.
- `sensirion_i2c_hal.h` — hardware abstraction layer that maps generic I²C calls to the Raspberry Pi's I²C device driver.
- `sgp40_i2c.h` — device-specific driver implementing the official SGP40 measurement sequences, including humidity-compensation input handling.
- `sht3x_i2c.h` — driver for the SHT31, providing temperature and humidity measurement commands and repeated-start I²C transaction handling.

Using these manufacturer libraries ensured compliance with the recommended sensor command sequences and timing constraints, reduced the likelihood of communication errors, and provided reliable humidity and VOC measurements for all experiments.

[4]Available at `https://github.com/Sensirion/raspberry-pi-i2c-sgp40` and `https://github.com/Sensirion/raspberry-pi-i2c-sht3x`.

Oversampling and logging

To reduce the influence of short-term noise, the program performed oversampling by averaging multiple consecutive readings from each sensor port. Two configuration parameters controlled this behavior:

- oversample_count (default: 5), the number of raw readings averaged into a single logged data-point,
- sht31_humidity_offset (default: 0), an optional correction applied to the SHT31 humidity reading.

Both parameters were defined in a dedicated configuration file, allowing for run-time adjustments of sampling behavior without needing recompiling nor modifying the core acquisition logic.

The choice of a one-second raw sampling interval was based on the manufacturer's recommended measurement rate for the SGP40, ensuring that the operating conditions matched those specified in the datasheet. The oversampling routine simply averaged multiple consecutive one-second readings and therefore did not modify the intrinsic sensor sampling behavior. Instead, the effective logging rate was determined by the configurable oversample_count parameter.

This structure allowed the system to balance temporal resolution and noise reduction: a low oversample_count provided finer resolution for rapid tests, whereas a higher value reduced noise and kept file sizes manageable during multi-hour experiments.

The sht31_humidity_offset parameter was introduced during early development, when the platform was tested using a different humidity sensor model. The two humidity sensors exhibited a small but systematic offset, and this parameter enabled evaluating whether artificially correcting the SHT31 reading affected the downstream humidity-compensation algorithm of the SGP40. Although unnecessary in the final configuration (where only identical SHT31 sensors were used), the parameter was retained for completeness.

Main sampling loop

At each iteration, the program collected and accumulated data from all sensor channels, applied oversampling, timestamped the result, and wrote a single row to disk. Each CSV file contained timestamped measurements of temperature, relative humidity, and raw VOC ticks for all eight sensor ports. To ensure traceability across batches, filenames incorporated both the timestamp and an experiment label supplied as a command-line argument (via argc/argv).

```
while (1) {
    for (int i = 0; i < oversample_count; i++) {
        sample_all_ports(accum, sht31_humidity_offset);
        sensirion_i2c_hal_sleep_usec(1000000); // 1 second delay
    }

    get_timestamp(timestamp, sizeof(timestamp));
    finalize_averages(logfile, accum, oversample_count, timestamp);
    reset_accumulators(accum);
}
```

At the beginning of each new log file, the program automatically generated a CSV header row containing the timestamp and, for each port, the corresponding temperature (T#), humidity (H#), and VOC (VOC#) columns. This ensured a consistent column structure across all files and allowed ports marked as *NaN* (e.g., disconnected sensors) to be handled seamlessly during MATLAB import and batch processing.

The application was designed with modularity in mind. During early development, support was implemented for configuring different I^2C addresses for the multiplexer, allowing in principle up to 64 sensor modules to be attached to the same bus. Although this full capability was not required for the present work, the structure was retained for future scalability. A similar modular principle motivated the implementation of a hot-swapping feature: at each iteration, the program scanned the I^2C bus to detect the presence or absence of sensor modules. This allowed sensors to be unplugged and reinserted while the script was running, without requiring a restart of the data acquisition process. In particular, for ports that did not respond to mux_i2c_detect(), all measurable parameters were assigned the value *NaN* (Not a Number). This convention is natively interpreted by MATLAB as missing data and allowed all logged CSV files to maintain fixed-width rows with consistent column structure, simplifying subsequent parsing and analysis.

3.2.2 Data Processing

The complete processing scripts are reported in Appendix C. The processing pipeline described below was applied identically to all experiments unless otherwise specified, with only minor additions introduced when required by the structure of a specific dataset.

Importing and structuring the data

Each CSV file was imported using the `readtable` function, and timestamp strings were converted into native `datetime` objects to ensure proper temporal alignment.

Because the number of active sensing ports varied between experiments, the script automatically inferred the number of channels by dividing the number of non-timestamp columns by three, corresponding to temperature, humidity, and VOC readings for each port. The signals were then reorganized into dedicated matrices, while non-existent or unused channels were represented as `NaN`. This approach ensured that all datasets were handled uniformly without the need for experiment-specific code branching.

In the wool measurements, some recordings were split across consecutive files due to acquisition restarts. In these cases the tables were concatenated and sorted by timestamp before further processing, effectively reconstructing a continuous time series and preventing discontinuities in downstream analyses.

Transformation of the VOC signal

The SGP40 raw VOC output ($\mathrm{VOC}_{\mathrm{ticks}}$) corresponds to an internal, logarithmic representation of the sensor resistance R. Since electrical conductance G is inversely proportional to resistance,

$$G = \frac{1}{R},$$

a higher VOC concentration (leading to a reduction in R) results in a decrease in the raw tick value. To obtain a quantity that increases with gas concentration and is proportional to the logarithm of the conductance, the VOC signal was inverted:

$$G_{\log}(t) = -\,\mathrm{VOC}_{\mathrm{ticks}}(t) \propto log(G(t)).$$

This simple transformation preserves the logarithmic response while producing a visually intuitive signal in which rising VOC levels correspond to upward shifts in the processed trace.

Noise reduction and smoothing

The raw time-series signals exhibited high-frequency noise originating from analogue-to-digital conversion and minor environmental fluctuations. To suppress this noise while preserving the slower dynamics relevant for VOC emission processes, a 20-sample moving average (MATLAB `movmean`) was applied to the VOC, temperature, and humidity channels:

$$x_{\mathrm{smooth}}(t) = \frac{1}{20} \sum_{k=-9}^{10} x(t+k).$$

The window length was selected empirically as a compromise between noise reduction and preservation of characteristic rising edges associated with sample introduction or concentration changes.

Port identification and labeling

Each sensing port corresponded to a fixed physical sampling position within the measurement setup (e.g. individual wool samples, clean-air references, or plant chambers). A port-to-label mapping was defined at the beginning of each analysis using a MATLAB `containers.Map` object, ensuring consistent traceability across datasets. For the induced-VOC plant experiments, ports were additionally classified as either control or treatment channels to enable color grouping in the visualization phase.

Time-window selection (plant experiments only)

In the induced-VOC experiments on maize, only part of the full recording period was relevant for inter-batch comparison. For consistency, the displayed time window was trimmed to fixed daytime intervals defined by the recording day. Batch 1 was plotted from the beginning of the measurement until 18:00 on the next day, while Batch 2 was trimmed to the same interval extended to 18:30. This ensured that both batches were visualized over matching daily periods.

Visualization and export

For each dataset, three time-series plots were generated showing the processed VOC signal, relative humidity, and temperature. In the wool experiments, color assignment was based on the perceptually uniform `linspecer` palette, while in the plant experiments a set of blue and green shades was used to distinguish control from treatment channels. Markers were added at regular intervals along each trace to aid visual inspection, and an interactive legend allowed individual curves to be toggled on or off.

All figures were exported using a dedicated helper function that standardized the aspect ratio, font sizes, and line widths prior to producing vector PDF output. Titles were removed in the exported version to facilitate integration into the manuscript layout, and file names were generated automatically from the experiment descriptors. This procedure ensured consistent visual appearance and formatting across all figures included in this work.

3.2.3 Processing of GC-MS Data

Volatile organic compounds were collected using dynamic headspace sampling on Tenax-based sorbent tubes, as described in the corresponding methodological sections for the wool and herbivory experiments. Briefly, approximately 1 g of sheep wool or an intact potted maize plant was placed on aluminum foil under a glass dome. Synthetic air was pumped into the top of the dome at a rate of

300 mL min^{-1}, while a simultaneous vacuum of 200 mL min^{-1} was applied to a thermal-desorption tube (Tenax TA) positioned in one of the side outlets. This setup ensured a continuous flow of purified air across the sample and efficient trapping of emitted VOCs. Each volatile collection lasted 2 h and was replicated across multiple batches, following the same airflow conditions as those used for the sensor recordings.

All laboratory procedures required for thermal desorption and chromatographic separation were performed by experienced staff at the hosting laboratory (UZH, Zürich, Switzerland), including Dr. Dani Lucas Barbosa. Sorbent tubes were desorbed for 10 min at 250°C and cryo-focused at −20°C. Secondary desorption was performed at a ramp rate of 40°C s^{-1} to a final temperature of 280°C, held for 10 min. The released compounds were transferred (split ratio 1:4) onto a non-polar gas-chromatography column operated with helium as carrier gas at 1 mL min^{-1}.

The GC oven was programmed from 40°C (5 min hold) to 250°C (8 min hold) at 5°C min^{-1}. The MS interface and ion source were maintained at 250°C, and electron ionization was set to 70 eV. Mass spectra were acquired in the m/z 35–400 range at 4.7 scans s^{-1}. A standard *n*-alkane mixture (C_8–C_{20}, 10 µg mL^{-1}) was run under identical conditions to compute AI (Arithmetic retention Indices) for compound annotation.

For each sample, the GC-MS output consisted of a peak table containing retention times, tentative compound identities, and peak intensities. The raw data were pre-processed using the MetAlign–MSClust pipeline [59, 60], which performs baseline correction, noise removal, chromatogram alignment, and clustering of co-eluting ions into reconstructed mass spectra of putative compounds. Only aligned peaks detected between 5 and 25 min and within the 55–400 m/z range were retained for downstream analysis. Tentative annotation was performed by comparing both mass spectra and experimentally determined AI values with entries from the Wageningen Mass Spectral Database of Natural Products and the NIST library. For each compound, a representative diagnostic ion was selected as the quantitative feature. Peaks with intensities not exceeding the background were excluded.

Peak-intensities tables were exported in CSV format and prepared for multivariate analysis by the author. Data were formatted according to the requirements of the MetaboAnalyst online platform (`https://www.metaboanalyst.ca/`), with samples as rows, VOC features as variables, and metadata specifying treatment and batch. Statistical processing included $\log_{10}$ transformation and autoscaling (mean-centering and division by the standard deviation) to stabilize variance across compounds of different abundances. Heatmaps were used to visualize global emission patterns and inspect differences between *Spodoptera*-damaged and control plants.

It is important to note that GC-MS peak intensities cannot be compared quantitatively between different compounds because ionization efficiency and detector response vary across analytes. Meaningful comparisons are therefore restricted to *within-compound* differences across samples. Since the GC-MS dataset served as a qualitative chemical reference rather than a quantitative calibration source, no attempt was made to align GC-MS intensities with the VOC sensor time series. Instead, the chromatographic profiles were used to contextualize sensor signals and support qualitative interpretation of emission strength across samples.

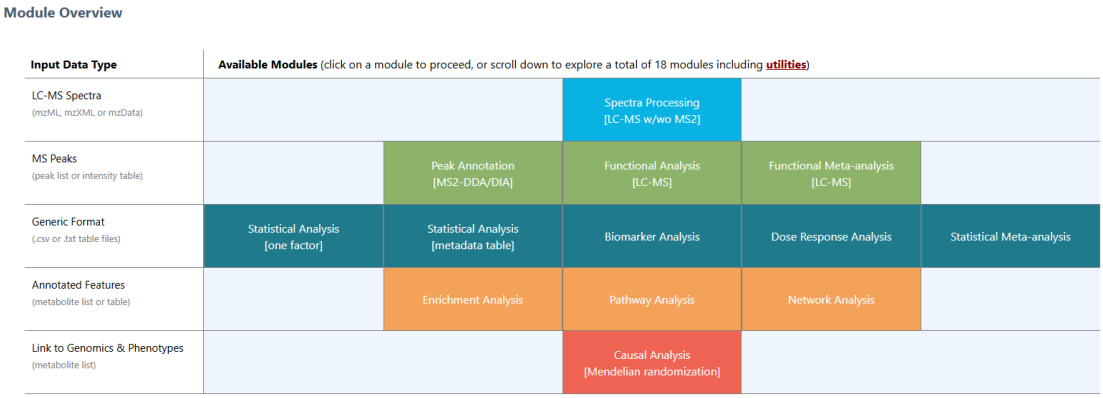

Figure 3.5: Screenshot of the `https://www.metaboanalyst.ca/` interface illustrating the available analysis modules. In this work, the *Statistical Analysis (metadata table)* module was used for processing the GC-MS peak-area data.

3.3 Experimental Setups

This section describes all experimental configurations used throughout this work, including sensor characterization tests, sheep wool VOC sampling, greenhouse monitoring, and the maize herbivory experiment. All experiments employed the sensing platform detailed in Chapter 3, and data were collected and processed following the workflow outlined in Section 3.2.1.

3.3.1 Sensor Characterization Tests

Two preliminary tests were performed to validate sensor operation and to assess cross-sensitivity to humidity. These characterizations ensured correct functionality before conducting the biological experiments.

Ethanol-based transient response test

As recommended in the *SGP Design-In Guide* by Sensirion [61], the first functional test consisted of exposing the sensor array to a brief pulse of ethanol-based vapors released from a permanent marker. The VOC source was positioned approximately 10 cm from the sensors, measured under ambient condition without enclosure, to generate a short, localized perturbation. This test served to confirm correct initialization and communication of all sensor modules, and to evaluate their transient response characteristics (see Section 2.1.4).

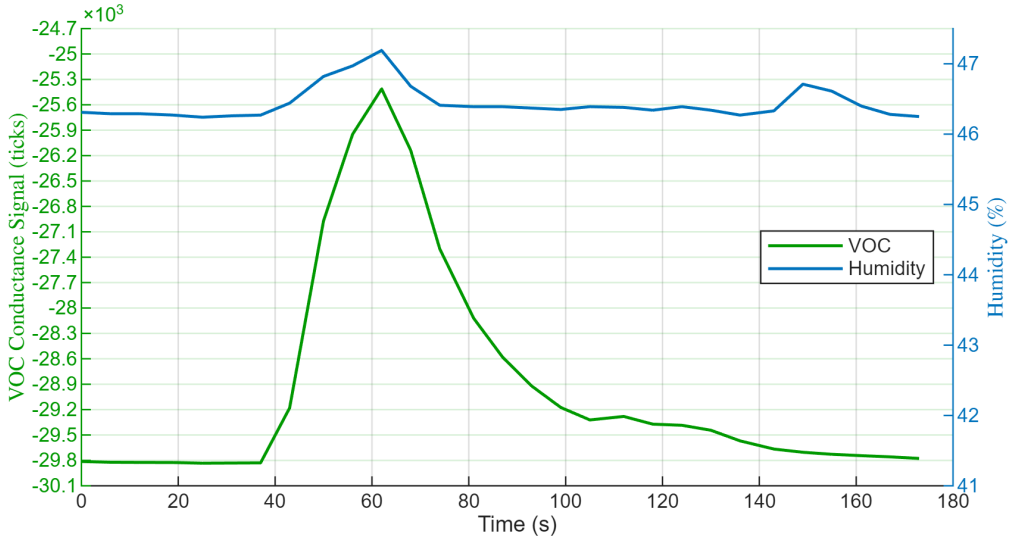

Figure 3.6: Transient response of the VOC channel to a short ethanol pulse released near the sensors.

Humidity disturbance test

A second characterization assessed the effect of abrupt humidity changes. The sensors were positioned above a beaker containing hot water (approximately 60°C) covered with aluminium foil to retain water vapor. This configuration produced a rapid rise in relative humidity, approaching saturation (100%). The objective was to evaluate the magnitude of humidity-induced variations in the compensated VOC signal and to verify the effectiveness of the manufacturer's humidity compensation algorithm [53].

3.3.2 Sheep Wool VOC Collection

This section describes the dynamic headspace sampling protocol used to collect volatiles from sheep wool, whose results are presented in section 4.2.

The setup used for the wool experiments is shown in Figure 3.7. Eight glass domes were placed on freshly replaced aluminium foil, each equipped with four lower ports and one upper port. Synthetic air (80% N_2, 20% O_2) was supplied from a pressurized cylinder through a PTFE manifold split into eight parallel channels. Each line incorporated a rotameter to adjust and maintain an inflow of 300 mL min^{-1}, introduced from the top of each dome.

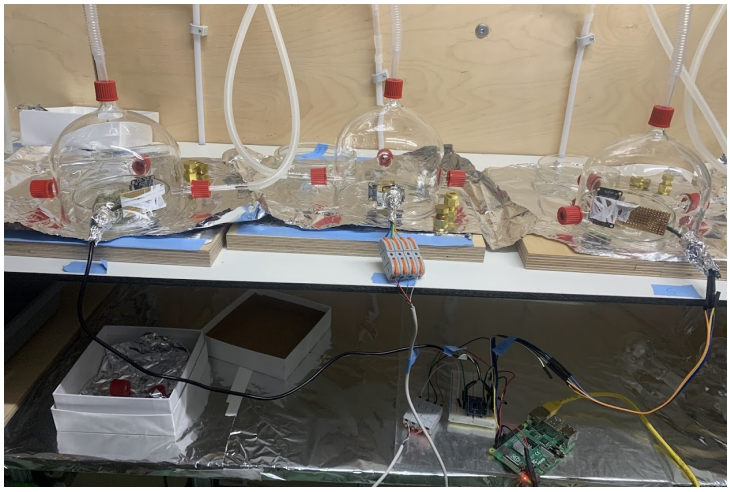

(a) Preliminary setup used to determine optimal sampling duration.

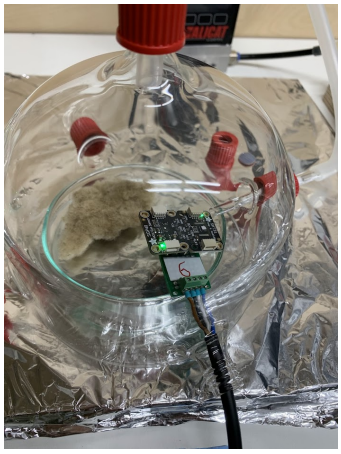

(b) Detail of a collection unit with wool sample, sensor module, and sorbent tube.

Figure 3.7: Experimental setup for sheep wool VOC sampling.

Volatiles were collected using Tenax TA sorbent tubes (8 mm OD, 6 mm ID) inserted into one of the lower dome ports. Chamber air was drawn through each tube at 200 mL min^{-1}, generating slight overpressure to prevent contamination. Flow rates were verified using a secondary flow meter before the tubes converged into one of two pumps (four chambers per pump).

Sensor modules were placed inside each dome, with cables passed through a lower port and sealed with aluminium foil. Based on preliminary tests, a sampling duration of two hours was selected.

A total of eight batches (54 samples) were collected. Each batch included one background measurement containing only an empty Petri dish. Between batches, domes were rinsed under a fume hood using both polar and non-polar solvents and placed on fresh aluminium foil before the next sampling sequence.

3.3.3 Greenhouse Monitoring Experiment

The following setup describes the configuration used in the greenhouse monitoring experiments, which are analyzed in Section 4.3.

A long-term monitoring campaign was conducted inside the greenhouse in which the maize plants for the herbivory study were grown (Agroscope, Reckenholz, Zurich). Two sensor modules were enclosed in transparent plexiglass tubes: one containing a healthy maize plant at the V3 stage, and the other containing only moist soil in an identical pot. The tubes were nearly sealed except for three circular 1 cm holes, creating a semi-closed environment that allowed accumulation of VOCs and humidity. Two additional sensors were placed in the open greenhouse atmosphere to record background conditions.

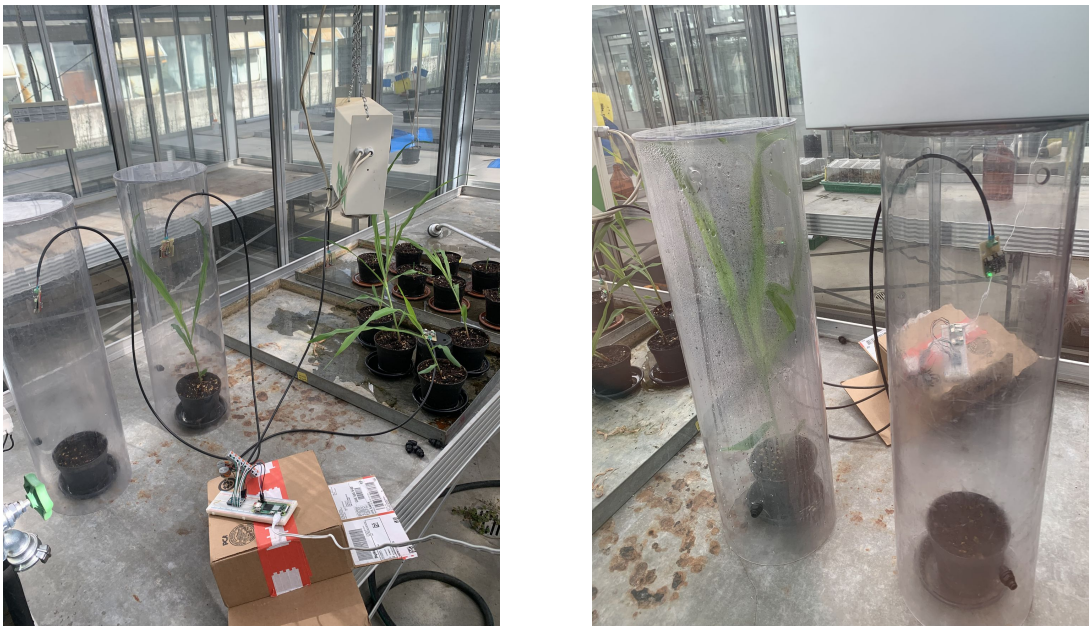

(a) Sensor placement on the first day of monitoring.

(b) Enclosures after one week, showing humidity buildup in the plant-containing tube.

Figure 3.8: Greenhouse monitoring configuration.

Greenhouse environmental conditions varied due to automatic ventilation, weather fluctuations, and supplemental lighting. All sensors logged data continuously using the same pipeline as in the laboratory experiments, enabling comparison among (i) a confined plant environment, (ii) a confined soil environment, and (iii) open-air greenhouse conditions.

3.3.4 Extended Four-Tube Greenhouse Setup

To assess the reproducibility of the observations made in the initial two-tube greenhouse experiment, an extended monitoring trial was conducted from 4 August to 20 August inside the same greenhouse facility (Agroscope, Reckenholz, Zurich). Four transparent plexiglass enclosures of identical geometry were employed. All tubes were initially filled with moist soil; in two of them, maize seeds were sown at the start of the experiment and germinated within the first days, producing two healthy V3 plants. A third tube contained only moist soil, while the fourth enclosure held an empty plastic pot without soil. All four sensor modules deployed in this trial were factory-new to eliminate the influence of previous VOC exposure or long-term drift. The enclosures were placed side by side on a single metal greenhouse bench

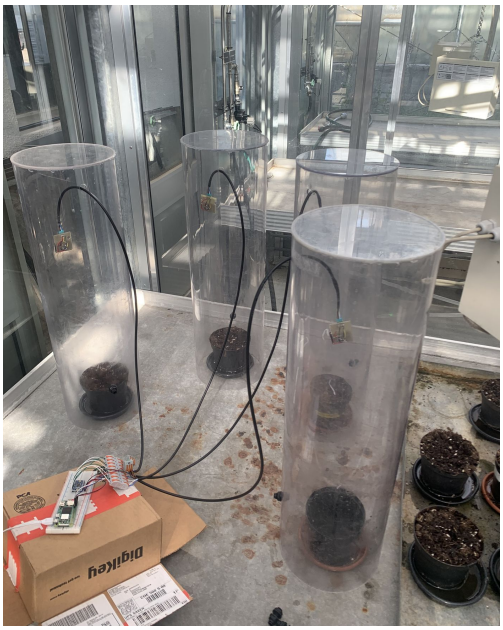

(a) Configuration at the beginning of the extended trial. All four tubes contained moist soil; maize seeds were sown in the first two enclosures (left).

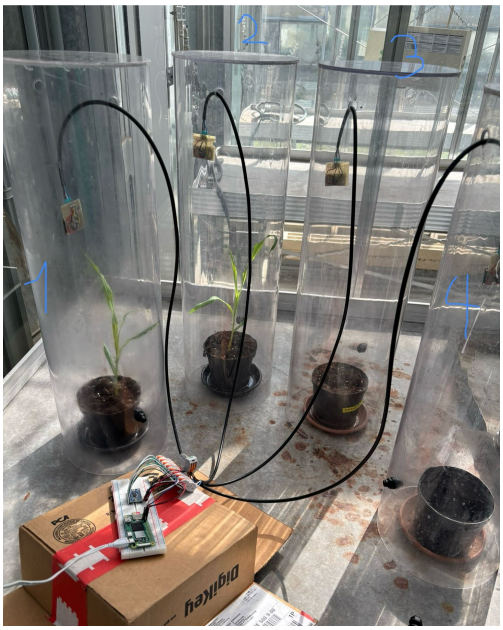

(b) System shortly after the watering event on 13 August. Increased humidity is visible in the plant tubes.

Figure 3.9: Photographic documentation of the four-tube greenhouse setup.

and experienced comparable illumination from overhead greenhouse lighting and natural sunlight. Each tube was semi-closed, with three circular ventilation holes (1 cm diameter), creating a confined headspace in which humidity and volatiles could accumulate. Temperature inside the enclosures remained highly similar due to their identical geometry and shared exposure conditions, whereas relative humidity varied depending on tube contents and watering events.

Photographs documenting the physical configuration of the system at the beginning of the experiment and after a mid-experiment watering event are shown in Figure 3.9a and Figure 3.9b. The state of the growing plants toward the end of the trial is shown in Figure 3.10. All four sensor modules logged VOC, humidity, and temperature data continuously using the same acquisition routines described in Section 3.2.1.

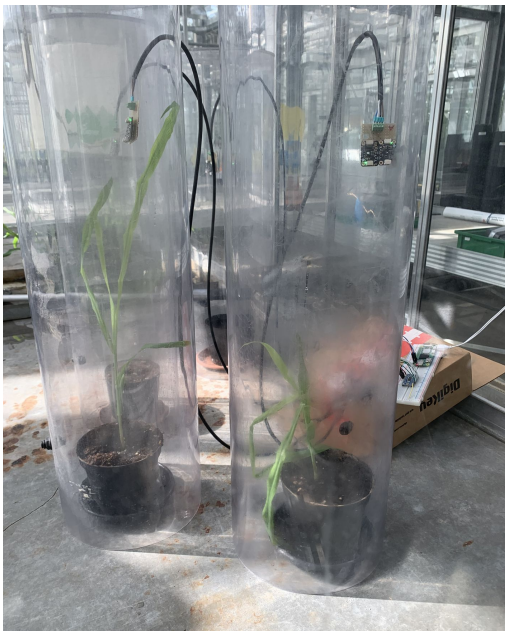

Figure 3.10: Enclosures on 18 August. Two V3 maize plants have developed in the leftmost tubes. Moisture condensation is clearly visible in the plant enclosures.

3.3.5 Maize Herbivory Experiment

This section details the controlled laboratory herbivory setup used to investigate induced maize volatiles (results in Section 4.4).

The herbivory experiment used eggs of *Spodoptera littoralis* obtained from Prof. Ted Turlings (Université de Neuchâtel). Upon arrival, eggs were placed in a mesh cage together with five maize plantlets (Figures 3.11–3.14). Excess egg batches were removed to avoid overcrowding. Larvae hatched after 3–4 days and consumed most of the leaf mesophyll, confirming successful rearing.

Eight enlarged glass domes were used, following the same principles as the wool experiment but scaled for whole maize plants. Maize (*Zea mays* L., cultivar Pioneer® P9610) was grown for 12 days in 8 cm pots and watered every four days. On the day of the experiment, plants were watered with 50 mL and covered with

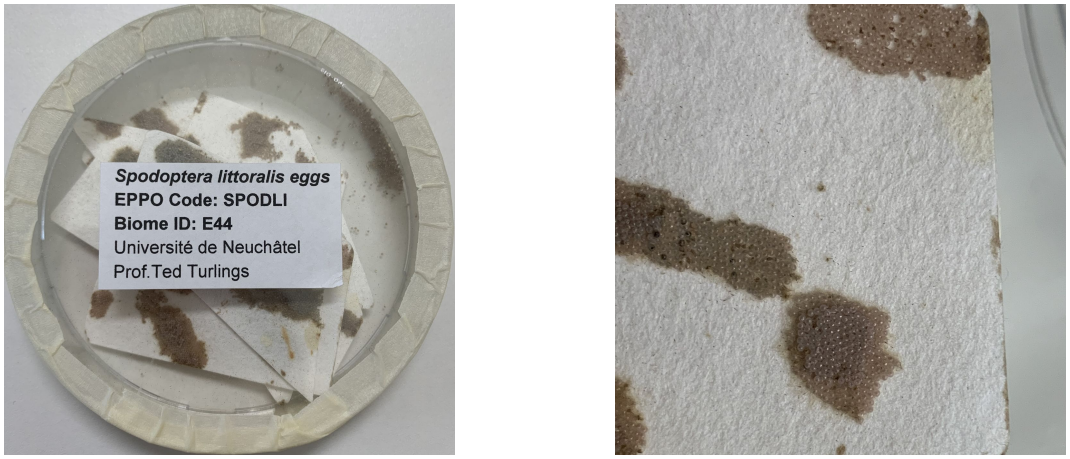

(a) Egg clusters received in Petri dishes. **(b)** Detail of an individual egg batch.

Figure 3.11: Overview and detail of *S. littoralis* eggs used in the herbivory experiment.

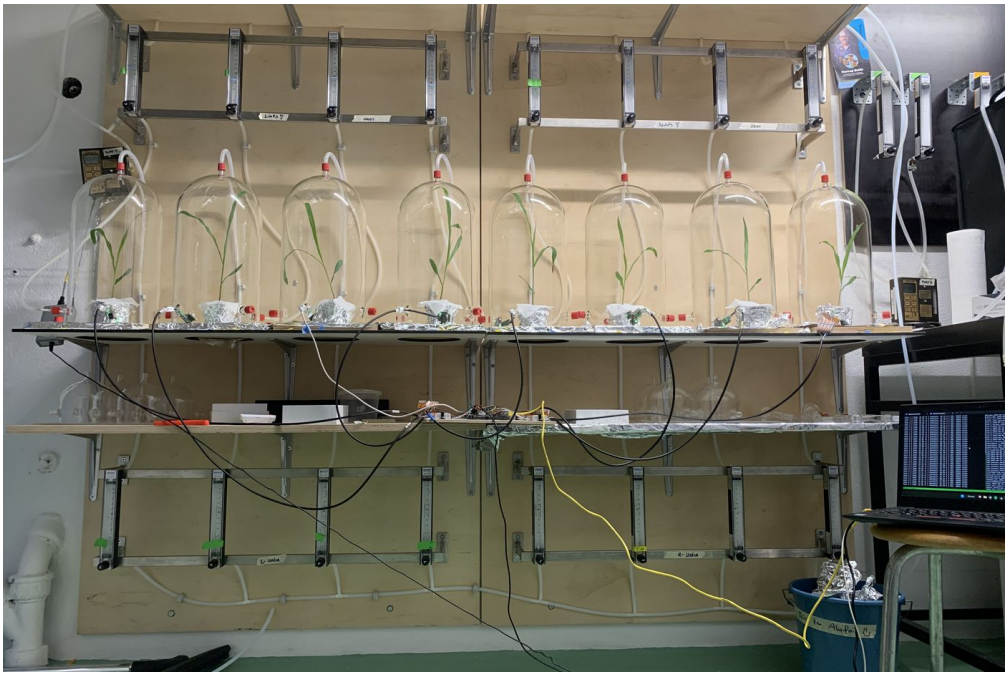

Figure 3.12: Laboratory configuration for maize herbivory VOC sampling.

aluminium foil to minimize soil VOC emissions.

Three first-instar larvae were placed on each plant and allowed to feed freely for 20–22 hours before VOC sampling. Feeding continued during the two-hour

forced-air sampling period, resulting in a total herbivory duration of approximately 24 hours.

Figure 3.13: Mesh cage containing maize plantlets and eggs.

Figure 3.14: Skeletonized leaves after larval feeding.

Synthetic air was supplied and extracted using rotameters connected to a pressurized cylinder and vacuum pump, maintaining constant chamber pressure. The same MOS sensor modules were used for continuous VOC monitoring. Four of the eight chambers served as undamaged controls. GC-MS sampling was synchronized with the final two hours of forced-air collection. Temperature and humidity were recorded using the integrated sensors.

After sampling, larvae were removed and above-ground biomass was measured for subsequent GC-MS data normalization.

Chapter 4

Results and Discussion

4.1 Sensor characteristics

To explore and understand the performance of the MOS sensors, a set of simple experiments was performed, targeting known weak points such as drift, noise, and humidity influence.

4.1.1 Results and Discussion

The output response from the ink test is shown in Figure 3.6. The sensor exhibited a rapid increase in signal, followed by a quick recovery, consistent with the manufacturer's specifications. The rise time was below 30 s, and recovery occurred within approximately one minute [61]. At its maximum, the conductance increased by over 4400 ticks relative to the clean air baseline, while the relative humidity rose by only 1%. This confirmed the expected sensitivity to volatile compounds and indicated low cross-sensitivity to humidity. Moreover, the reproducible response validated both the hardware configuration and data acquisition pipeline.

A qualitative humidity control was performed to assess whether abrupt moisture changes could explain the large VOC-like events observed later in biological experiments. During the test, relative humidity was increased by more than 40%, approaching saturation. Despite this large stimulus, the compensated VOC signal changed by only around 300 ticks (see Figure 4.1), compared with the $\sim$4400 tick response elicited by a small ethanol VOC pulse. Although the uncompensated raw output was not recorded in this test, the small amplitude of the compensated signal under such extreme humidity conditions provides qualitative evidence that humidity variation alone is unlikely to account for the major signal changes observed in subsequent experiments. Consequently, large events in the biological experiments are more plausibly attributed to genuine VOC fluctuations or other experimental perturbations, rather than to uncompensated humidity artefacts alone.

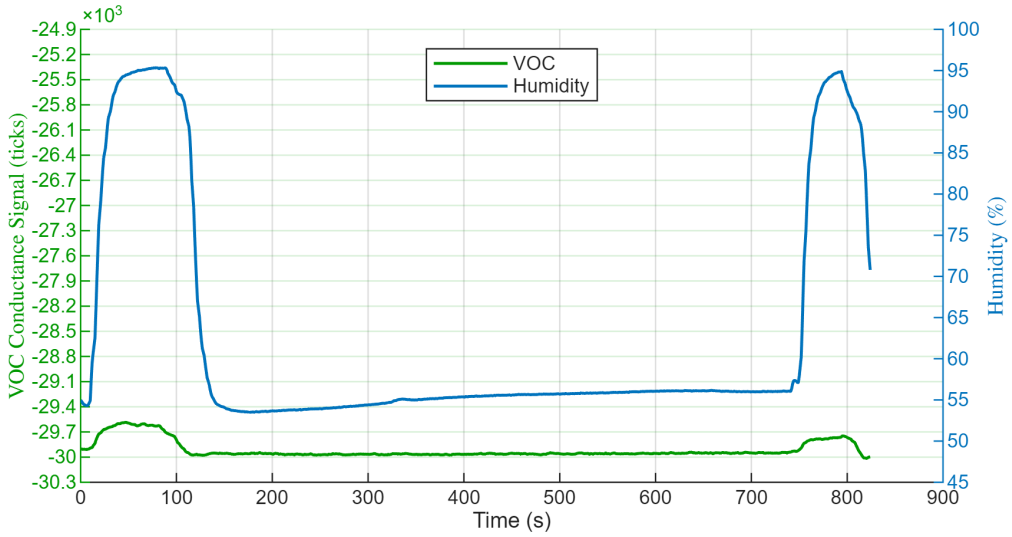

Figure 4.1: Response of the VOC channel to a rapid increase in relative humidity. The humidity was raised from approximately 60% to nearly 100% using a beaker of hot water. Only a small variation in signal intensity (∼300 ticks) was observed, confirming the low humidity cross-sensitivity of the sensor.

This interpretation is consistent with the on-chip compensation strategy described by Rüffer et al. [53], which corrects most humidity-related conductance shifts using the co-located RH measurement.

A brief transient response was visible at the onset of the humidity increase. Although the temporal shape of this signal resembles that of a typical VOC response, its amplitude was more than an order of magnitude smaller. This behavior is consistent with a short-lived physical perturbation, such as minor thermal or diffusion gradients near the sensing surface, rather than a genuine chemical interaction with the sensing layer. Long-term humidity effects on metal-oxide sensors are well documented and involve gradual changes in surface chemistry through the adsorption of physisorbed and chemisorbed water [16], typically leading to slower and more sustained drifts than those observed here. The combination of a small amplitude and rapid relaxation therefore supports the conclusion that humidity fluctuations alone cannot account for the much larger VOC-like signals observed in later biological experiments.

Overall, these preliminary characterizations confirmed that the sensor platform behaved as expected under simple test conditions. The strong and reversible response to ethanol vapors demonstrated high reactivity to volatile compounds, while the limited effect of large humidity variations indicated robust performance in varying environmental conditions. These results provided the necessary confidence to proceed with more complex biological experiments, where the sensors would be

exposed to plant-emitted VOC under controlled laboratory settings.

4.2 Sheep wool VOC Preliminary Experiment

In this section, the sensor system is validated through a preliminary experiment conducted on sheep wool samples. The study had two objectives: (i) to assess the performance of the sensor array under realistic measurement conditions, and (ii) with the dynamic headspace sampling workflow introduced in subsection 3.3.2 and used later in the main experiment of this thesis.

Before presenting the results, the following background provides the biological and ecological motivation for analyzing sheep wool volatiles.

4.2.1 Background

This work was carried out as part of a broader project following the research of Brok et al. [62], which aims to reduce damage caused by biting midges of the genus *Culicoides* (Diptera: Ceratopogonidae). These insects are vectors of pathogens in the livestock industry, which can potentially cause disease to animals such as the bluetongue virus and can also trigger allergic reactions. Similar to mosquitoes, biting midges locate their hosts by detecting body odors and exhaled breath, which partly explains why some individuals are more attractive to these blood-feeding insects than others. This variation is mainly driven by differences in the skin microbiome, since bacteria are largely responsible for producing the VOC that form the odor bouquet of humans and animals.

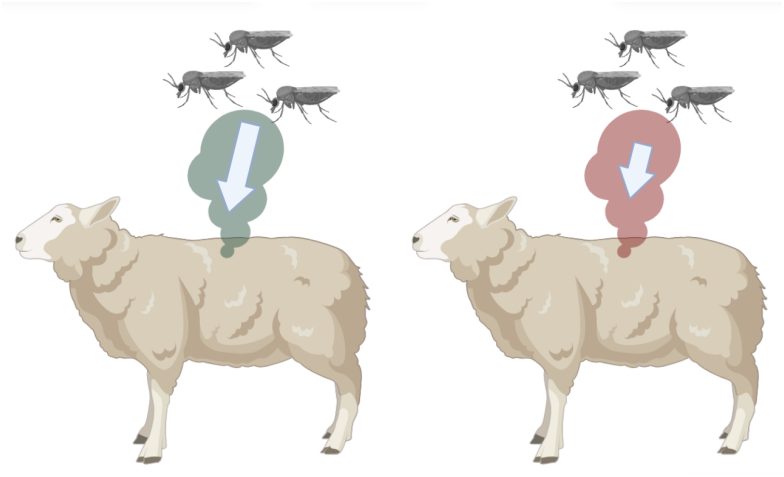

Figure 4.2: Representation of high/low attractiveness (left/right) of different sheep odors to biting midges. Created with BioRender.

In the first phase of the project, sheep were washed with bacterial strains previously shown to reduce host attractiveness. In the phase reported here, wool samples from treated animals were collected and analyzed to characterize their volatile organic compound emissions. VOC were sampled using dynamic headspace collection coupled with GC-MS analysis to be performed at a later stage. The sensor system was placed inside the measurement chamber with the wool samples to detect and monitor the released compounds. This preliminary study thus served both to validate sensor performance under realistic conditions and to provide familiarity with the experimental workflow employed in the main part of this thesis.

4.2.2 Results and Discussion

An example of an unforeseen event occurred during Batch 1, when the compressed air supply bottle ran out before the end of the collection period. This was immediately evident from the pressure gauge on the tank, but it was also clearly reflected in the sensor data. As shown in Figure 4.3, the gradual reduction of airflow corresponds to a noticeable rise in the blank signal (pink), which can be explained by the progressive inflow of laboratory air, characterized by a higher VOC concentration than the supplied synthetic air. In this sense, the sensor system acted not only as a VOC detector but also as an online diagnostic tool for monitoring the integrity of the experimental setup.

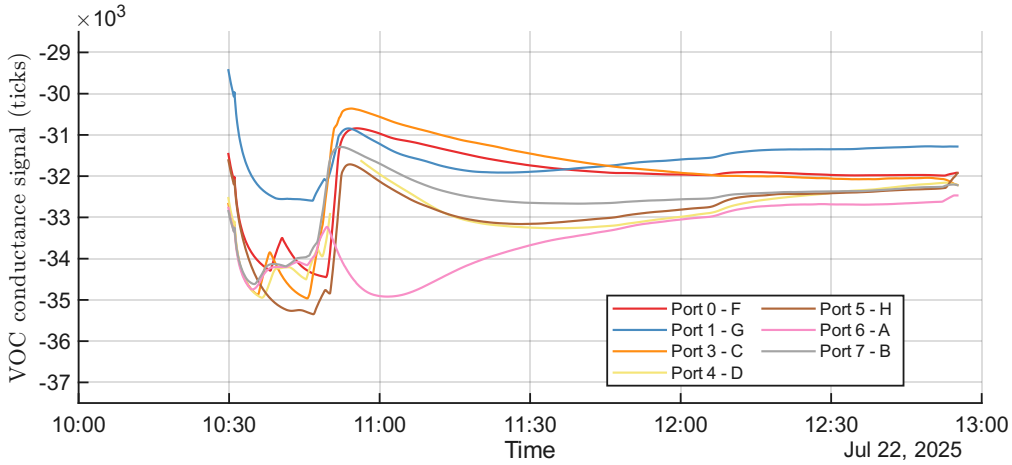

Figure 4.3: Detailed time-series of Batch 1

The presence of the sensors therefore helped pinpoint the timing of the problem, enabling a prompt decision to repeat the collection. However, the second batch also encountered a similar issue (Figure A.3a), when the backup air tank used to rerun Batch 1 was depleted during sampling. In both cases, the signal patterns were

consistent with a sudden shift in ambient composition, confirming the system's responsiveness to minor variations in air purity.

The moment of sample insertion, between 10:45 and 10:53, is also clearly visible as a step-like increase in sensor response. This transient reflects both the brief exposure of the sensors to unfiltered laboratory air during chamber opening and the sudden introduction of the wool sample's odor, which releases a burst of VOC into the headspace. Although such abrupt changes are undesirable from a measurement standpoint, they provided useful temporal markers for verifying signal alignment and confirming that the sensors responded promptly to the presence of new volatiles.

A clear distinction can be observed between the earlier batches (Figures A.3–A.5) and the later ones (Figures A.6–A.9), as illustrated in the complete set of experimental plots provided in Appendix A. In the earlier experiments, sensor recordings began after or only immediately before sample introduction, resulting in the absence of a well-defined pre-sample reference phase. In contrast, the later batches included an initial period of clean synthetic air exposure prior to sample insertion, providing a stable baseline for normalization and comparison. This procedural refinement significantly improved data consistency, enabling clearer interpretation of sensor responses to the introduced VOC.

4.3 Greenhouse Long-Term Monitoring Experiment

The experimental configuration of this greenhouse trial is described in subsection 3.3.3. Here, we provide additional background to contextualize the biological and environmental expectations before presenting the recorded sensor signals.

4.3.1 Background

Before conducting the controlled herbivory experiment, a preliminary multi-day study was performed in the greenhouse to explore the temporal dynamics of plant-emitted VOC under natural environmental fluctuations. While the laboratory experiments described in the previous sections provide controlled and reproducible conditions, understanding sensor behavior in more realistic environments is essential for assessing the feasibility of continuous monitoring applications.

It is important to note that healthy, undamaged maize plants emit only very small quantities of constitutive VOC and are considered nearly odorless under non-stress conditions [11]. Therefore, large or distinct VOC signals were not expected in the absence of herbivory. Instead, this exploratory trial focused on (i) observing day–night oscillations in VOC and environmental variables, (ii) assessing sensor behavior in the absence of stress-induced plant emissions, (iii) understanding how

greenhouse temperature, humidity, lighting and ventilation dynamics influence the measurements, and (iv) identifying potential sources of variability and confounding signals prior to the controlled herbivory experiment. As no reference analytical measurements (e.g. GC-MS) were available, the results are qualitative and serve primarily as contextual information.

4.3.2 Results and Discussion

Figure 4.4 and Figure 4.5 present representative signals from the multi-day greenhouse recording. Both sensors placed inside the plexiglass enclosures showed substantially higher relative humidity than the sensors in the open greenhouse air, reflecting reduced ventilation and the presence of moist soil in the tubes. Among the enclosed sensors, the plant-containing tube consistently reached the highest humidity values, in line with transpiration-driven moisture release, as it can be seen in Figure 4.6a.

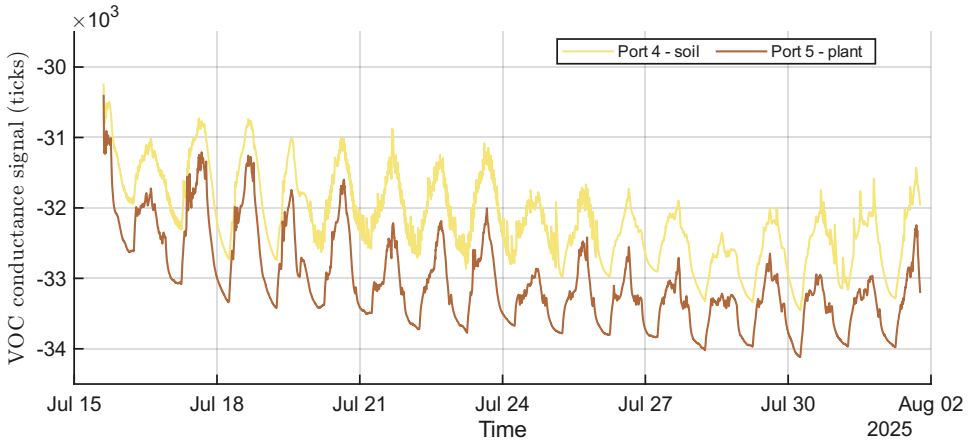

Figure 4.4: Signals recorded inside the two enclosed plexiglass tubes. The tube containing only moist soil (yellow line) shows slightly higher absolute values than the tube containing a V3 maize plant (brown line).

Contrary to initial expectations, the soil-only tube exhibited a higher mean VOC-related signal than the plant tube throughout the monitoring period. The difference between the two traces remained relatively stable, oscillating between approximately 600 and 1300 ticks depending on environmental conditions. Importantly, the temporal dynamics of both enclosed sensors were almost identical. Daily peaks in signal intensity coincided with maxima in greenhouse temperature and light.

Because no GC-MS reference data were available, this offset cannot be interpreted as a biological difference in VOC emission. Several non-exclusive explanations are more plausible. First, moist soil and associated microbial activity can generate a

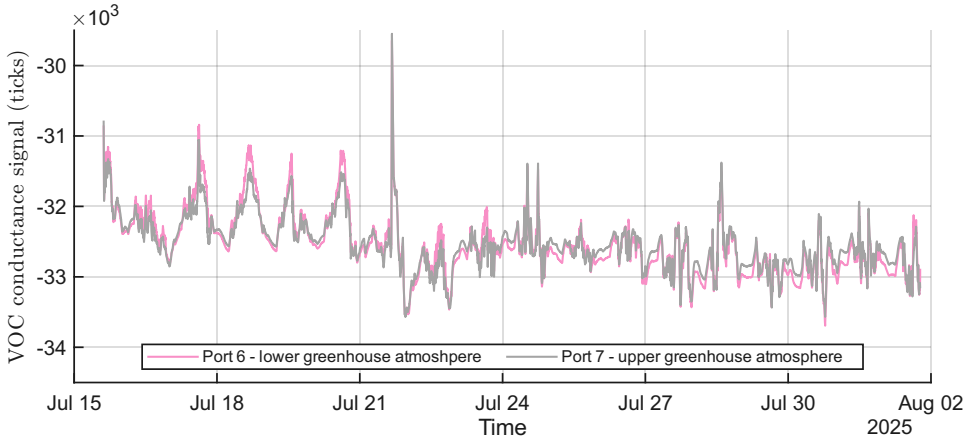

Figure 4.5: Open-air greenhouse recordings. The two sensors placed in the ambient greenhouse environment show lower signal amplitudes than the enclosed soil tube, but peak values comparable to the plant enclosure.

substantial VOC background. Second, enclosure materials such as plastics may off-gas more strongly under elevated temperatures. Third, plant physiological processes, including transpiration and stomatal behavior, may influence air exchange within the small headspace. The strong similarity in temporal patterns suggests that the observed difference reflects a persistent baseline offset rather than plant-specific emissions.

The sensors in the open greenhouse atmosphere behaved consistently with each other. Their traces followed the same diurnal pattern as the enclosed sensors but had significantly lower absolute amplitudes because of continuous dilution and ventilation. Brief signal increases occurred when the greenhouse doors were opened, illustrating the sensitivity of the system to airflow and environmental perturbations. All four sensors shared the same temperature trend as shown in Figure 4.6b.

Two qualitative conclusions can be drawn from this first greenhouse trial. Sensors exposed to the same microenvironment displayed nearly identical temporal dynamics, which indicates good reproducibility of the sensing platform. In addition, enclosure effects such as reduced airflow, elevated humidity, and accumulation of background volatiles dominated the absolute magnitude of the VOC-related signal. These observations highlighted the need for tighter control of airflow and background sources in the subsequent herbivory experiment.

Overall, this initial trial confirmed that under semi-closed greenhouse conditions the outputs of metal-oxide sensors are strongly influenced by environmental factors and enclosure characteristics. Although no biological conclusions can be drawn from these measurements, the experiment provided useful diagnostic insight into long-term drift, humidity influence, and the role of enclosure geometry.

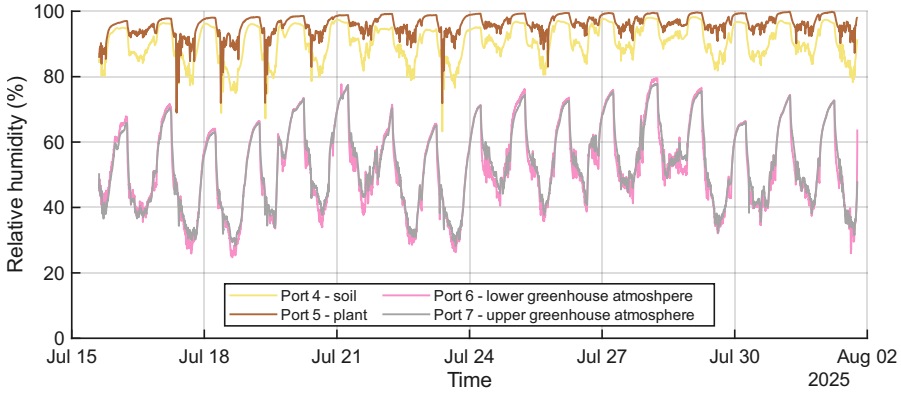

(a) RH measured in the greenhouse atmosphere and inside the plant and soil sampling tubes during the two-tube experiment.

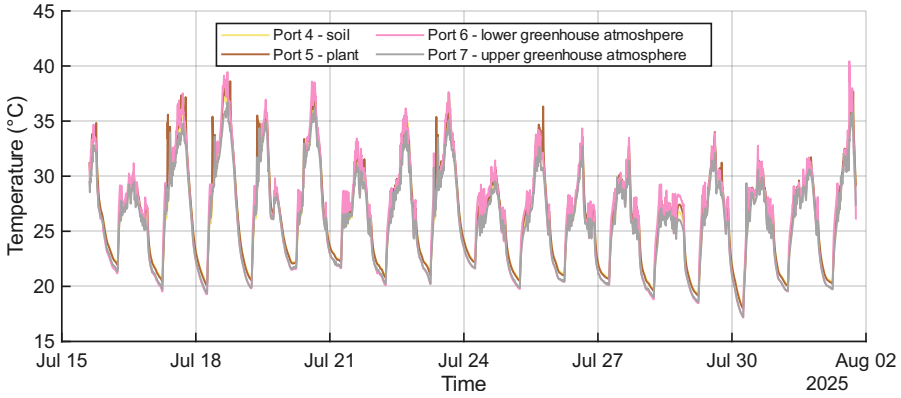

(b) Temperature recorded in the greenhouse atmosphere and inside the plant and soil sampling tubes. All positions experienced similar thermal conditions throughout the measurement period.

Figure 4.6: Environmental conditions during the greenhouse two-tube experiment: (a) relative humidity and (b) temperature in the greenhouse atmosphere and in the plant and soil enclosures.

Extended Four-Tube Greenhouse Trial

The extended four-tube greenhouse trial provided additional insight into long-term sensor behaviour under semi-confined environmental conditions. In contrast to the first two-tube experiment, where enclosed sensors exhibited different baseline dynamics, the four enclosed sensors in this extended trial showed highly similar temporal behaviour. All VOCs signals displayed pronounced diurnal oscillations driven by greenhouse temperature and light cycles, increasing during warm, bright periods and decreasing during the night.

Despite this shared temporal pattern, the four tubes differed in their absolute

signal baselines. Throughout the experiment, the empty-pot enclosure consistently produced the highest VOC signal. The soil-only enclosure showed intermediate values, while the two plant tubes exhibited the lowest signals and remained closely aligned. This ordering was maintained for almost the entire monitoring period.

The watering event on 13 August induced clear humidity changes that corresponded with shifts in the relative signal offsets. Before watering, Plant B exhibited lower humidity (approximately 72–88 percent) than Plant A (85–100 percent). After irrigation, the humidity in Plant B rose to values similar to those in Plant A, and the difference in VOC baseline between the two plant tubes decreased accordingly. The soil-only enclosure showed a comparable rise in humidity, whereas the empty-pot enclosure, which received minimal water, did not.

The full time series of VOC, humidity, and temperature measurements is presented in Figures 4.7a, 4.7b, and 4.7c. The strong similarity among the temporal patterns, combined with the persistent baseline ordering, indicates that enclosure-specific microenvironmental factors such as humidity accumulation, ventilation characteristics, and surface off-gassing dominated the sensor response. The identity of the enclosure with the highest baseline differed from that in the initial greenhouse trial, which further suggests that these differences were determined by local microenvironmental conditions rather than by variation between sensor modules.

Overall, this extended trial demonstrated that in semi-closed greenhouse environments MOSs sensor respond primarily to humidity and airflow patterns rather than to plant-emitted VOCs. An additional factor is that the plants themselves likely emitted only very low constitutive levels of volatiles during this period. In the absence of herbivory or other biotic or abiotic stress, most crop species release only minimal quantities of green-leaf volatiles and terpenoids, with emission rates several orders of magnitude lower than during induced defence responses [45, 48, 63]. Such “silent" emission profiles are typical for healthy, unstressed plants and make detection challenging for low-cost sensors operating in variable environmental conditions.

These observations motivated the use of strictly controlled laboratory conditions in the herbivory experiment, where GC-MS reference measurements provided a more reliable basis for interpreting sensor signals.

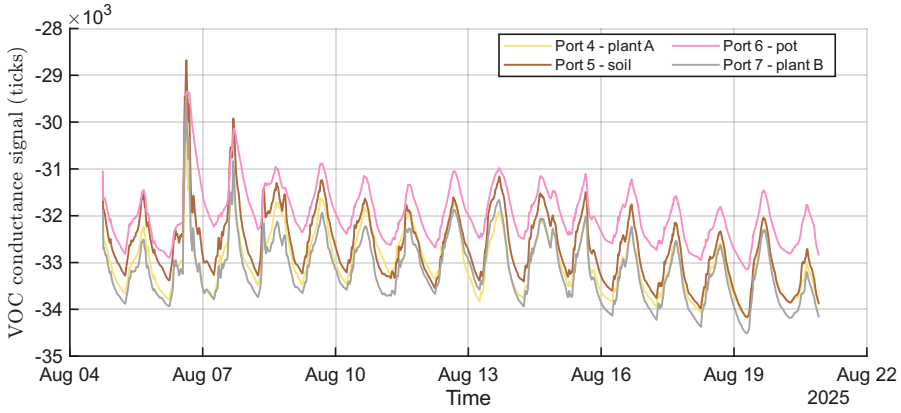

(a) VOC signal from the four enclosures over the monitoring period. All traces show clear diurnal oscillations with stable baseline offsets.

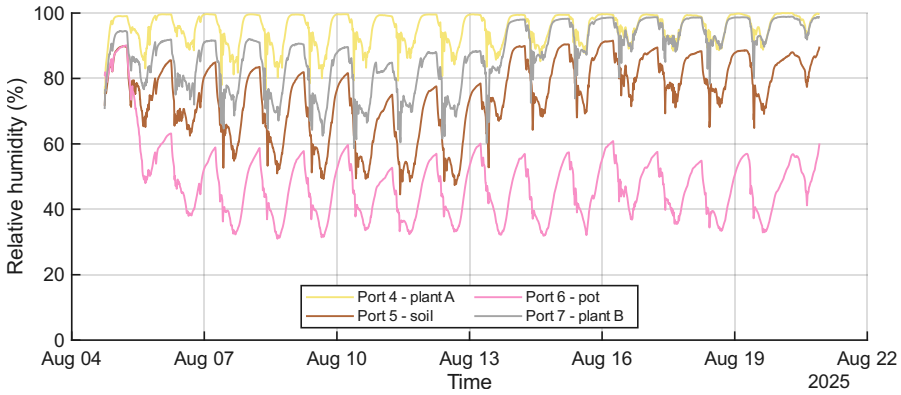

(b) Relative humidity inside the four enclosures. Watering induced step-like increases in the plant and soil tubes.

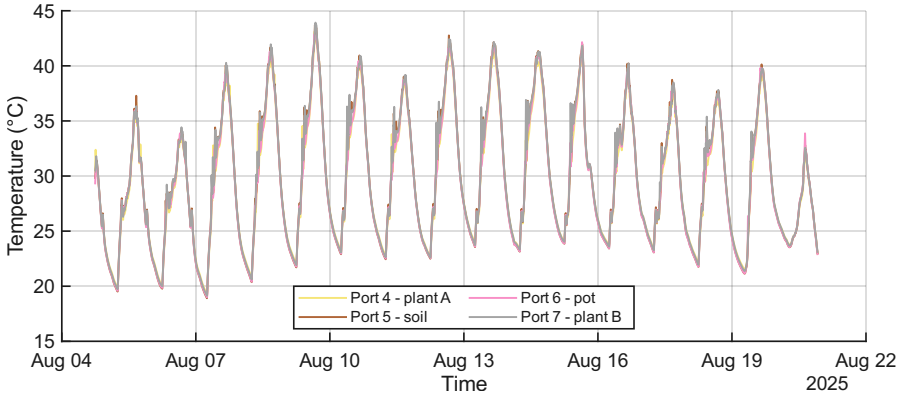

(c) Temperature inside the four enclosures, showing similar thermal conditions across all tubes.

Figure 4.7: VOC and environmental measurements from the extended four-tube greenhouse trial.

4.4 Maize Herbivory

This section describes the main experiment of this thesis, briefly recalling the concepts on plant VOCs introduced in section 2.2 and discussing the obtained sensor measurements in relation to the GC-MS reference data. In addition, it introduces essential background information on *Spodoptera littoralis*, the insect species used in the experiments, to support understanding of the experimental procedure and its biological relevance. The experimental conditions and sampling protocol for the this experiment are detailed in subsection 3.3.5.

4.4.1 Background

Plant life relies on Volatile Organic Compound for continuous communication within its ecosystem, playing critical roles in defense and signaling. In response to mechanical damage or feeding by antagonists, plants release complex chemical signals known as HIPVs [64]. These HIPVs function primarily as an indirect defense mechanism, acting as chemical cues to attract the natural enemies (predators and parasitoids) of the attacking herbivore. Additionally, HIPVs can prime the defenses of neighboring or systemic plant tissues, enhancing resistance to future stress [65]. VOC emission patterns are highly plastic and serve as sensitive, non-invasive markers for monitoring biotic stress [9].

Maize (*Zea mays* L.) is widely utilized as a model system for investigating chemical ecology and tritrophic interactions due to its global agricultural importance and its robust, inducible volatile response [48, 63, 49, 50, 39]. Crucially, maize production of specific volatiles is triggered by elicitors found in caterpillar oral secretions, allowing the plant to differentiate herbivory from mere mechanical damage [64].

The insect species *Spodoptera littoralis* (Boisduval), commonly known as the Egyptian cotton leafworm, belongs to the class Insecta, order Lepidoptera, family Noctuidae [66, 67]. It is a highly polyphagous pest of global agricultural concern, known to feed on more than 100 plant species across over 40 families, including key crops such as cotton, soybean, maize, tomato, and various vegetables and ornamentals. Native to Africa, *S. littoralis* is now established throughout the Mediterranean Basin, the Middle East, and parts of Southern Europe, where mild winters allow it to persist year-round. Its wide host range and capacity to migrate and reproduce under a range of climatic conditions make it a major threat to temperate agriculture.

(a) 1st (right) and early 2nd instar.

(b) 2nd (left) and early 3rd instar.

(c) 4th instar.

Figure 4.8: *S. littoralis* instar stages. Photos by M. vd Straten © NPPO, The Netherlands [67].

The larval stage is the most damaging phase of the life cycle. Newly hatched larvae initially feed gregariously, scraping the epidermis from the underside of young leaves, while later instars become solitary and consume entire leaf sections, leading to defoliation and yield loss. Pupation occurs in the soil, and adults emerge as nocturnal moths that are strong fliers and can disperse over considerable distances, contributing to seasonal infestations [66, 67].

Beyond its economic impact, *S. littoralis* serves as a well-established model organism for studying herbivory-induced plant responses, owing to its predictable feeding behavior and the consistent induction of defense signaling in host plants such as maize. Feeding damage or exposure to larval oral secretions, containing specific elicitors like volicitin, triggers the production of HIPVs, including GLV (Green Leaf Volatile), terpenoids, and indole [45, 48]. These compounds mediate complex tritrophic interactions by attracting the natural enemies of the herbivore and modulating the defensive state of neighboring plants. Consequently, *S. littoralis*–maize interactions represent an ideal experimental model for investigating plant volatile emission dynamics under controlled conditions.

Maize responds to *S. littoralis* damage by emitting characteristic HIPV blends. This emission occurs in distinct phases: an immediate release of GLVs, fatty acid derivatives such as (*Z*)-3-hexenal, (*E*)-2-hexenal, and (*Z*)-3-hexen-1-yl acetate, which signal acute tissue damage. This initial burst is followed, hours later, by the systemic release of newly synthesized compounds, primarily terpenoids and aromatic compounds [48]. Key induced metabolites include homoterpenes like DMNT ((*E*)-4,8-dimethyl-1,3,7-nonatriene), sesquiterpenes such as β-caryophyllene, and indole, a shikimate-derived compound acting as a priming signal in maize [38, 51]. The specific profile of these induced metabolites (GLVs, terpenoids, indole) varies depending on the maize genotype and the timing of the attack [49].

The distinct, time-dependent chemical signatures produced by maize during

herbivory are critical targets for plant health monitoring [43]. To move HIPV monitoring from controlled laboratory environments to practical field applications, this research employs low-cost MOS (Metal Oxide Semiconductor) gas sensors for rapid and continuous detection [1, 5]. To ensure the accuracy and reliability of the data obtained from these lower-fidelity sensors, laboratory validation is crucial. Therefore, performing controlled experiments using both the emerging MOS sensing technology and the high-precision analytical capabilities of GC-MS (Gas Chromatography–Mass Spectrometry) is necessary to reliably interpret the complex HIPV profiles associated with *S. littoralis* herbivory in maize [5, 2].

4.4.2 Results and Discussion

The results from the maize herbivory experiment revealed clear differences in volatile emission dynamics between the two experimental batches, largely reflecting the variability in larval feeding activity. In Batch 1, the larvae placed on the plants during the evening did not feed overnight, and additional individuals were introduced the following morning. Consistent with this limited early damage, both the MOS sensor responses and the GC-MS reference data showed only minimal induction in the *Spodoptera*-treated plants (SpoM). In particular, SpoM05 displayed no detectable difference from the control maize (CM) plants in its GC-MS profile and also showed no visible feeding marks, confirming the absence of herbivory-induced VOC emission, thus it was classified as control.

To better illustrate the biological conditions underlying the contrasting VOC profiles in the two batches, Figure 4.9 shows representative leaf damage on SpoM01 and SpoM06 at the time of dynamic headspace sampling.

(a) SpoM01 (Batch 1). Only limited feeding damage was present at the time of dynamic headspace sampling.

(b) SpoM06 (Batch 2). Substantial feeding damage was already present at the start of sampling.

Figure 4.9: Comparison of leaf damage between SpoM01 (Batch 1) and SpoM06 (Batch 2) at the time of dynamic headspace collection. The limited early feeding in Batch 1 explains the weak and poorly structured VOC emissions, whereas the sustained herbivory in Batch 2 produced stronger and more temporally coherent VOC signatures.

Accordingly, the sensor curves of Batch 1 (Figure 4.13) remained nearly indistinguishable between CM and SpoM chambers until after the beginning of the photoperiod (Figure 4.13a). After this point, additional larvae were placed onto the plants, visible as small drops in the VOC signal caused by handling the domes, and feeding likely began shortly thereafter. The perturbations observed in the conductance traces occurred only later, following the opening of the air supply (Figure 4.10), consistent with the expected timing of induced volatile emission occurring several hours after the onset of herbivory [48]. These transient features, absent in CM, likely reflect the early stages of induced volatile release and may have been amplified by the drop in relative humidity following the opening of the air supply (Figure 4.13b). Temperature remained stable across ports and did not appear to influence sensor behavior (Figure 4.13c).

Interestingly, CM01 exhibited a marked increase in MOS sensor signal during the

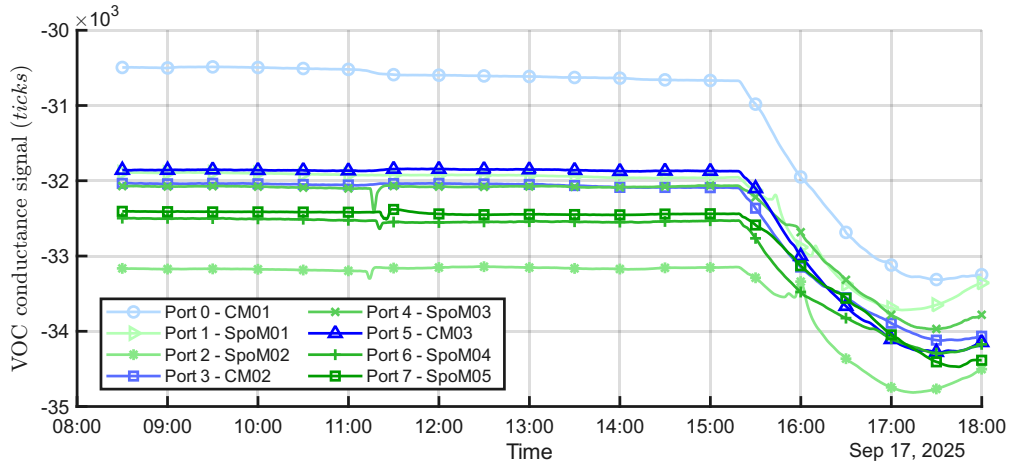

Figure 4.10: Zoomed view of VOC conductance during Batch 1, showing the beginning of the photoperiod (lights on at 08:30) and the moment the air supply was opened for dynamic headspace collection.

night period, a pattern not observed in the other control plants. The corresponding GC-MS profile revealed substantially higher levels of 4-hydroxybenzaldehyde and cyclosativene compared to the remaining CM and SpoM samples. Because CM01 experienced no herbivory and showed no visible damage, this atypical emission pattern is unlikely to be related to insect feeding. Instead, it may reflect localized processes such as microbial activity on plant or pot surfaces (e.g., fungi or bacteria contributing phenolic and sesquiterpene volatiles)[68]. Without dedicated microbiological data, this interpretation remains speculative, but it highlights that control chambers can occasionally display VOC signatures that are not strictly "background" in a biological sense.

In contrast, Batch 2 exhibited continuous herbivory from the start of the recording period, resulting in more temporally structured VOC responses. While all chambers showed the expected nocturnal decrease in VOC emission, a clear daytime increase was evident primarily in SpoM06, which experienced the strongest feeding activity (Figure 4.11). An exception was port 7 (CM04), which displayed substantially higher conductance values than the other CM plants. This artifact was traced back to the cleaning procedure between batches: a small amount of ethanol was used to remove larvae from the glass dome of Batch 1, and insufficient venting time likely resulted in residual vapors persisting inside the chamber at the start of Batch 2. This affected the MOS sensor response but not the GC-MS measurements as Tenax TA does not retain well molecules outside its range (from n-C_6 to n-C_{26}). For this reason, the plotting scale for the Batch 2 VOC traces was adjusted to prevent CM04 from dominating the y-axis. Notably, when the air supply

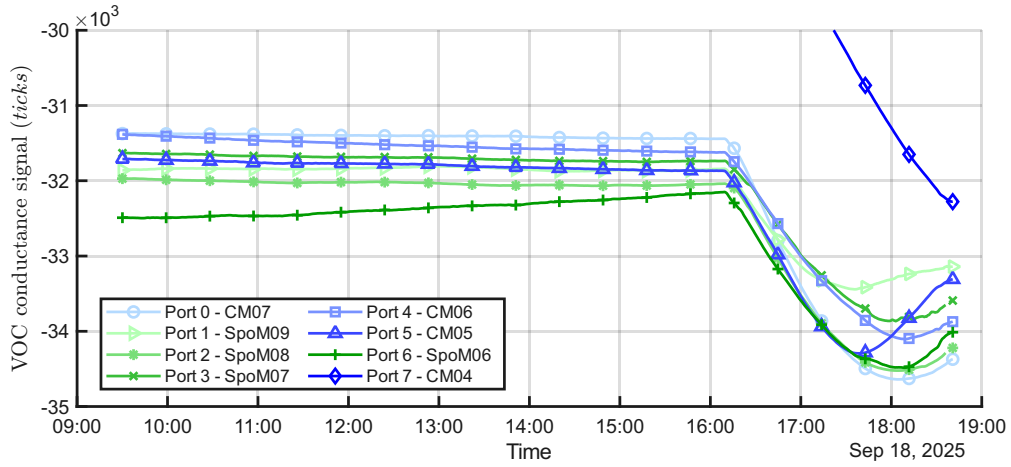

Figure 4.11: Zoomed view of VOC conductance during Batch 2, from the moment lights were turned on and highlighting the onset of dynamic headspace collection when the air supply was opened.

was opened, the CM04 signal decreased sharply, although it did not return fully to baseline levels during the experiment. The corresponding VOC conductance curves are shown in Figure 4.14a. Relative humidity and temperature followed patterns comparable to those observed in Batch 1 (Figure 4.14b and Figure 4.14c), indicating that the differences between the batches stemmed primarily from herbivory progress rather than environmental variation. Unlike Batch 1, no pronounced perturbation was associated with the air-supply phase, likely because the plants had already begun emitting induced volatiles prior to this event.

4.4.3 GC-MS Reference Data

The normalized GC-MS data (see Figure 4.12) revealed clear differences between the two experimental batches, consistent with the distinct feeding patterns observed in the sensor measurements. Overall, Batch 2 exhibited substantially higher amounts of herbivory-related volatiles compared to Batch 1. This was expected, as larvae in Batch 2 had been feeding continuously before and during sampling, whereas in Batch 1 feeding only began shortly before the VOC collection period.

Across both batches, the chemical composition of the headspace was dominated by three main classes of compounds: (i) green-leaf volatiles (GLVs) such as hexanal, *(E)*-3-hexenal, and their acetate derivatives; (ii) terpenoids including limonene, *trans*-β-ocimene, and DMNT; and (iii) minor contributions from aromatic compounds and aldehydes. As expected for maize under herbivory, several terpenoids showed particularly strong induction in SpoM samples of Batch 2, most notably *trans*-β-ocimene, DMNT, and β-farnesene, which are characteristic markers of

systemic HIPV release. Notably, within Batch 2, SpoM06 stood out by producing particularly high amounts of α-bergamotene and sabinene, sesquiterpenes associated with strong or progressing herbivore damage [46, 45].

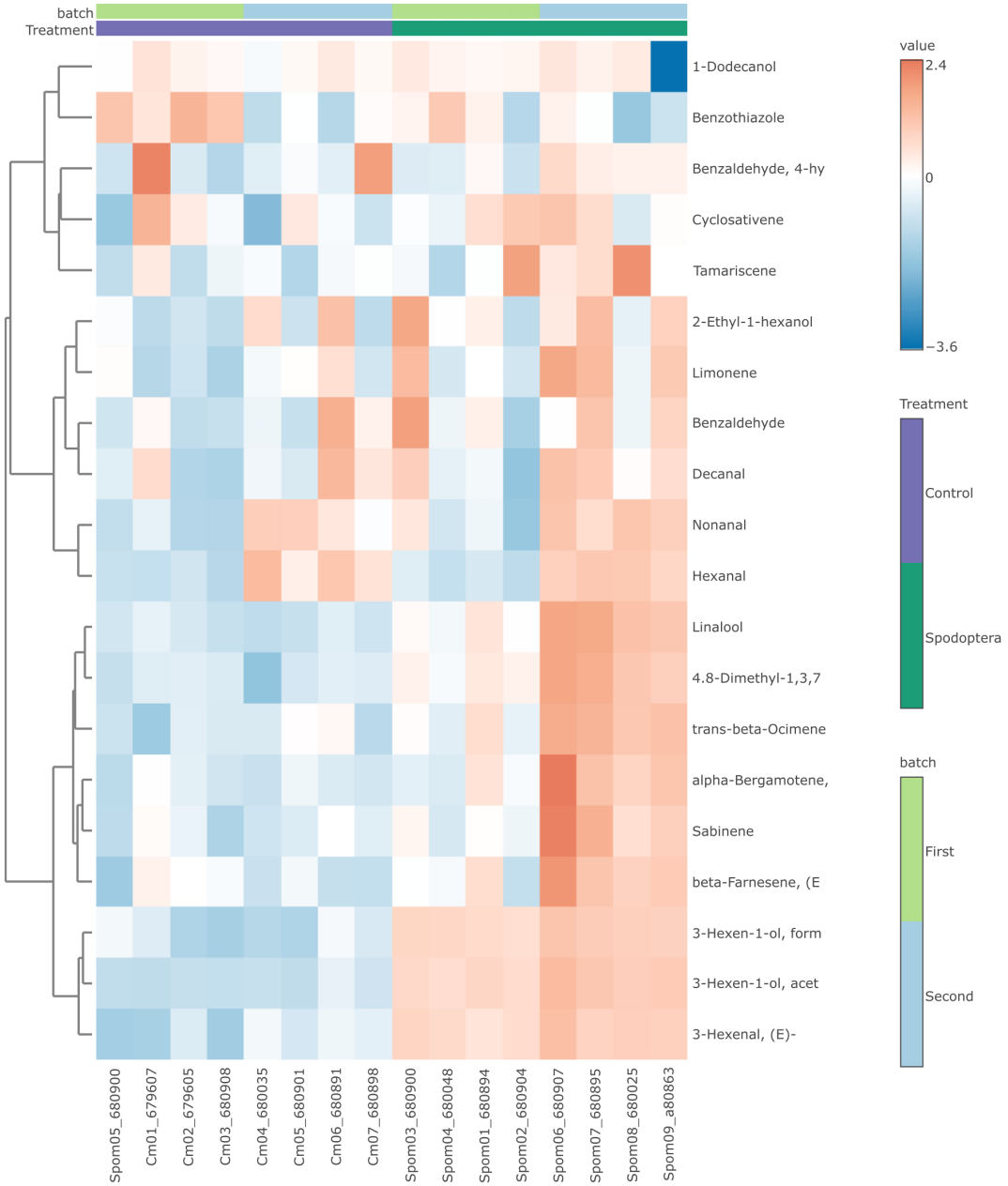

Figure 4.12: Autoscaled heatmap of GC–MS peak intensities across CM and SpoM samples in the two experimental batches.

In contrast, Batch 1 showed overall lower abundances for these compounds, reflecting the limited damage prior to sampling. A notable exception was CM01, which displayed elevated amounts of 4-hydroxybenzaldehyde and cyclosativene relative to the other controls. Since no herbivory occurred on this plant, this atypical profile likely reflects non-herbivory-related processes such as local microbial activity or individual plant metabolic variation. Apart from this outlier, the CM samples of both batches clustered tightly and showed consistently low emission across all major compound classes, confirming that the observed increases in Batch 2 arise from active larval feeding rather than environmental differences between batches.

A further difference between the batches is visible in the GC-MS data: the control plants of Batch 2 showed slightly higher amounts of several volatiles, particularly hexanal and nonanal, compared to the controls of Batch 1. Since these GLVs often increase in plants exposed to airborne cues from damaged neighbors, this elevation may reflect a mild induction caused by volatiles released during the preceding herbivory experiment. As shown by Skoczek *et al.* [63], several of these aldehydes are inducible compounds whose emission increases under both direct feeding and exposure to HIPVs from neighboring plants.

Overall, the maize herbivory experiments showed that low-cost MOS sensors can resolve time-dependent changes in plant volatile emissions associated with *S. littoralis* feeding. When herbivory was sustained (Batch 2), the sensors differentiated actively damaged plants from controls, in agreement with the GC-MS data that revealed strong induction of characteristic HIPV markers such as GLVs, terpenoids, and DMNT. At the same time, the experiments highlighted important sources of variability and potential confounding factors, including plant-to-plant differences, residual contaminants in the enclosures, and low-level induction of control plants by airborne cues. These findings underline both the promise and the current limitations of using commercial MOS devices for ecological VOC monitoring. The next chapter summarizes the main outcomes of this work and discusses their implications for future applications and methodological developments.

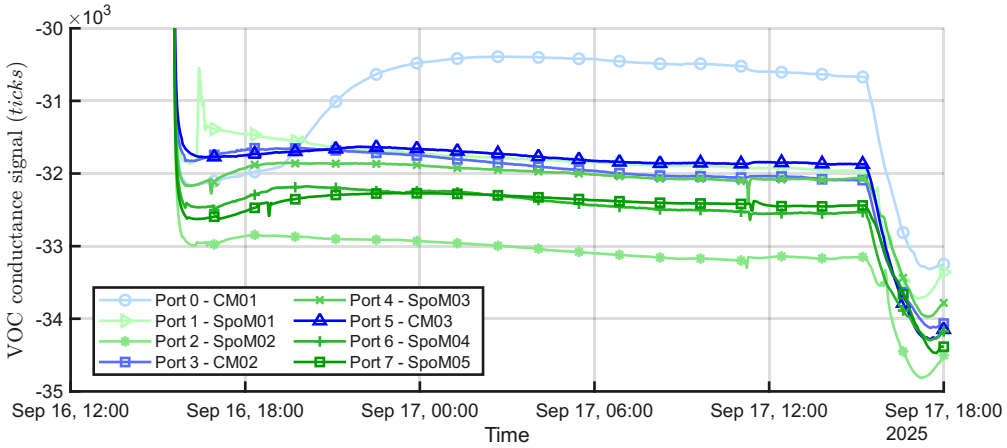

(a) VOC-related conductance measured during Batch 1.

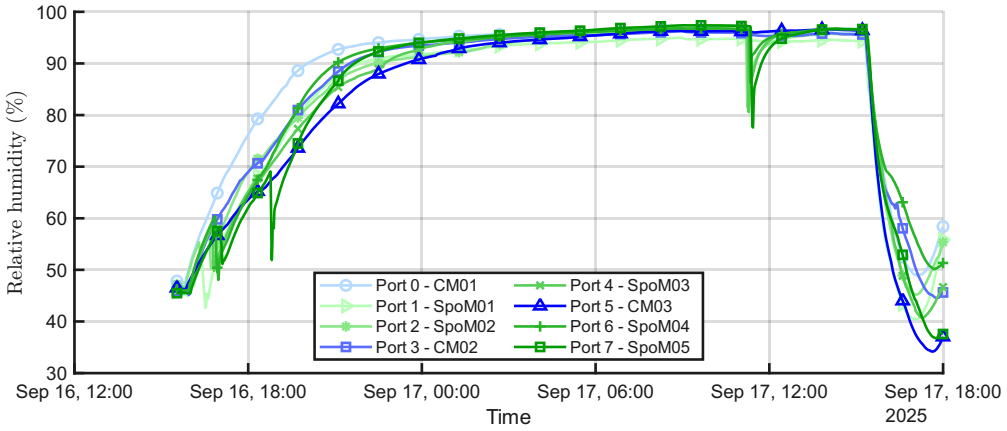

(b) Relative humidity inside the enclosures during Batch 1.

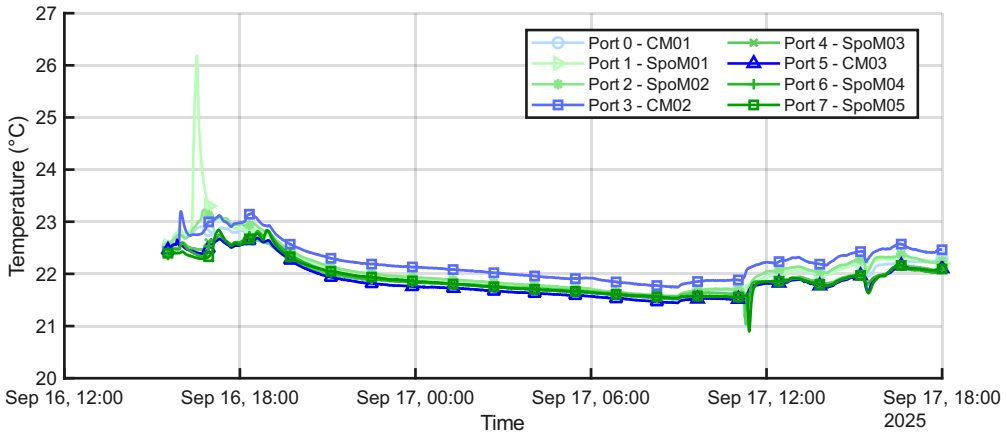

(c) Temperature measured inside the enclosures during Batch 1.

Figure 4.13: Environmental and VOC-related measurements acquired by the sensor array during the first maize herbivory experiment (Batch 1).

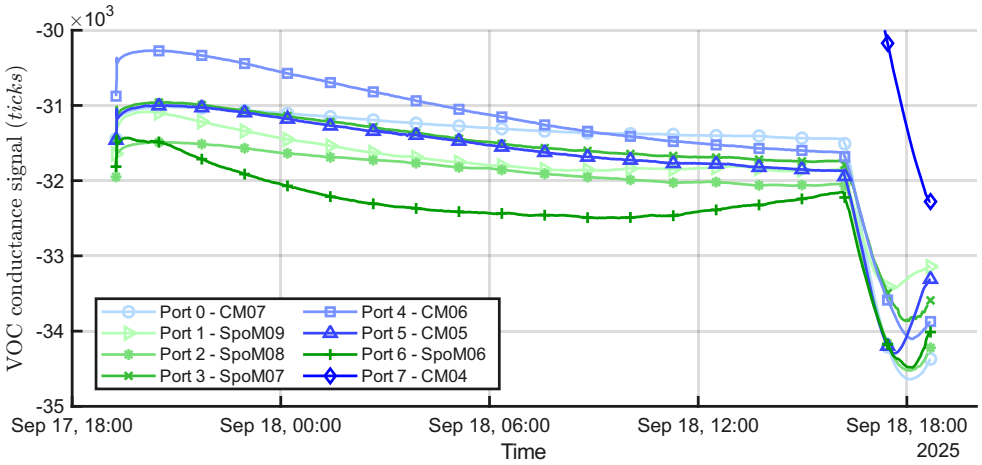

(a) VOC-related conductance during Batch 2.

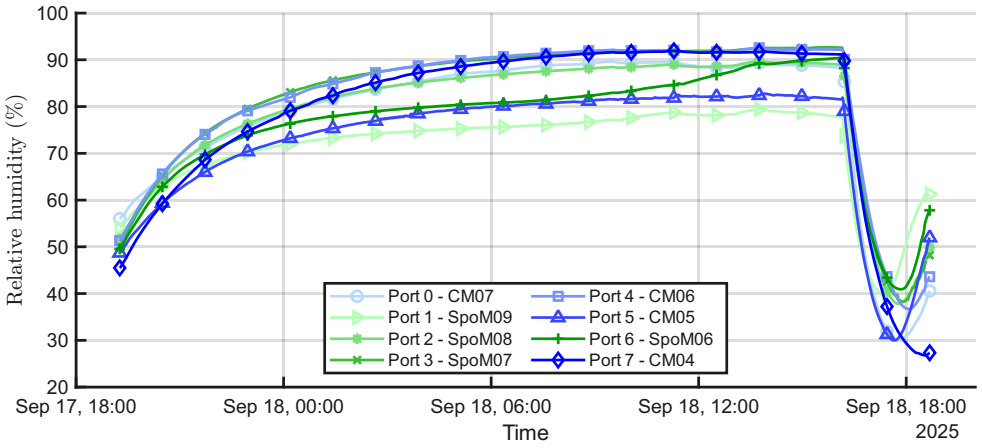

(b) Relative humidity inside the enclosures during Batch 2.

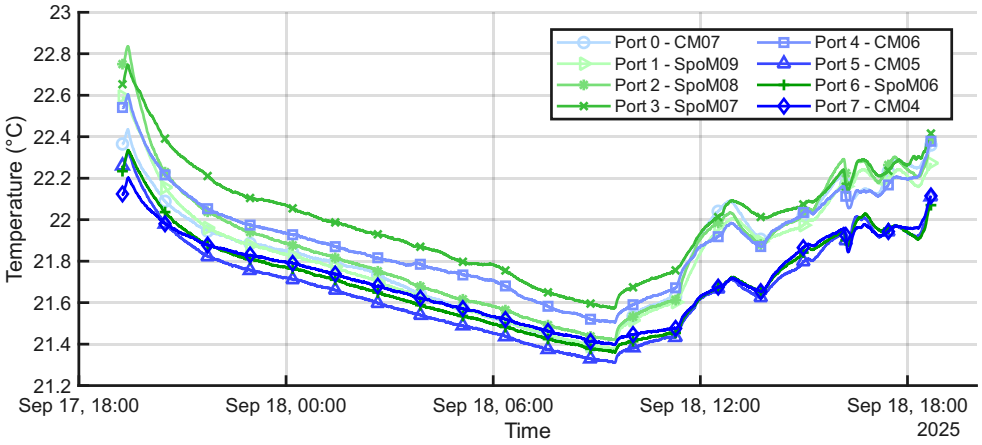

(c) Temperature inside the enclosures during Batch 2.

Figure 4.14: Environmental and VOC-related measurements acquired by the sensor array during the second maize herbivory experiment (Batch 2).

4.5 Conclusion

This thesis evaluated the performance of a low-cost MOS gas sensor platform for the detection of plant-emitted VOCs under controlled laboratory conditions. Across three experimental stages (sheep wool validation, greenhouse monitoring, and herbivory-induced emissions in maize) the system demonstrated the ability to track relative changes in volatile release, despite the inherent limitations of low-cost sensor technology.

The preliminary wool experiments provided a stable reference system and enabled characterization of sensor behavior, including baseline drift, overshoot effects, and cross-sensitivity to humidity and temperature. These trials demonstrated that the platform was sufficiently stable for long-duration measurements and highlighted the importance of environmental conditions and sensor orientation when interpreting raw MOS signals.

Experiments in the greenhouse environment offered insight into system performance under semi-controlled but biologically realistic conditions. The sensors accurately followed the diurnal cycles of the greenhouse, with clear responses to temperature-driven ventilation changes and plant transpiration. Although no chemical reference method was available in these trials, the measurements confirmed that enclosed plants produced stronger signals than open-air conditions, reinforcing the potential usefulness of such platforms for continuous crop monitoring.

The herbivory experiment on maize plants constituted the core of this work. The system successfully detected differences in VOCs emission between control maize (CM) and *Spodoptera*-treated plants (SpoM), with clear temporal patterns corresponding to the light regime, feeding activity, and dynamic headspace sampling. Batch 2, in which larvae fed continuously prior to measurement, showed a much stronger induction of HIPVs than Batch 1, consistent with the temporal dynamics of volatile induction described in the literature. These qualitative differences were confirmed by GC-MS analysis, particularly for key compounds such as GLVs, monoterpenes, and the homoterpene DMNT. Within Batch 2, SpoM06 exhibited especially high levels of α-bergamotene, sabinene, *trans*-β-ocimene, DMNT, and β-farnesene , matching the marked rise observed in its sensor signal and indicating a strong systemic herbivory response.

Across all experiments, the results demonstrate that low-cost MOS sensors can detect herbivory-induced changes in maize VOCs at a qualitative level and reliably capture large variations in emission magnitude. However, the findings also highlight important limitations. The sensors lack chemical selectivity, exhibit cross-sensitivity to humidity, and require careful calibration to avoid confounding effects such as residual chamber contaminants. Biological variability, particularly inconsistent feeding behavior, emerged as a major source of experimental noise.

Furthermore, the study did not employ machine learning or deep learning approaches for signal processing, partly due to the hardware complexity, limited dataset size, and increased total cost of ownership that such methods would entail. Advanced data-driven techniques could substantially enhance pattern recognition and discrimination power once larger curated datasets become available.

Biological limitations also influence the interpretation of the results. The experiments did not include treatments with standardized oral secretion or insect extract, which could provide controlled and reproducible induction of HIPVs. Control plants in Batch 2 showed slightly elevated levels of constitutive GLVs, likely due to airborne exposure to volatiles emitted during Batch 1, illustrating the sensitivity of maize to inter-plant communication.

Future work should therefore focus on improving both the sensing system and the experimental methodology. On the technical side, integrating temperature and humidity compensation algorithms, applying multivariate or machine learning models for signal interpretation, and exploring sensor arrays with complementary materials would enhance selectivity and robustness. On the biological side, standardizing herbivory induction, expanding sample size, and conducting controlled exposure experiments with isolated HIPVs or oral secretion extracts would reduce variability and enable stronger cross-validation. Finally, coupling the system with portable GC or miniaturized preconcentration units could transform it into a powerful hybrid platform for field-ready plant monitoring.

In summary, this thesis establishes a methodological basis for the use of low-cost MOS-based platforms in plant volatile sensing and demonstrates their applicability for detecting herbivory-induced changes in maize. While further refinement and validation are required before such systems can be deployed outside controlled environments, the results highlight their promise as accessible tools for continuous crop health monitoring and precision agriculture.

Appendix A

Raw Time Series Plots Sheep Wool VOC

This appendix reports the complete time series of the VOC sensor responses and environmental measurements (temperature and humidity) for each experimental batch performed in the sheep wool experiment described in section 4.2. Each pair of plots shares the same time axis for direct comparison of signal variations and environmental conditions. On later experiments the orientation of the sensor module was recorded and the information is included in the legend, marked as either `side`, `up` or `down`, and if the chamber contained an empty Petri dish `blank` was also included.

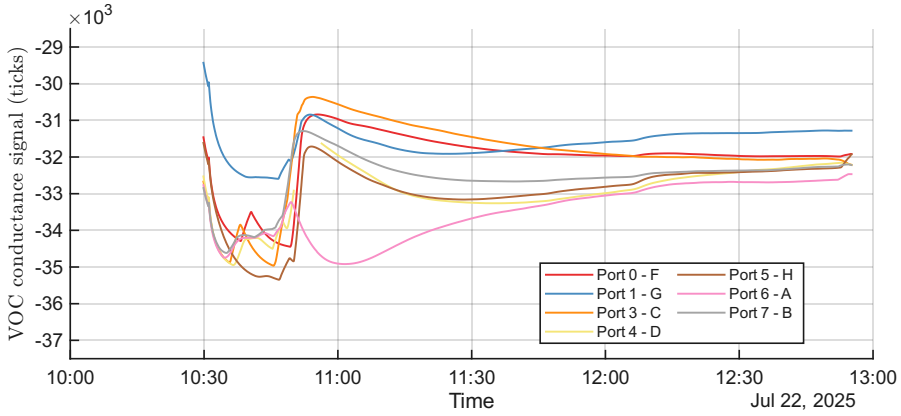

(a) VOC sensor responses during Batch 1.

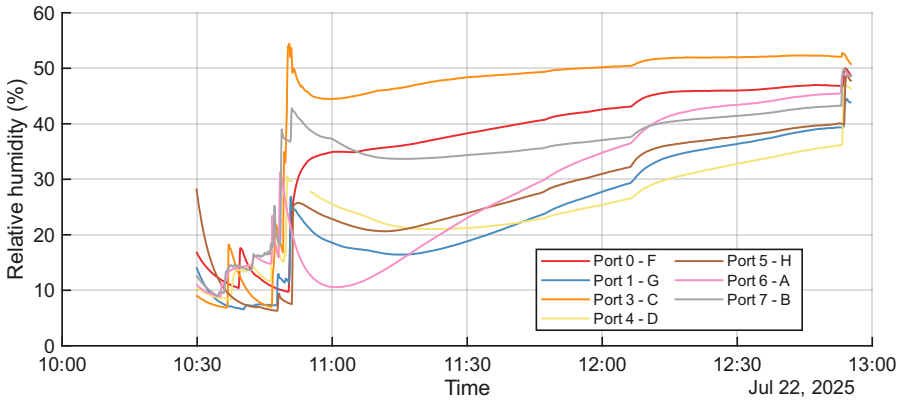

(b) Humidity during Batch 1.

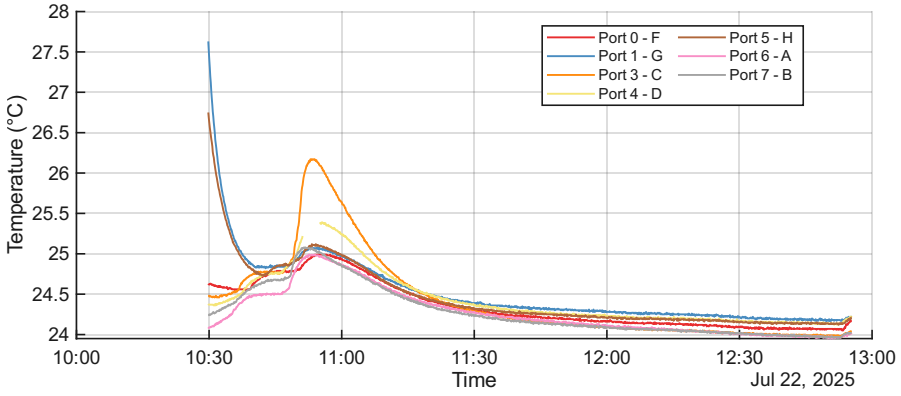

(c) Temperature during Batch 1.

Figure A.1: VOC and environmental sensor responses during Batch 1. All plots share the same time scale.

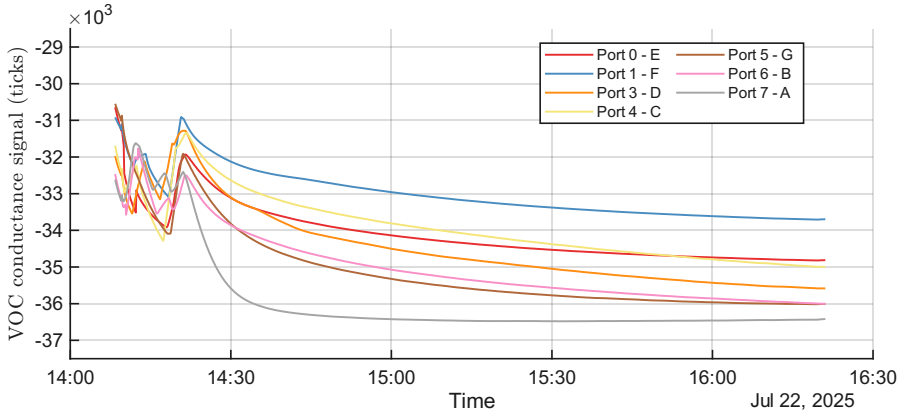

(a) VOC sensor responses during Batch 1 retake.

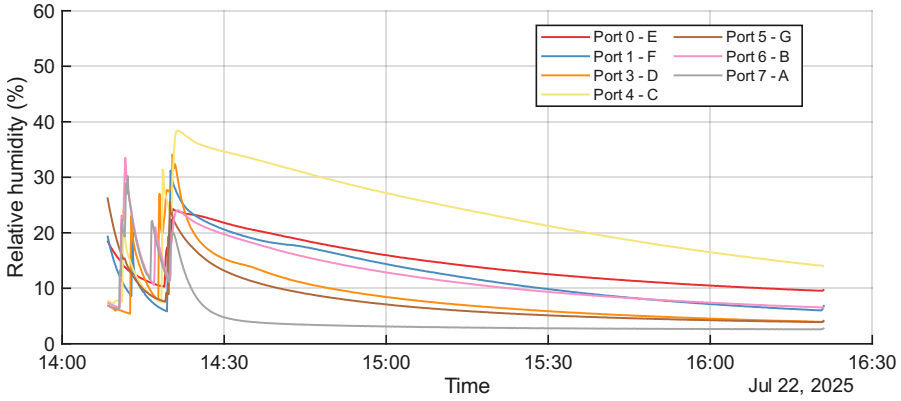

(b) Humidity during Batch 1 retake.

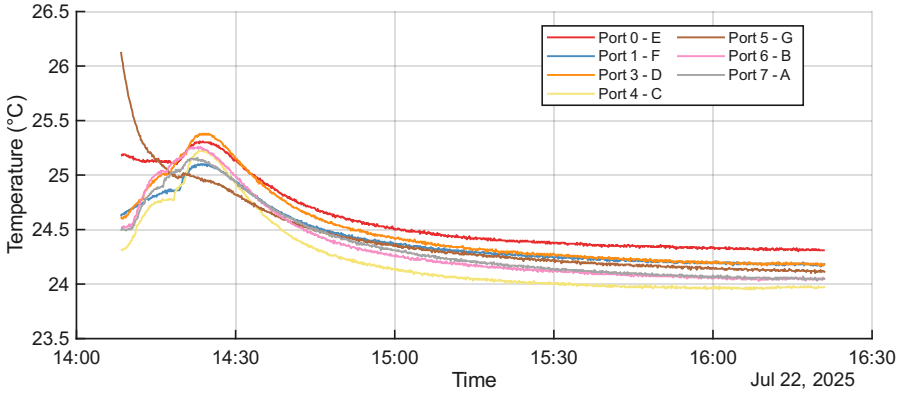

(c) Temperature during Batch 1 retake.

Figure A.2: VOC and environmental sensor responses during Batch 1 retake. All plots share the same time scale.

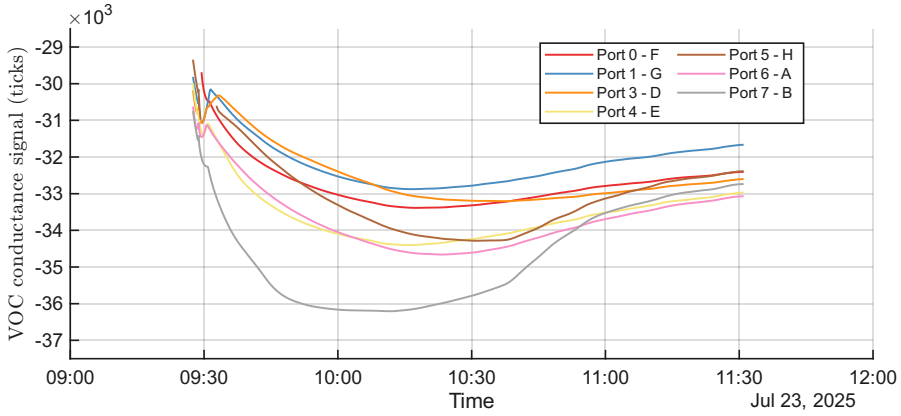

(a) VOC sensor responses during Batch 2.

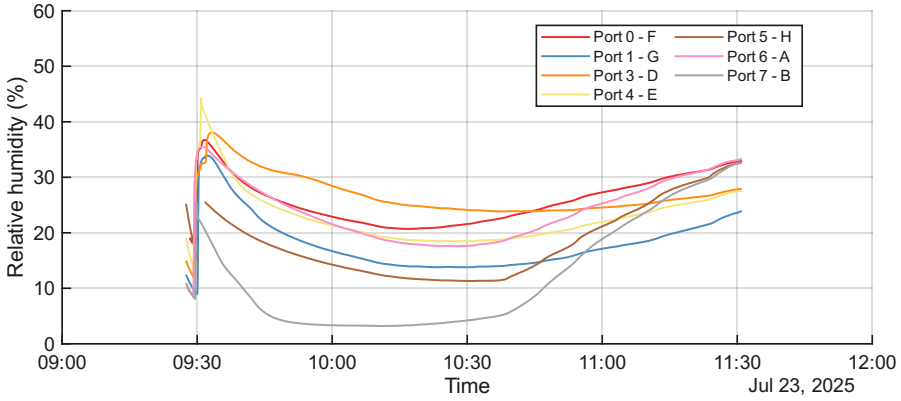

(b) Humidity during Batch 2.

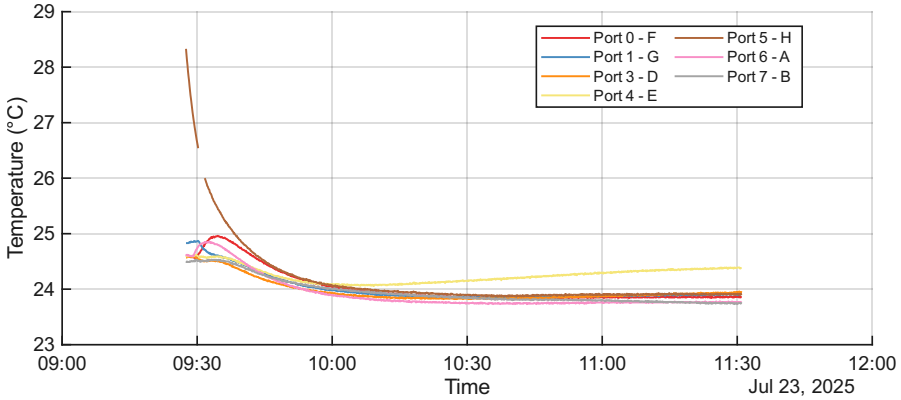

(c) Temperature during Batch 2.

Figure A.3: VOC and environmental sensor responses during Batch 2. All plots share the same time scale.

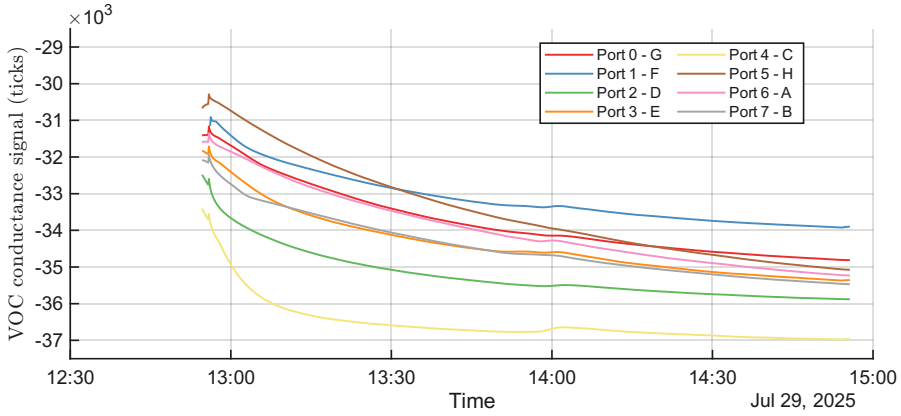

(a) VOC sensor responses during Batch 3.

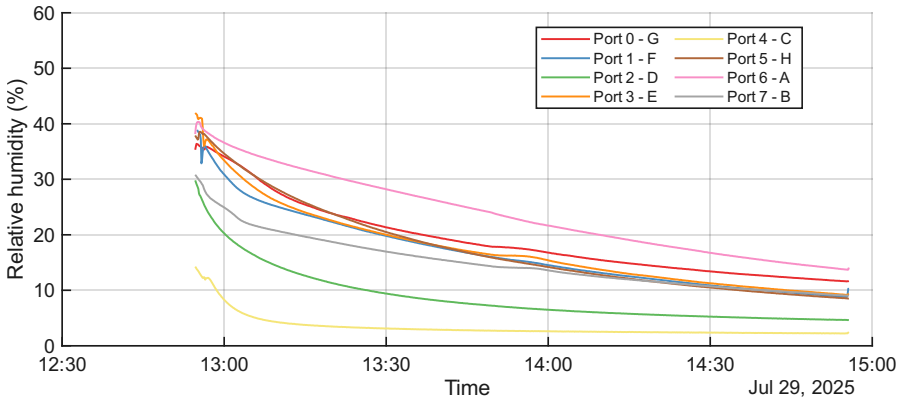

(b) Humidity during Batch 3.

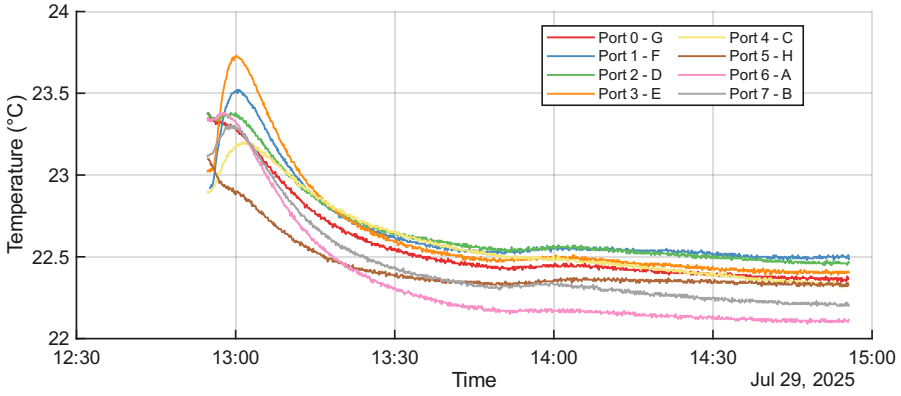

(c) Temperature during Batch 3.

Figure A.4: VOC and environmental sensor responses during Batch 3. All plots share the same time scale.

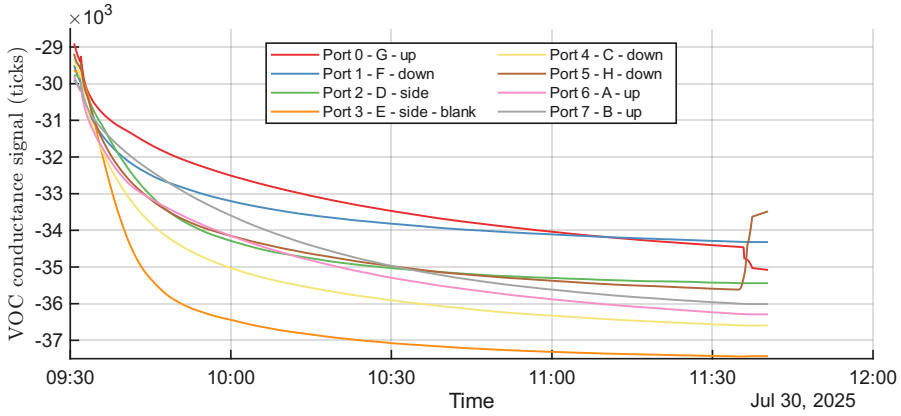

(a) VOC sensor responses during Batch 4.

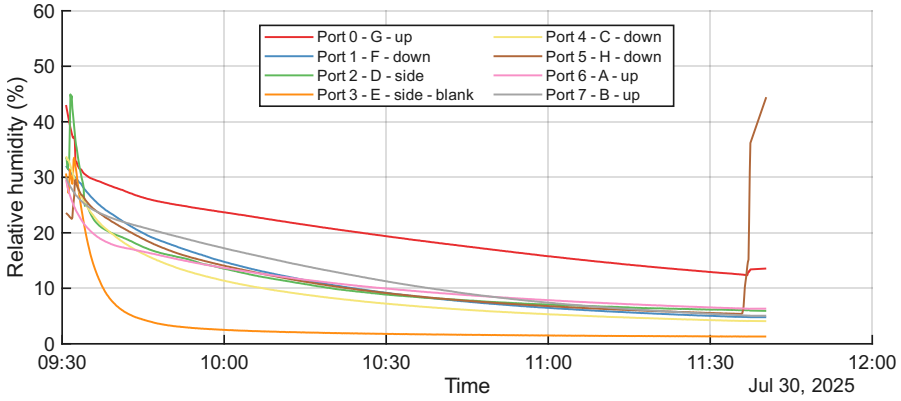

(b) Humidity during Batch 4.

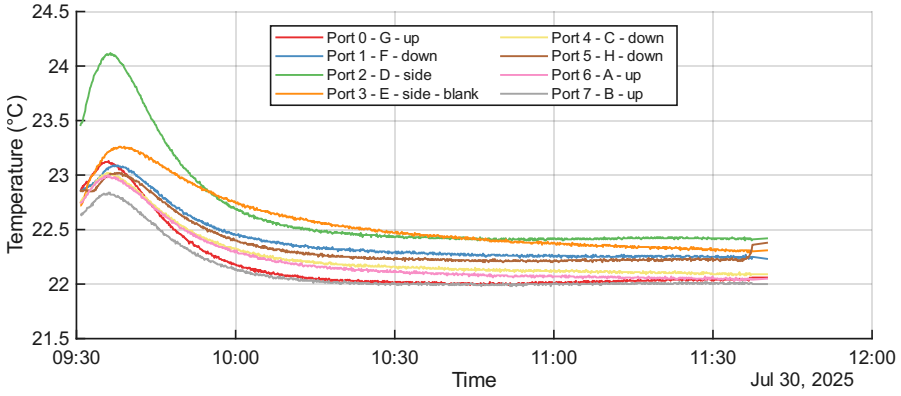

(c) Temperature during Batch 4.

Figure A.5: VOC and environmental sensor responses during Batch 4. All plots share the same time scale.

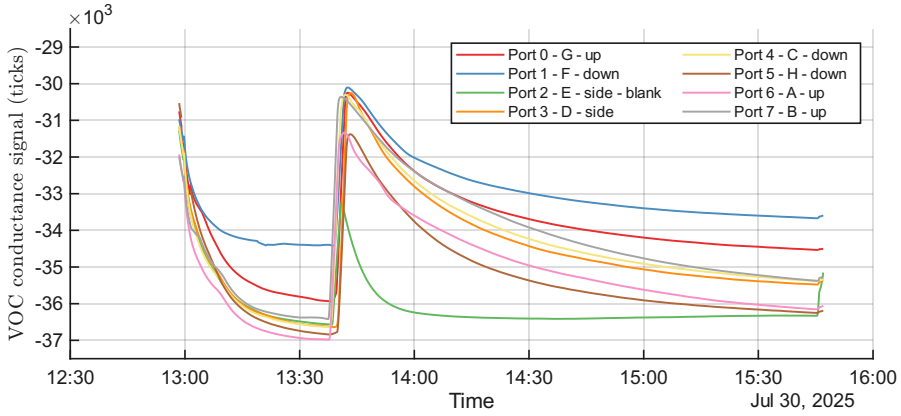

(a) VOC sensor responses during Batch 5.

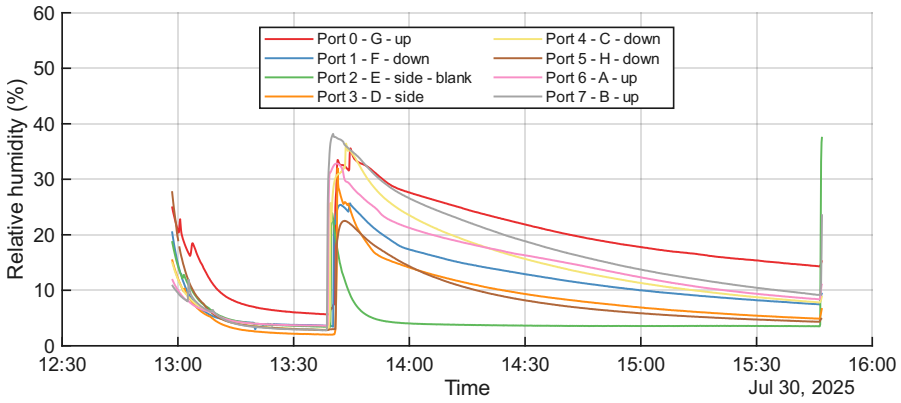

(b) Humidity during Batch 5.

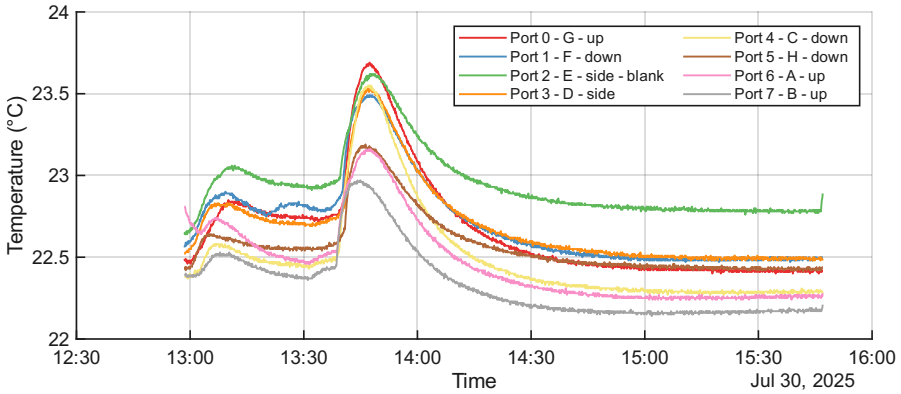

(c) Temperature during Batch 5.

Figure A.6: VOC and environmental sensor responses during Batch 5. All plots share the same time scale.

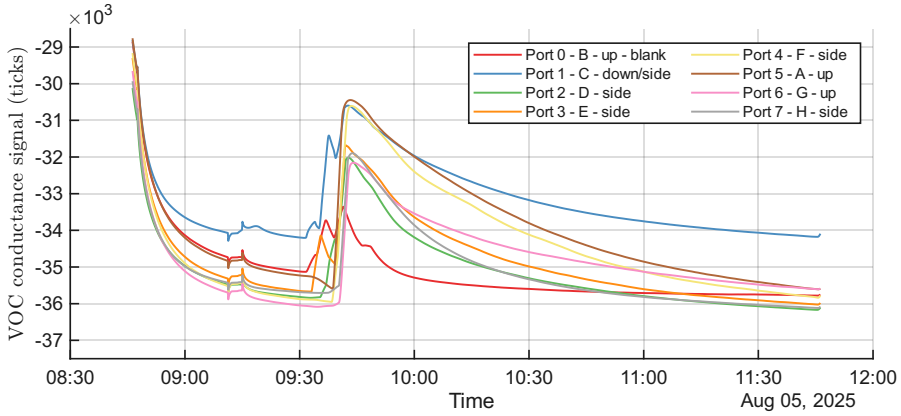

(a) VOC sensor responses during Batch 6.

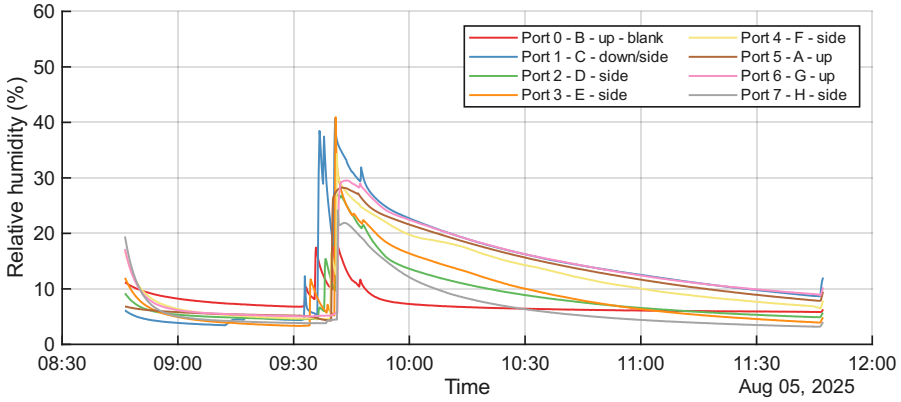

(b) Humidity during Batch 6.

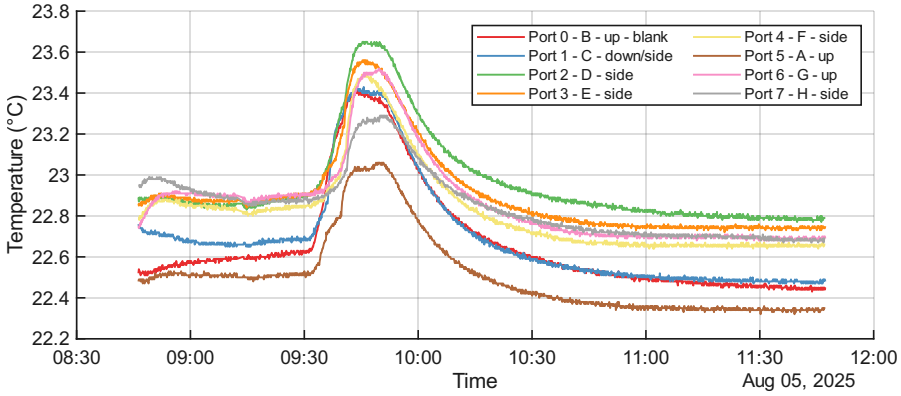

(c) Temperature during Batch 6.

Figure A.7: VOC and environmental sensor responses during Batch 6. All plots share the same time scale.

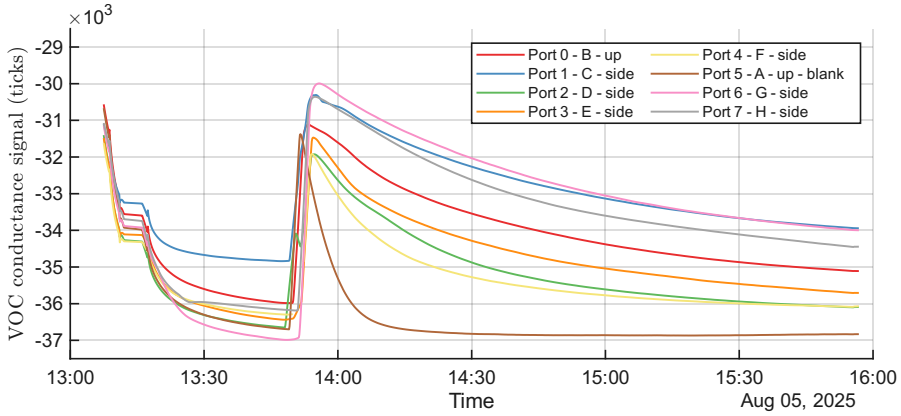

(a) VOC sensor responses during Batch 7.

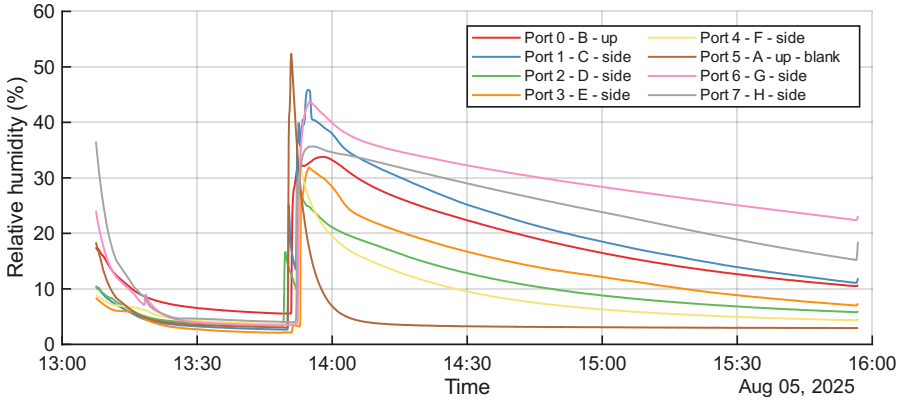

(b) Humidity during Batch 7.

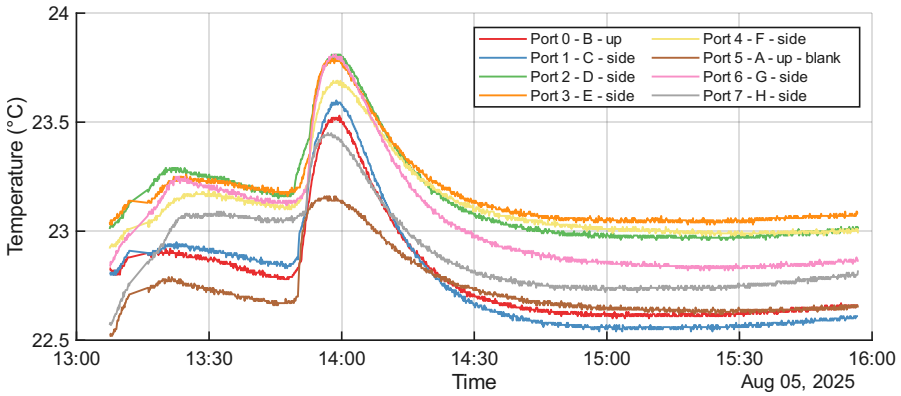

(c) Temperature during Batch 7.

Figure A.8: VOC and environmental sensor responses during Batch 7. All plots share the same time scale.

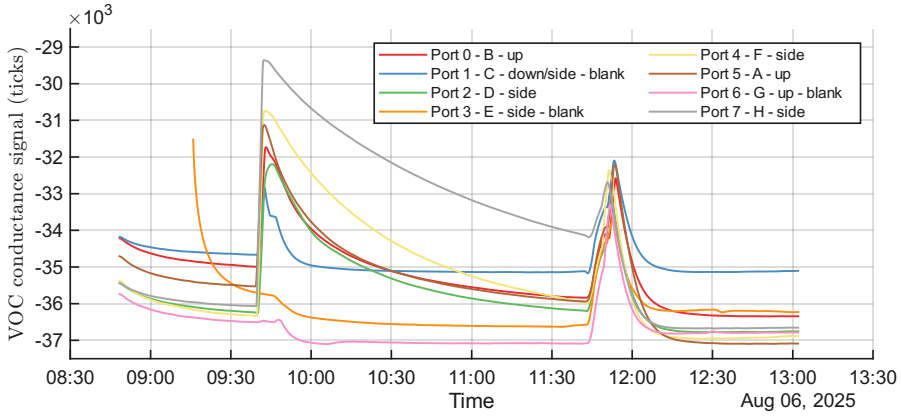

(a) VOC sensor responses during Batch 8.

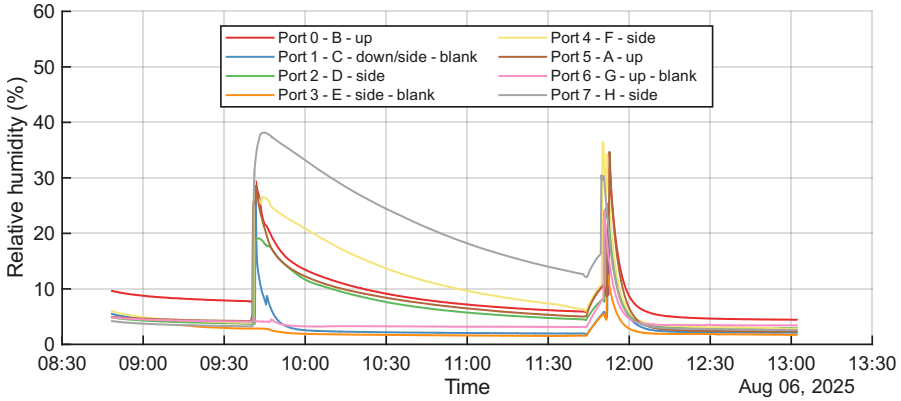

(b) Humidity during Batch 8.

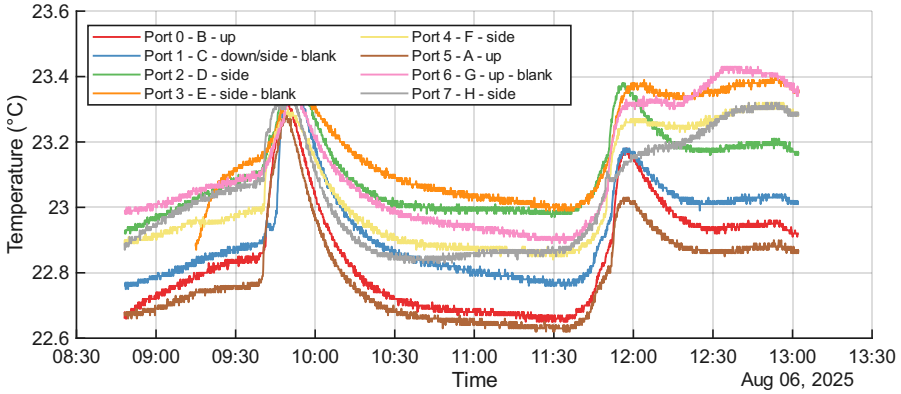

(c) Temperature during Batch 8.

Figure A.9: VOC and environmental sensor responses during Batch 8. All plots share the same time scale.

Appendix B

Data Acquisition codebase

B.1 main.c

```c
#include <stdio.h>
#include <stdlib.h>
#include <string.h>
#include <time.h>
#include <sys/stat.h>
#include <sys/types.h>

#include "libraries/sensirion_common.h"
#include "libraries/sensirion_i2c.h"
#include "libraries/sensirion_i2c_hal.h"
#include "libraries/sgp40_i2c.h"
#include "libraries/sht3x_i2c.h"
#include "libraries/VOC_essentials.h"

#define LOG_DIR "../logs"

int main(int argc, char* argv[]) {
    char filename[128];
    char timestamp[32];

    // Generate timestamp for filename
    time_t now = time(NULL);
    struct tm* t = localtime(&now);
    strftime(timestamp, sizeof(timestamp), "%Y-%m-%d_%H-%M-%S", t);

    if (argc >= 2) {
        snprintf(filename, sizeof(filename), "%s/%s_%s.csv", LOG_DIR,
    argv[1], timestamp);
    } else {
```

```
29          snprintf(filename, sizeof(filename), "%s/log_%s.csv", LOG_DIR
    , timestamp);
30      }
31
32      int oversample_count = 5;
33      float sht31_humidity_offset = 0;
34
35      if (read_config(&oversample_count, &sht31_humidity_offset) != 0)
    {
36          printf("Using default config: oversample_count = %d,
    humidity_offset = %.2f\n", oversample_count, sht31_humidity_offset
    );
37      } else {
38          printf("Loaded config: oversample_count = %d, humidity_offset
     = %.2f\n", oversample_count, sht31_humidity_offset);
39      }
40
41      mkdir(LOG_DIR, 0755);
42
43      FILE* logfile = fopen(filename, "a");
44      if (!logfile) {
45          perror("Failed to open log file");
46          return 1;
47      }
48
49      // Write CSV header if file is empty
50      fseek(logfile, 0, SEEK_END);
51      if (ftell(logfile) == 0) {
52          fprintf(logfile, "Timestamp");
53          for (int i = 0; i < MAX_PORTS; i++) {
54              fprintf(logfile, ",T%d,H%d,VOC%d", i, i, i);
55          }
56          fprintf(logfile, "\n");
57      }
58
59      sensirion_i2c_hal_init();
60      sht3x_init(SHT31_I2C_ADDR_44);
61      mux_init_address(TCA_ADDR_70);
62
63      SensorAccumulator accum[MAX_PORTS];
64      reset_accumulators(accum);
65
66      while (1) {
67          for (int i = 0; i < oversample_count; i++) {
68              sample_all_ports(accum, sht31_humidity_offset);
69              sensirion_i2c_hal_sleep_usec(1000000); // 1 second delay
    per sample
70          }
71
```

```
72          get_timestamp(timestamp, sizeof(timestamp));
73          finalize_averages(logfile, accum, oversample_count, timestamp
    );
74          reset_accumulators(accum);
75      }
76
77      fclose(logfile);
78      return 0;
79  }
```

B.2 VOC_essential.h

```
1  //
2  // Created by save0 on 02/06/2025.
3  //
4
5  #ifndef VOC_ESSENTIALS_H
6  #define VOC_ESSENTIALS_H
7
8  #include <stdint.h>
9  #include "sensirion_common.h"
10 #include "sensirion_i2c.h"
11 #include "sensirion_i2c_hal.h"
12 #include "sgp40_i2c.h"
13 #include "sht3x_i2c.h"
14
15
16 #endif //VOC_ESSENTIALS_H
17
18
19 #include "stdlib.h"
20 #include "stdio.h"
21 #include "string.h"
22 #include "time.h"
23
24 #define CONFIG_FILE "../config.txt"
25
26 #define MAX_PORTS 8
27
28
29 #define TCA_ADDR_70 0x70
30 #define TCA_ADDR_71 0x71
31 #define TCA_ADDR_72 0x72
32 #define TCA_ADDR_73 0x73
33 #define TCA_ADDR_74 0x74
```

```
34 #define TCA_ADDR_75 0x75
35 #define TCA_ADDR_76 0x76
36 #define TCA_ADDR_77 0x77
37
38 /**
39 * @struct SensorAccumulator
40 * @brief A structure to accumulate sensor readings over multiple
       samples for averaging.
41 *
42 * This structure is used during oversampling to store the running sum
       of sensor readings
43 * and the number of valid samples collected for a given multiplexer
       port.
44 */
45 typedef struct {
46     float temp_sum;          /**< Sum of temperature readings (°C). */
47     float hum_sum;           /**< Sum of humidity readings (%RH). */
48     uint32_t voc_sum;        /**< Sum of raw VOC signal readings (ticks
       ). */
49     int sample_count;        /**< Number of valid samples accumulated.
       */
50 } SensorAccumulator;
51
52 /**
53 *  mux_init_address() - This function select the  of the multiplexer
       to use in following functions
54 *
55 *  @param mux_addr is the multiplexer address in the format 0xXX
56 *
57 */
58 void mux_init_address(uint8_t mux_addr);
59
60 /**
61 * mux_port_select() - This command selects one of the eight port of
       the multiplexer for i2c communication
62 *
63 * @param mux_port Port of the multiplexer to select (from 0 to 7)
64 *
65 * @return 0 on success, an error code otherwise
66 */
67 int16_t mux_port_select(uint8_t mux_port);
68
69 /**
70 * mux_i2c_detect() - This command scans the i2c addresses range and
       returns 0 if it detects any device other
71 * than the multiplexer
72 *
73 * @return 0 on success, 1 otherwise
74 */
```

```
75 int16_t mux_i2c_detect ();
76
77 /**
78 * get_timestamp() - This command saves the current time in a string
     buffer
79 *
80 * @param buffer String buffer where to save the time stamp
81 *
82 * @param size Size of buffer
83 */
84 void get_timestamp(char* buffer, size_t size);
85
86 /**
87 * read_config() - Reads configuration values from a file.
88 *
89 * This function reads two parameters from a configuration file:
90 *  - The oversampling count, which determines how many individual
     measurements are averaged.
91 *  - The humidity offset, which is used to correct sensor readings.
92 *
93 * @param oversample_count Pointer to an integer where the read
     oversampling count will be stored.
94 * @param humidity_offset Pointer to a float where the read humidity
     offset (in %) will be stored.
95 *
96 * @return 0 on success, -1 if the configuration file is not found or
     cannot be read.
97 */
98 int read_config(int* oversample_count, float* humidity_offset);
99
100
101 /**
102 *
103 * @param oversample_count Oversampling factor so that T_sampling =
     oversample_count*1s
104 * @param sht31_humidity_offset Offset for humidity measure
105 * @param avg_temp
106 * @param avg_hum
107 * @param avg_raw_voc
108 * @return
109 */
110 int16_t measure_oversampled(int oversample_count, float
     sht31_humidity_offset, float * avg_temp, float * avg_hum, uint16_t
      * avg_raw_voc );
111
112 /**
113 * single_measure() - Performs a single sensor measurement for
     temperature, humidity, and VOC.
114 *
```

```
115 * This function reads temperature and humidity from the SHT31,
        applies the humidity offset,
116 * and then measures raw VOC signal using the SGP40, providing the
        corrected humidity and temperature.
117 *
118 * @param humidity Pointer to float where the corrected humidity (%RH)
        will be stored.
119 * @param temperature Pointer to float where the measured temperature
        (°C) will be stored.
120 * @param raw_voc Pointer to uint16_t where the measured raw VOC
        signal (ticks) will be stored.
121 * @param humidity_offset Offset in %RH applied to humidity for VOC
        compensation.
122 *
123 * @return 0 on success, error code if measurement fails.
124 */
125 int16_t single_measure(float* humidity, float* temperature, uint16_t*
        raw_voc, float humidity_offset);
126
127
128 /**
129 * sample_all_ports() - Performs one measurement per active sensor
        port and stores results in accumulators.
130 *
131 * This function loops over all multiplexer ports, selects each sensor
        , performs a single measurement,
132 * and accumulates the results (temperature, humidity, VOC) for later
        averaging.
133 *
134 * @param accum Array of SensorAccumulator structures used to collect
        and sum measurements for each port.
135 * @param humidity_offset Offset in %RH applied to humidity readings.
136 */
137 void sample_all_ports(SensorAccumulator accum[], float
        humidity_offset);
138
139
140 /**
141 * finalize_averages() - Computes final averages and writes them to
        the logfile.
142 *
143 * This function calculates the average temperature, humidity, and VOC
        values for each port
144 * using the accumulated sums and writes a formatted CSV line to the
        logfile.
145 *
146 * @param logfile File pointer to the CSV log file.
147 * @param accum Array of SensorAccumulator structures containing
        summed data.
```

```
148 * @param oversample_count Number of measurements accumulated (used
        for averaging).
149 * @param timestamp Current timestamp string to prefix the CSV line.
150 */
151 void finalize_averages(FILE* logfile, SensorAccumulator accum[], int
        oversample_count, const char* timestamp);
152
153
154 /**
155 * reset_accumulators() - Resets the measurement accumulators for all
        ports.
156 *
157 * This function sets the sum and count fields of each
        SensorAccumulator to zero,
158 * preparing them for a new round of oversampling.
159 *
160 * @param accum Array of SensorAccumulator structures to reset.
161 */
162 void reset_accumulators(SensorAccumulator accum[]);
```

B.3 VOC_essentials.c

```
1  #include "VOC_essentials.h"
2  #include "sensirion_i2c_hal.h"
3  #include <stdio.h>
4  #include <time.h>
5
6  static uint8_t _mux_addr;
7
8  void mux_init_address(uint8_t mux_addr) {
9      _mux_addr = mux_addr;
10 }
11
12 int16_t mux_port_select(uint8_t mux_port) {
13     if (mux_port > 7) return 1;
14     uint8_t data = 1 << mux_port;
15     return sensirion_i2c_hal_write(_mux_addr, &data, 1);
16 }
17
18 int16_t mux_i2c_detect() {
19     for (uint8_t addr = 0; addr <= 127; addr++) {
20         if (addr == _mux_addr) continue;
21         if (sensirion_i2c_hal_write(addr, NULL, 0) == 0) {
22             return 0; // Device detected
23         }
```

```
    }
    return 1; // No devices found
}

void get_timestamp(char* buffer, size_t size) {
    time_t now = time(NULL);
    strftime(buffer, size, "%Y-%m-%dT%H:%M:%S", localtime(&now));
}

int read_config(int* oversample_count, float* humidity_offset) {
    FILE* config_file = fopen(CONFIG_FILE, "r");
    if (!config_file) {
        fprintf(stderr, "Config file not found. Using defaults.\n");
        return -1;
    }

    char line[128];
    while (fgets(line, sizeof(line), config_file)) {
        char key[64], value[64];
        if (line[0] == '\0' || line[0] == '#') continue;
        if (sscanf(line, "%63s = %63s", key, value) == 2) {
            if (strcmp(key, "oversample_count") == 0) {
                *oversample_count = atoi(value);
                if (*oversample_count <= 0) *oversample_count = 5;
            } else if (strcmp(key, "humidity_offset") == 0) {
                *humidity_offset = atof(value);
                if (*humidity_offset < 0) *humidity_offset = 0;
            }
        }
    }

    fclose(config_file);
    return 0;
}

int16_t measure_oversampled(int oversample_count, float
    humidity_offset, float* avg_temp, float* avg_hum, uint16_t*
    avg_raw_voc) {
    float temp_sum = 0, hum_sum = 0;
    unsigned int voc_sum = 0;
    int16_t error = 0;

    for (int i = 0; i < oversample_count; i++) {
        float t = 0, h = 0;
        uint16_t voc = 0;
        error = single_measure(&h, &t, &voc, humidity_offset);
        sensirion_i2c_hal_sleep_usec(1000000);
        if (error) return error;

```

```
71          temp_sum += t;
72          hum_sum += h;
73          voc_sum += voc;
74      }
75
76      *avg_temp = temp_sum / oversample_count;
77      *avg_hum = hum_sum / oversample_count;
78      *avg_raw_voc = voc_sum / oversample_count;
79
80      return 0;
81  }
82
83  int16_t single_measure(float* humidity, float* temperature, uint16_t*
        raw_voc, float humidity_offset) {
84      uint16_t h_ticks = 0, t_ticks = 0;
85      int16_t error = sht3x_measure_single_shot(REPEATABILITY_HIGH,
        false, &t_ticks, &h_ticks);
86      if (error != NO_ERROR) return error;
87
88      h_ticks += (uint16_t)((humidity_offset * 65535.0f) / 100.0f);
89
90      *humidity = signal_humidity(h_ticks);
91      *temperature = signal_temperature(t_ticks);
92
93      error = sgp40_measure_raw_signal(h_ticks, t_ticks, raw_voc);
94      return error;
95  }
96
97  void sample_all_ports(SensorAccumulator accum[], float
        humidity_offset) {
98      for (int port = 0; port < MAX_PORTS; port++) {
99          mux_port_select(port);
100
101         if (!mux_i2c_detect()) {
102             float t = 0, h = 0;
103             uint16_t voc = 0;
104             if (single_measure(&h, &t, &voc, humidity_offset) == 0) {
105                 accum[port].temp_sum += t;
106                 accum[port].hum_sum += h;
107                 accum[port].voc_sum += voc;
108                 accum[port].sample_count++;
109
110                 printf("Port %d | Temp: %.2f °C | Humidity: %.2f %% |
        VOC: %u ticks\n", port, t, h, voc);
111             }
112         }
113     }
114 }
115
```

```
116 void finalize_averages(FILE* logfile, SensorAccumulator accum[], int
    oversample_count, const char* timestamp) {
117     char csv_row[1024] = "";
118     snprintf(csv_row, sizeof(csv_row), "%s", timestamp);
119 
120     for (int port = 0; port < MAX_PORTS; port++) {
121         if (accum[port].sample_count == oversample_count) {
122             float avg_temp = accum[port].temp_sum / oversample_count;
123             float avg_hum = accum[port].hum_sum / oversample_count;
124             uint16_t avg_voc = accum[port].voc_sum / oversample_count
    ;
125 
126             snprintf(csv_row + strlen(csv_row), sizeof(csv_row) -
    strlen(csv_row),
127                 ",%.2f,%.2f,%u", avg_temp, avg_hum, avg_voc);
128         } else {
129             snprintf(csv_row + strlen(csv_row), sizeof(csv_row) -
    strlen(csv_row), ",NaN,NaN,NaN");
130         }
131     }
132 
133     fprintf(logfile, "%s\n", csv_row);
134     fflush(logfile);
135 }
136 
137 void reset_accumulators(SensorAccumulator accum[]) {
138     for (int i = 0; i < MAX_PORTS; i++) {
139         accum[i] = (SensorAccumulator){0};
140     }
141 }
142 
```

B.4 Useful functions from Sensirion's libraries

B.4.1 sgp40_i2c.c

```
1 int16_t sgp40_measure_raw_signal(uint16_t relative_humidity,
2 uint16_t temperature, uint16_t* sraw_voc) {
3     int16_t error;
4     uint8_t buffer[8];
5     uint16_t offset = 0;
6     offset = sensirion_i2c_add_command_to_buffer(&buffer[0], offset,
    0x260F);
7 
8     offset = sensirion_i2c_add_uint16_t_to_buffer(&buffer[0], offset,
```

```
9       relative_humidity);
10      offset =
11      sensirion_i2c_add_uint16_t_to_buffer(&buffer[0], offset,
        temperature);
12
13      error = sensirion_i2c_write_data(SGP40_I2C_ADDRESS, &buffer[0],
        offset);
14      if (error) {
15          return error;
16      }
17
18      sensirion_i2c_hal_sleep_usec(30000);
19
20      error = sensirion_i2c_read_data_inplace(SGP40_I2C_ADDRESS, &
        buffer[0], 2);
21      if (error) {
22          return error;
23      }
24      *sraw_voc = sensirion_common_bytes_to_uint16_t(&buffer[0]);
25      return NO_ERROR;
26  }
```

B.4.2 sht31_i2c.c

```
1   int16_t sht3x_measure_single_shot(repeatability
        measurement_repeatability,
2   bool is_clock_stretching,
3   uint16_t* a_temperature, uint16_t* a_humidity) {
4       uint16_t raw_temp = 0;
5       uint16_t raw_humi = 0;
6       int16_t local_error = 0;
7       if (is_clock_stretching) {
8           if (measurement_repeatability == REPEATABILITY_HIGH) {
9               local_error =
10
        sht3x_measure_single_shot_high_repeatability_clock_stretching(
11              &raw_temp, &raw_humi);
12              if (local_error != NO_ERROR) {
13                  return local_error;
14              }
15          } else if (measurement_repeatability == REPEATABILITY_MEDIUM)
        {
16              local_error =
17
        sht3x_measure_single_shot_medium_repeatability_clock_stretching(
18              &raw_temp, &raw_humi);
```

```
19              if (local_error != NO_ERROR) {
20                  return local_error;
21              }
22          } else if (measurement_repeatability == REPEATABILITY_LOW) {
23              local_error =
24
    sht3x_measure_single_shot_low_repeatability_clock_stretching(
25                  &raw_temp, &raw_humi);
26              if (local_error != NO_ERROR) {
27                  return local_error;
28              }
29          }
30      } else if (measurement_repeatability == REPEATABILITY_HIGH) {
31          local_error =
32          sht3x_measure_single_shot_high_repeatability(&raw_temp, &
    raw_humi);
33          if (local_error != NO_ERROR) {
34              return local_error;
35          }
36      } else if (measurement_repeatability == REPEATABILITY_MEDIUM) {
37          local_error = sht3x_measure_single_shot_medium_repeatability
    (&raw_temp,
38              &raw_humi);
39          if (local_error != NO_ERROR) {
40              return local_error;
41          }
42      } else if (measurement_repeatability == REPEATABILITY_LOW) {
43          local_error =
44          sht3x_measure_single_shot_low_repeatability(&raw_temp, &
    raw_humi);
45          if (local_error != NO_ERROR) {
46              return local_error;
47          }
48      }
49      *a_temperature = raw_temp;
50      *a_humidity = raw_humi;
51      return local_error;
52  }
```

Appendix C

Data Processing scripts

C.1 analyze_wool_batches.m

```
clear variables
close all
clc

%% Credit
% Line color palette:
% Jonathan C. Lansey (2025). Beautiful and distinguishable line colors + colormap
% (https://www.mathworks.com/matlabcentral/fileexchange/42673-beautiful-and-distinguishable-line-colors-colormap),
% MATLAB Central File Exchange. Retrieved July 25, 2025.

%% General settings

% Output folder for figures (created if it does not exist)
outDir = fullfile(pwd, 'Figures_wool');
if ~exist(outDir, 'dir')
    mkdir(outDir);
end

% Moving-average window length (samples)
wind_length = 20;

%% Loop over experiments (wool batches)

num_ex = 9;

for ex = 1:num_ex

```

```
28      %% Select CSV file and port mapping for this experiment
29      switch ex
30          case 1
31              % 22 July - morning
32              filename        = 'exp_1_2025-07-22_10-29-42.csv';
33              experimentLabel = 'Batch 1 - 2025-07-22 - morning';
34              portTypeMap = containers.Map( ...
35                  {0, 1, 2, 3, 4, 5, 6, 7}, ...
36                  {'F', 'G', 'NC', 'C', 'D', 'H', 'A', 'B'} );
37
38          case 2
39              % 22 July - afternoon (retake)
40              filename        = 'exp_1_retake_2025-07-22_14-08-16.
    csv';
41              experimentLabel = 'Batch 1 retake - 2025-07-22 -
    afternoon';
42              portTypeMap = containers.Map( ...
43                  {0, 1, 2, 3, 4, 5, 6, 7}, ...
44                  {'E', 'F', 'NC', 'D', 'C', 'G', 'B', 'A'} );
45
46          case 3
47              % 23 July - morning
48              filename        = 'exp_2_2025-07-23_09-27-24.csv';
49              experimentLabel = 'Batch 2 - 2025-07-23 - morning';
50              portTypeMap = containers.Map( ...
51                  {0, 1, 2, 3, 4, 5, 6, 7}, ...
52                  {'F', 'G', 'NC', 'D', 'E', 'H', 'A', 'B'} );
53
54          case 4
55              % 29 July - afternoon
56              filename        = 'exp_3_2025-07-29_12-54-31.csv';
57              experimentLabel = 'Batch 3 - 2025-07-29 - afternoon';
58              portTypeMap = containers.Map( ...
59                  {0, 1, 2, 3, 4, 5, 6, 7}, ...
60                  {'G', 'F', 'D', 'E', 'C', 'H', 'A', 'B'} );
61
62          case 5
63              % 30 July - morning
64              filename        = 'exp_4_2025-07-30_09-30-36.csv';
65              experimentLabel = 'Batch 4 - 2025-07-30 - morning';
66              portTypeMap = containers.Map( ...
67                  {0, 1, 2, 3, 4, 5, 6, 7}, ...
68                  {'G - up', 'F - down', 'D - side', ...
69                   'E - side - blank', 'C - down', 'H - down', ...
70                   'A - up', 'B - up'} );
71
72          case 6
73              % 30 July - afternoon (clean air reference)
74              filename        = 'clean_air_2025-07-30_12-58-23.csv';
```

```
75            experimentLabel = 'Batch 5 - 2025-07-30 - afternoon';
76            portTypeMap = containers.Map( ...
77                {0, 1, 2, 3, 4, 5, 6, 7}, ...
78                {'G - up', 'F - down', 'E - side - blank', ...
79                 'D - side', 'C - down', 'H - down', ...
80                 'A - up', 'B - up'} );
81
82        case 7
83            % 5 August - morning: concatenate two files into a
    single CSV
84            data1 = readtable('exp_6_2025-08-05_08-46-10.csv');
85            data2 = readtable('exp_6_continue_2025-08-05_09-13-39.
    csv');
86
87            data_combined = [data1; data2];
88
89            % Sort by timestamp if the column exists
90            if any(strcmp('Timestamp', data_combined.Properties.
    VariableNames))
91                data_combined = sortrows(data_combined, 'Timestamp
    ');
92            end
93
94            % Save the combined file locally
95            filename_combined = 'exp_6.csv';
96            writetable(data_combined, filename_combined);
97
98            filename        = filename_combined;
99            experimentLabel = 'Batch 6 - 2025-08-05 - morning';
100           portTypeMap = containers.Map( ...
101               {0, 1, 2, 3, 4, 5, 6, 7}, ...
102               {'B - up - blank', 'C - down/side', 'D - side ',
    ...
103                'E - side', 'F - side', 'A - up', ...
104                'G - up', 'H - side'} );
105
106       case 8
107           % 5 August - afternoon: concatenate two files into a
    single CSV
108           data1 = readtable('exp_7_2025-08-05_13-07-23.csv');
109           data2 = readtable('exp_7_continue_2025-08-05_13-16-00.
    csv');
110
111           data_combined = [data1; data2];
112
113           % Sort by timestamp if the column exists
114           if any(strcmp('Timestamp', data_combined.Properties.
    VariableNames))
```

```
115                 data_combined = sortrows(data_combined, 'Timestamp
    ');
116             end
117
118             % Save the combined file locally
119             filename_combined = 'exp_7.csv';
120             writetable(data_combined, filename_combined);
121
122             filename        = filename_combined;
123             experimentLabel = 'Batch 7 - 2025-08-05 - afternoon';
124             portTypeMap = containers.Map( ...
125                 {0, 1, 2, 3, 4, 5, 6, 7}, ...
126                 {'B - up ', 'C - side', 'D - side ', ...
127                  'E - side', 'F - side', 'A - up - blank', ...
128                  'G - side', 'H - side'} );
129
130         case 9
131             % 6 August - morning (continuation of exp_8)
132             % filename = 'exp_8_2025-08-05_16-22-10.csv';
133             filename        = 'exp_8_continue_2025-08-06_08-47-59.
    csv';
134             experimentLabel = 'Batch 8 - 2025-08-06 - morning';
135             portTypeMap = containers.Map( ...
136                 {0, 1, 2, 3, 4, 5, 6, 7}, ...
137                 {'B - up', 'C - down/side - blank', 'D - side ',
    ...
138                  'E - side - blank', 'F - side', 'A - up', ...
139                  'G - up - blank', 'H - side'} );
140     end
141
142     %% Read CSV data
143
144     data = readtable(filename, "Delimiter", ',');
145
146     % Convert timestamp to datetime
147     data.Timestamp = datetime( ...
148         data.Timestamp, ...
149         'InputFormat', 'yyyy-MM-dd''T''HH:mm:ss');
150
151     %% Extract number of ports from number of columns
152
153     % 1 column for Timestamp, then triplets T / H / VOC per port
154     numPorts = (width(data) - 1) / 3;
155
156     %% Prepare arrays for easier handling
157
158     Temps   = NaN(height(data), numPorts);
159     Hums    = NaN(height(data), numPorts);
160     VOC_res = NaN(height(data), numPorts);
```

```
161
162     for p = 0:(numPorts-1)
163         tempCol = sprintf('T%d',   p);
164         humCol  = sprintf('H%d',   p);
165         vocCol  = sprintf('VOC%d', p);
166
167         if ismember(tempCol, data.Properties.VariableNames)
168             Temps(:, p+1) = data.(tempCol);
169         end
170         if ismember(humCol, data.Properties.VariableNames)
171             Hums(:, p+1) = data.(humCol);
172         end
173         if ismember(vocCol, data.Properties.VariableNames)
174             VOC_res(:, p+1) = data.(vocCol);
175         end
176     end
177
178     %% Convert VOC resistance to (logarithmic) conductance and
    smooth signals
179
180     % According to the manufacturer, VOC ticks are proportional to
     log(R).
181     % Conductance is proportional to 1/R, so the signal is
    inverted to obtain
182     % a log-conductance representation, which is visually easier
    to interpret.
183     VOC_cond      = -VOC_res;
184     VOC_cond_mean = NaN(size(VOC_cond));
185     Hums_mean     = NaN(size(Hums));
186     Temps_mean    = NaN(size(Temps));
187
188     for p = 1:numPorts
189         VOC_cond_mean(:, p) = movmean(VOC_cond(:, p), wind_length)
    ;
190         Hums_mean(:,     p) = movmean(Hums(:,     p), wind_length)
    ;
191         Temps_mean(:,    p) = movmean(Temps(:,    p), wind_length)
    ;
192     end
193
194     % Precompute colors for all plots in this experiment
195     colors = linspecer(numPorts);
196
197     %% Plot VOC (conductance) from all ports
198
199     figVOC = figure('Name', ['VOC - ', experimentLabel]);
200     hold on;
201     ax = gca;
202     ax.YAxis.Exponent = 3;  % Force labels to be in 1e3 units
```

```
203
204     for p = 1:numPorts
205         if all(isnan(VOC_cond_mean(:, p)))
206             continue; % Skip port with all NaN
207         end
208
209         portLabel = sprintf('Port %d - %s', p-1, portTypeMap(p-1))
    ;
210         plot(data.Timestamp, VOC_cond_mean(:, p), ...
211             'LineWidth', 1.5, ...
212             'Color',     colors(p, :), ...
213             'DisplayName', portLabel);
214     end
215
216     ylim([-3.75e4 -2.85e4]);
217
218     hold off;
219     xlabel('Time');
220     ylabel('VOC conductance signal (ticks)', 'Interpreter', 'latex
    ');
221     title(['VOC conductance over time - ', experimentLabel], '
    Interpreter', 'none');
222
223     ax = gca;
224
225
226
227     % Larger axes for readability
228     ax.FontSize   = 12;
229     ax.LineWidth = 1;
230
231     % Legend style same as thesis
232     lg = legend('Fontsize',10, 'NumColumns', 2, 'Location','best')
    ;
233     set(lg, 'ItemHitFcn', @(src, event) toggleVisibility(event));
234
235
236     grid on
237
238     saveThesisFigure(figVOC, outDir, 'VOC', experimentLabel);
239
240     %% Plot humidity from all ports
241
242     figH = figure('Name', ['Humidity - ', experimentLabel]);
243     hold on;
244
245     for p = 1:numPorts
246         if all(isnan(Hums(:, p)))
247             continue; % Skip port with all NaN
```

```
        end

        portLabel = sprintf('Port %d - %s', p-1, portTypeMap(p-1));
        plot(data.Timestamp, Hums(:, p), ...
            'LineWidth', 1.5, ...
            'Color',     colors(p, :), ...
            'DisplayName', portLabel);
    end

    ylim([0 60]);
    hold off;
    xlabel('Time');
    ylabel('Relative humidity (%)');
    title(['Humidity over time - ', experimentLabel], 'Interpreter', 'none');

     ax = gca;



    % Larger axes for readability
    ax.FontSize  = 12;
    ax.LineWidth = 1;

    % Legend style same as thesis
    lg = legend('Fontsize',10, 'NumColumns', 2, 'Location','best');
    set(lg, 'ItemHitFcn', @(src, event) toggleVisibility(event));

    grid on

    saveThesisFigure(figH, outDir, 'HUM', experimentLabel);

    %% Plot temperature from all ports

    figT = figure('Name', ['Temperature - ', experimentLabel]);
    hold on;

    for p = 1:numPorts
        if all(isnan(Temps(:, p)))
            continue; % Skip port with all NaN
        end

        portLabel = sprintf('Port %d - %s', p-1, portTypeMap(p-1));
        plot(data.Timestamp, Temps(:, p), ...
            'LineWidth', 1.5, ...
            'Color',     colors(p, :), ...
```

```
293             'DisplayName', portLabel);
294     end
295
296     hold off;
297     xlabel('Time');
298     ylabel('Temperature (°C)');
299     title(['Temperature over time - ', experimentLabel], '
    Interpreter', 'none');
300
301      ax = gca;
302
303
304
305     % Larger axes for readability
306     ax.FontSize   = 12;
307     ax.LineWidth = 1;
308
309     % Legend style same as thesis
310     lg = legend('Fontsize',10, 'NumColumns', 2, 'Location','best')
    ;
311     set(lg, 'ItemHitFcn', @(src, event) toggleVisibility(event));
312
313     grid on
314
315     saveThesisFigure(figT, outDir, 'TEMP', experimentLabel);
316
317 end  % for ex = 1:num_ex
```

C.2 induced_voc_processing.m

```
1  clear variables
2  close all
3  clc
4
5  %% Output folder (consistent with other scripts)
6  outDir = fullfile(pwd, 'Figures_inducedVOC');
7  if ~exist(outDir, 'dir')
8      mkdir(outDir);
9  end
10
11 %% General settings
12 wind_length = 20;        % moving-average window length (samples)
13
14 %% Loop over experiments
15
```

```
num_ex = 2;

for ex = 2:num_ex
    %% Select file and port mapping
    switch ex
        case 1
            filename        = 'first_batch_2025-09-16_15-32-17.csv
    ';
            experimentLabel = 'Induced VOC';
            portTypeMap     = containers.Map( ...
                {0, 1, 2, 3, 4, 5, 6, 7}, ...
                {'CM01', 'SpoM01', 'SpoM02', 'CM02', 'SpoM03', '
    CM03', 'SpoM04', 'SpoM05'} );

        case 2
            filename        = 'second_batch_2025-09-17_19-15-38.
    csv';
            experimentLabel = 'Induced VOC experiment 2';
            portTypeMap     = containers.Map( ...
                {0, 1, 2, 3, 4, 5, 6, 7}, ...
                {'CM07', 'SpoM09', 'SpoM08', 'SpoM07', 'CM06', '
    CM05', 'SpoM06', 'CM04'} );
    end

    %% Read data
    data = readtable(filename, "Delimiter", ',');
    data.Timestamp = datetime(data.Timestamp, ...
                              'InputFormat', 'yyyy-MM-dd''T''HH:mm
    :ss');

    %% Number of ports
    numPorts = (width(data) - 1) / 3; % 1 Timestamp + 3 columns
    per port

    %% Identify control vs test ports
    isControl = false(1, numPorts);
    for p = 0:(numPorts-1)
        isControl(p+1) = startsWith(portTypeMap(p), "CM"); %
    controls start with "CM"
    end

    numControls = sum(isControl);
    numTests    = numPorts - numControls;

    %% Color scheme (unchanged: blue for controls, green for tests
    )
    blueBase   = [0 0 1];       % deep blue
    blueLight  = [0.7 0.85 1];  % sky blue
    greenBase  = [0 0.6 0];     % strong green
```

```
    greenLight = [0.7 1 0.7];   % light green

    blueShades  = makeShades(blueBase,  numControls, blueLight);
    greenShades = makeShades(greenBase, numTests,    greenLight);

    colors = zeros(numPorts, 3);
    cIdx = 1; gIdx = 1;
    for p = 0:(numPorts-1)
        if isControl(p+1)
            colors(p+1,:) = blueShades(cIdx,:);
            cIdx = cIdx + 1;
        else
            colors(p+1,:) = greenShades(gIdx,:);
            gIdx = gIdx + 1;
        end
    end

    %% Prepare arrays
    Temps   = NaN(height(data), numPorts);
    Hums    = NaN(height(data), numPorts);
    VOC_res = NaN(height(data), numPorts);

    for p = 0:(numPorts-1)
        tempCol = sprintf('T%d', p);
        humCol  = sprintf('H%d', p);
        vocCol  = sprintf('VOC%d', p);

        if ismember(tempCol, data.Properties.VariableNames)
            Temps(:, p+1) = data.(tempCol);
        end
        if ismember(humCol, data.Properties.VariableNames)
            Hums(:, p+1) = data.(humCol);
        end
        if ismember(vocCol, data.Properties.VariableNames)
            VOC_res(:, p+1) = data.(vocCol);
        end
    end

    %% Convert resistance -> log-conductance & smooth signals
    VOC_cond      = -VOC_res;                       % log-
conductance representation
    VOC_cond_mean = movmean(VOC_cond, wind_length);
    Hums_mean     = movmean(Hums,     wind_length);
    Temps_mean    = movmean(Temps,    wind_length);

    %% Time cut-off: for Batch 1, keep from start until next-day
18:00
    if ex == 1
        startDay   = dateshift(data.Timestamp(1), 'start', 'day');
```

```
104         cutoffTime = startDay + days(1) + hours(18);   % next day
    at 18:00
105         validIdx   = data.Timestamp <= cutoffTime;
106     elseif ex == 2
107         startDay   = dateshift(data.Timestamp(1), 'start', 'day');
108         cutoffTime = startDay + days(1) + hours(18) + minutes(30);
          % next day at 18:00
109         validIdx   = data.Timestamp <= cutoffTime;
110     end
111
112     tUse = data.Timestamp(validIdx);
113
114     %% Markers (unchanged)
115     ctrlMarkers    = {'o','s','^','d','p','h','+','v'};
116     testMarkers    = {'>','*','x','+','s','^','v','<'};
117     numCtrlMarkers = numel(ctrlMarkers);
118     numTestMarkers = numel(testMarkers);
119     numMarkers     = 20;  % markers per line
120
121     %% === VOC (smoothed) ===
122
123     figVOC = figure('Name', ['VOC - ', experimentLabel]);
124     hold on; grid on;
125
126     ax = gca;
127     ax.YAxis.Exponent = 3;
128
129     ctrlIdx = 1;
130     testIdx = 1;
131
132     for p = 1:numPorts
133         if all(isnan(VOC_cond_mean(:, p))), continue; end
134
135         portLabel = sprintf('Port %d - %s', p-1, portTypeMap(p-1))
    ;
136
137         if isControl(p)
138             marker = ctrlMarkers{mod(ctrlIdx-1, numCtrlMarkers)
    +1};
139             ctrlIdx = ctrlIdx + 1;
140         else
141             marker = testMarkers{mod(testIdx-1, numTestMarkers)
    +1};
142             testIdx = testIdx + 1;
143         end
144
145         N = sum(validIdx);
146         markerIdx = round(linspace(1, N, numMarkers));
147
```

```
148         plot(tUse, VOC_cond_mean(validIdx, p), ...
149             'LineWidth', 1.5, ...
150             'Color', colors(p,:), ...
151             'Marker', marker, ...
152             'MarkerIndices', markerIdx, ...
153             'DisplayName', portLabel);
154     end
155 
156     xlabel('Time');
157     ylabel('VOC conductance signal ($ticks$)','Interpreter','latex
    ');
158     title(['VOC conductance signal over time - ', experimentLabel
    ], 'Interpreter','none');
159 
160     ax.FontSize  = 12;
161     ax.LineWidth = 1;
162 
163 % Legend style same as thesis
164 lg = legend('Fontsize',10, 'NumColumns', 2, 'Location','best');
165 set(lg, 'ItemHitFcn', @(src, event) toggleVisibility(event));
166 
167     ylim([-35e3 -30e3]);
168     xlim([tUse(1), cutoffTime]);
169     saveThesisFigure(figVOC, outDir, 'VOC', experimentLabel);
170 
171 
172 
173     %% === Humidity (smoothed) ===
174 
175     figH = figure('Name', ['Humidity - ', experimentLabel]);
176     hold on; grid on;
177 
178     ctrlIdx = 1;
179     testIdx = 1;
180 
181     for p = 1:numPorts
182         if all(isnan(Hums_mean(:, p))), continue; end
183 
184         portLabel = sprintf('Port %d - %s', p-1, portTypeMap(p-1))
    ;
185 
186         if isControl(p)
187             marker = ctrlMarkers{mod(ctrlIdx-1, numCtrlMarkers)
    +1};
188             ctrlIdx = ctrlIdx + 1;
189         else
190             marker = testMarkers{mod(testIdx-1, numTestMarkers)
    +1};
191             testIdx = testIdx + 1;
```

```
192         end
193
194         N = sum(validIdx);
195         markerIdx = round(linspace(1, N, numMarkers));
196
197         plot(tUse, Hums_mean(validIdx, p), ...
198             'LineWidth', 1.5, ...
199             'Color', colors(p,:), ...
200             'Marker', marker, ...
201             'MarkerIndices', markerIdx, ...
202             'DisplayName', portLabel);
203     end
204
205     xlabel('Time');
206     ylabel('Relative humidity (\%)','Interpreter','latex');
207     title(['Humidity signal over time - ', experimentLabel], '
        Interpreter','none');
208     ax = gca;
209     ax.FontSize  = 12;
210     ax.LineWidth = 1;
211
212     lg = legend('Fontsize',10, 'NumColumns', 2, 'Location','south'
        );
213     set(lg, 'ItemHitFcn', @(src, event) toggleVisibility(event));
214
215     xlim([tUse(1), cutoffTime]);   % NEW
216     saveThesisFigure(figH, outDir, 'HUM', experimentLabel);
217
218
219     %% === Temperature (smoothed) ===
220
221     figT = figure('Name', ['Temperature - ', experimentLabel]);
222     hold on; grid on;
223
224     ctrlIdx = 1;
225     testIdx = 1;
226
227     for p = 1:numPorts
228         if all(isnan(Temps_mean(:, p))), continue; end
229
230         portLabel = sprintf('Port %d - %s', p-1, portTypeMap(p-1))
        ;
231
232         if isControl(p)
233             marker = ctrlMarkers{mod(ctrlIdx-1, numCtrlMarkers)
        +1};
234             ctrlIdx = ctrlIdx + 1;
235         else
```

```
236             marker = testMarkers{mod(testIdx-1, numTestMarkers)
    +1};
237             testIdx = testIdx + 1;
238         end
239
240         N = sum(validIdx);
241         markerIdx = round(linspace(1, N, numMarkers));
242
243         plot(tUse, Temps_mean(validIdx, p), ...
244             'LineWidth', 1.5, ...
245             'Color', colors(p,:), ...
246             'Marker', marker, ...
247             'MarkerIndices', markerIdx, ...
248             'DisplayName', portLabel);
249     end
250
251     xlabel('Time');
252     ylabel('Temperature (°C)');
253     title(['Temperature signal over time - ', experimentLabel], '
    Interpreter','none');
254
255     ax = gca;
256     ax.FontSize  = 12;
257     ax.LineWidth = 1;
258
259
260     % Legend style same as thesis
261     lg = legend('Fontsize',10, 'NumColumns', 2, 'Location','best')
    ;
262     set(lg, 'ItemHitFcn', @(src, event) toggleVisibility(event));
263
264
265     saveThesisFigure(figT, outDir, 'TEMP', experimentLabel);
266
267 %% ------------------------------------------
268 %  VOC-only thesis plots with custom time windows for Batches 1 &
    2
269 % ------------------------------------------
270
271 % Determine time window depending on batch
272 if ex == 1
273     % Batch 1: from same-day 08:30 to next-day 18:00
274     dayStart   = dateshift(data.Timestamp(1), 'start', 'day');
275     tStart     = dayStart + days(1) + hours(8) + minutes(30);
276     tEnd       = dayStart + days(1) + hours(18);
277 elseif ex == 2
278     % Batch 2: from 09:30 until end
279     dayStart   = dateshift(data.Timestamp(1), 'start', 'day');
280     tStart     = dayStart + days(1) + hours(9) + minutes(30);
```

```
    tEnd       = data.Timestamp(end);
end

% Mask data
validIdx = (data.Timestamp >= tStart) & (data.Timestamp <= tEnd);
tUse = data.Timestamp(validIdx);

% Create figure
figVOCwin = figure('Name', ['VOC (windowed) - ', experimentLabel]);
hold on; grid on;

ax = gca;
ax.YAxis.Exponent = 3;

% Reset marker counters
ctrlIdx = 1;
testIdx = 1;

for p = 1:numPorts
    if all(isnan(VOC_cond_mean(:, p))), continue; end

    portLabel = sprintf('Port %d - %s', p-1, portTypeMap(p-1));

    % Choose marker
    if isControl(p)
        marker = ctrlMarkers{mod(ctrlIdx-1, numCtrlMarkers)+1};
        ctrlIdx = ctrlIdx + 1;
    else
        marker = testMarkers{mod(testIdx-1, numTestMarkers)+1};
        testIdx = testIdx + 1;
    end

    % Markers evenly spaced in the trimmed window
    N = sum(validIdx);
    markerIdx = round(linspace(1, N, numMarkers));

    % Plot smoothed VOC
    plot(tUse, VOC_cond_mean(validIdx, p), ...
        'LineWidth', 1.5, ...
        'Color', colors(p,:), ...
        'Marker', marker, ...
        'MarkerIndices', markerIdx, ...
        'DisplayName', portLabel);
end

xlabel('Time');
ylabel('VOC conductance signal ($ticks$)','Interpreter','latex');
```

```
328 title(['VOC signal - ', experimentLabel, ' (trimmed window)'], '
    Interpreter','none');
329
330     ylim([-35e3 -30e3]);
331
332
333 % Larger axes for readability
334 ax.FontSize   = 12;
335 ax.LineWidth = 1;
336
337 % Legend style same as thesis
338 lg = legend('Fontsize',10, 'NumColumns', 2, 'Location','best');
339 set(lg, 'ItemHitFcn', @(src, event) toggleVisibility(event));
340
341
342
343 % Export PDF
344 saveThesisFigure(figVOCwin, outDir, 'VOCwindow', experimentLabel);
345
346
347 end % for ex = 1:num_ex
348
349 function shades = makeShades(baseColor, n, lightTint)
350     % Generate n shades between a light tint and the baseColor
351     if n == 1
352         shades = baseColor;
353         return;
354     end
355     shades = zeros(n,3);
356     for i = 1:n
357         t = (i-1)/(n-1); % interpolation fraction
358         shades(i,:) = (1-t)*lightTint + t*baseColor;
359     end
360 end
```

C.3 toggleVisibility.m

```
1 function toggleVisibility(event)
2 % toggleVisibility  Legend click callback to hide/show lines.
3     obj = event.Peer;
4     if strcmp(obj.Visible, 'on')
5         obj.Visible = 'off';
6     else
7         obj.Visible = 'on';
8     end
```

```
end
```

C.4 saveThesisFigure.m

```
function saveThesisFigure(figHandle, outDir, prefix, experimentLabel)
% saveThesisFigure  Save a thesis-styled figure as vector PDF.
%   - wide aspect ratio (good for \linewidth)
%   - normalised fonts and line widths
%   - title removed
%   - small padding so axes are not glued to the edge

    safeLabel = makeFileSafeName(experimentLabel);
    base      = sprintf('%s_%s', prefix, safeLabel);

    % Set figure window ratio: width:height = 2.5 : 1 (tune if needed)
    setFigureRatio(figHandle, 2.5);

    % Normalise axes style
    ax = get(figHandle, 'CurrentAxes');
    if ~isempty(ax)
        ax.FontSize  = 12;
        ax.LineWidth = 1.0;

        lines = findall(ax, 'Type', 'line');
        set(lines, 'LineWidth', 1.2);

        % Remove title for final output
        title(ax, '');
    end

    % Export as vector PDF with a bit of padding
    exportgraphics(figHandle, ...
        fullfile(outDir, [base '.pdf']), ...
        'ContentType', 'vector', ...
        'BackgroundColor', 'white', ...
        'Padding', 0.02);

    close(figHandle);
end

% --- subfunction: only used inside this file ----------------------------
function setFigureRatio(figHandle, ratio)
```

```
39      % ratio = width / height
40      if nargin < 2
41          ratio = 2.5;
42      end
43
44      oldUnits = get(figHandle, 'Units');
45      set(figHandle, 'Units', 'pixels');
46
47      pos = get(figHandle, 'Position');   % [left bottom width
        height]
48      pos(4) = pos(3) / ratio;            % height = width / ratio
49      set(figHandle, 'Position', pos);
50
51      set(figHandle, 'Units', oldUnits);
52  end
53
54  % --- subfunction: only used inside this file
        ----------------------------
55  function safe = makeFileSafeName(label)
56      safe = strtrim(label);
57      safe = strrep(safe, ' ', '_');
58      safe = strrep(safe, '-', '-');      % en dash -> normal dash
59      badChars = '/\:;,*"?''';
60      for k = 1:numel(badChars)
61          safe = strrep(safe, badChars(k), '');
62      end
63  end
```

Bibliography

[1] Siyoung Lee et al. «Wearable Volatile Organic Compound Sensors for Plant Health Monitoring». In: *Advanced Sustainable Systems* 8.9 (2024), p. 2300634. ISSN: 2366-7486. DOI: 10.1002/adsu.202300634. URL: https://onlinelibrary.wiley.com/doi/abs/10.1002/adsu.202300634 (visited on 2025-05-14) (cit. on pp. 1, 15–17, 49).

[2] Vos Rob et al. «The future of food and agriculture». report. Food and Agriculture Organization of the United Nations (FAO), 2017. URL: https://hal.inrae.fr/hal-04567070 (visited on 2025-10-21) (cit. on pp. 1, 49).

[3] *The future of food and agriculture – Drivers and triggers for transformation*. FAO, Dec. 2, 2022. ISBN: 978-92-5-136639-4. DOI: 10.4060/cc0959en. URL: http://www.fao.org/documents/card/en/c/cc0959en (visited on 2025-10-21) (cit. on p. 1).

[4] E.-C. Oerke. «Crop losses to pests». In: *The Journal of Agricultural Science* 144.1 (Feb. 2006), pp. 31–43. ISSN: 0021-8596, 1469-5146. DOI: 10.1017/S0021859605005708. URL: https://www.cambridge.org/core/product/identifier/S0021859605005708/type/journal_article (visited on 2025-10-22) (cit. on p. 1).

[5] Rosario Razo-Belman and César Ozuna. «Volatile Organic Compounds: A Review of Their Current Applications as Pest Biocontrol and Disease Management». In: *Horticulturae* 9.4 (Apr. 2023). Publisher: Multidisciplinary Digital Publishing Institute, p. 441. ISSN: 2311-7524. DOI: 10.3390/horticulturae9040441. URL: https://www.mdpi.com/2311-7524/9/4/441 (visited on 2025-10-21) (cit. on pp. 1, 13, 14, 49).

[6] Harro Bouwmeester, Robert C. Schuurink, Petra M. Bleeker, and Florian Schiestl. «The role of volatiles in plant communication». In: *The Plant Journal* 100.5 (Dec. 2019), pp. 892–907. ISSN: 0960-7412. DOI: 10.1111/tpj.14496. URL: https://www.ncbi.nlm.nih.gov/pmc/articles/PMC6899487/ (visited on 2025-07-04) (cit. on pp. 1, 17).

[7] Dorothea Tholl, Oindrila Hossain, Alexander Weinhold, Ursula S. R. Röse, and Qingshan Wei. «Trends and applications in plant volatile sampling and analysis». In: *The Plant Journal* 106.2 (Apr. 2021), pp. 314–325. ISSN: 0960-7412, 1365-313X. DOI: 10.1111/tpj.15176. URL: https://onlinelibrary.wiley.com/doi/10.1111/tpj.15176 (visited on 2025-05-12) (cit. on pp. 1, 13–17).

[8] Ruchi Sharma, Menglian Zhou, Mark D. Hunter, and Xudong Fan. «Rapid In Situ Analysis of Plant Emission for Disease Diagnosis Using a Portable Gas Chromatography Device». In: *Journal of Agricultural and Food Chemistry* 67.26 (July 3, 2019), pp. 7530–7537. ISSN: 0021-8561, 1520-5118. DOI: 10.1021/acs.jafc.9b02500. URL: https://pubs.acs.org/doi/10.1021/acs.jafc.9b02500 (visited on 2025-05-14) (cit. on p. 1).

[9] Federico Brilli, Francesco Loreto, and Ivan Baccelli. «Exploiting Plant Volatile Organic Compounds (VOCs) in Agriculture to Improve Sustainable Defense Strategies and Productivity of Crops». In: *Frontiers in Plant Science* 10 (Mar. 19, 2019). Publisher: Frontiers. ISSN: 1664-462X. DOI: 10.3389/fpls.2019.00264. URL: https://www.frontiersin.org/journals/plant-science/articles/10.3389/fpls.2019.00264/full (visited on 2025-05-26) (cit. on pp. 2, 10, 16, 17, 47).

[10] Ramasamy Kanagaraj Murali-Baskaran, Palanisamy Mooventhan, Debanjan Das, Anil Dixit, Kailash Chander Sharma, Sengottayan Senthil-Nathan, Pankaj Kaushal, and Probir Kumar Ghosh. «The future of plant volatile organic compounds (pVOCs) research: Advances and applications for sustainable agriculture». In: *Environmental and Experimental Botany* 200 (Aug. 1, 2022), p. 104912. ISSN: 0098-8472. DOI: 10.1016/j.envexpbot.2022.104912. URL: https://www.sciencedirect.com/science/article/pii/S0098847222001344 (visited on 2025-05-14) (cit. on pp. 2, 11, 16, 17).

[11] Ted C. J. Turlings and Felix Wäckers. «Recruitment of predators and parasitoids by herbivore-injured plants». In: *Advances in Insect Chemical Ecology*. Ed. by Ring T. Cardé and Jocelyn G. Millar. 1st ed. Cambridge University Press, June 21, 2004, pp. 21–75. ISBN: 978-0-521-79275-2 978-0-511-54266-4 978-0-521-18893-7. DOI: 10.1017/CBO9780511542664.003. URL: https://www.cambridge.org/core/product/identifier/CBO9780511542664A009/type/book_part (visited on 2025-08-18) (cit. on pp. 2, 15, 16, 41).

[12] Andreas Schütze, Tobias Baur, Martin Leidinger, Wolfhard Reimringer, Ralf Jung, Thorsten Conrad, and Tilman Sauerwald. «Highly Sensitive and Selective VOC Sensor Systems Based on Semiconductor Gas Sensors: How to?» In: *Environments* 4.1 (Mar. 2017). Number: 1 Publisher: Multidisciplinary Digital Publishing Institute, p. 20. ISSN: 2076-3298. DOI: 10.3390/environm

ents4010020. URL: https://www.mdpi.com/2076-3298/4/1/20 (visited on 2025-05-19) (cit. on pp. 2, 11).

[13] Muhammad Khatib and Hossam Haick. «Sensors for Volatile Organic Compounds». In: *ACS Nano* 16.5 (May 24, 2022), pp. 7080–7115. ISSN: 1936-0851, 1936-086X. DOI: 10.1021/acsnano.1c10827. URL: https://pubs.acs.org/doi/10.1021/acsnano.1c10827 (visited on 2025-06-25) (cit. on pp. 2, 10).

[14] Tetsuro Seiyama, Akio Kato, Kiyoshi Fujiishi, and Masanori Nagatani. «A New Detector for Gaseous Components Using Semiconductive Thin Films.» In: *Analytical Chemistry* 34.11 (1962). _eprint: https://doi.org/10.1021/ac60191a001, pp. 1502–1503. DOI: 10.1021/ac60191a001. URL: https://doi.org/10.1021/ac60191a001 (cit. on p. 4).

[15] Nicolae Barsan and Udo Weimar. «Conduction Model of Metal Oxide Gas Sensors». In: *Journal of Electroceramics* 7.3 (Dec. 1, 2001), pp. 143–167. ISSN: 1573-8663. DOI: 10.1023/A:1014405811371. URL: https://doi.org/10.1023/A:1014405811371 (visited on 2025-06-16) (cit. on pp. 4, 6, 8, 19).

[16] Marc J. Madou and Stanley Roy Morrison. *Chemical sensing with solid state devices*. Boston: Academic Press, 1989. ISBN: 978-0-12-464965-1 (cit. on pp. 5, 7, 8, 10, 38).

[17] Neeraj Goel, Kishor Kunal, Aditya Kushwaha, and Mahesh Kumar. «Metal oxide semiconductors for gas sensing». In: *Engineering Reports* 5.6 (June 2023), e12604. ISSN: 2577-8196, 2577-8196. DOI: 10.1002/eng2.12604. URL: https://onlinelibrary.wiley.com/doi/10.1002/eng2.12604 (visited on 2025-05-12) (cit. on pp. 5–7, 9).

[18] Zhijie Li et al. «Advances in designs and mechanisms of semiconducting metal oxide nanostructures for high-precision gas sensors operated at room temperature». In: *Materials Horizons* 6.3 (Mar. 18, 2019). Publisher: The Royal Society of Chemistry, pp. 470–506. ISSN: 2051-6355. DOI: 10.1039/C8MH01365A. URL: https://pubs.rsc.org/en/content/articlelanding/2019/mh/c8mh01365a (visited on 2025-10-09) (cit. on pp. 5, 10).

[19] Digambar Y. Nadargi, Ahmad Umar, Jyoti D. Nadargi, Smita A. Lokare, Sheikh Akbar, Imtiaz S. Mulla, Sharad S. Suryavanshi, Nagesh L. Bhandari, and Manohar G. Chaskar. «Gas sensors and factors influencing sensing mechanism with a special focus on MOS sensors». In: *Journal of Materials Science* 58.2 (Jan. 1, 2023), pp. 559–582. ISSN: 1573-4803. DOI: 10.1007/s10853-022-08072-0. URL: https://doi.org/10.1007/s10853-022-08072-0 (visited on 2025-05-26) (cit. on pp. 6, 7, 9).

[20] Ghenadii Korotcenkov. *Handbook of Gas Sensor Materials: Properties, Advantages and Shortcomings for Applications Volume 2: New Trends and Technologies*. Integrated Analytical Systems. New York, NY: Springer New York, 2014. ISBN: 978-1-4614-7387-9 978-1-4614-7388-6. DOI: 10.1007/978-1-4614-7388-6. URL: http://link.springer.com/10.1007/978-1-4614-7388-6 (visited on 2025-05-26) (cit. on pp. 6–9, 16).

[21] Prem Kumar, Sarita Kataria, Kesavan Subaharan, Mahima Chandel, Bandana Kumari Sahu, Parul Sharma, and Vijayakumar Shanmugam. «Sensing nature's alarm: SnO2/MXene gas sensor unveils methyl jasmonate signatures of plant insect stress». In: *Nanoscale* 16.22 (June 6, 2024). Publisher: The Royal Society of Chemistry, pp. 10675–10681. ISSN: 2040-3372. DOI: 10.1039/D4NR00825A. URL: https://pubs.rsc.org/en/content/articlelanding/2024/nr/d4nr00825a (visited on 2025-06-25) (cit. on pp. 7, 9).

[22] Chaoqi Zhu, Xiang Li, Xiaoxia Wang, Huiyu Su, Chaofan Ma, Xiang Guo, Changsheng Xie, and Dawen Zeng. «Ultrasensitive methyl salicylate gas sensing determined by Pd-doped SnO2». In: *Frontiers of Materials Science* 16.4 (Dec. 23, 2022), p. 220625. ISSN: 2095-0268. DOI: 10.1007/s11706-022-0625-5. URL: https://doi.org/10.1007/s11706-022-0625-5 (visited on 2025-07-17) (cit. on p. 9).

[23] Maximilian Koehne, Christopher Schmidt, Satnam Singh, Andreas Grasskamp, Tilman Sauerwald, and Gina Zeh. «Development of a gas chromatography system coupled to a metal-oxide semiconductor (MOS) sensor, with compensation of the temperature effects on the column for the measurement of ethene». In: *Journal of Sensors and Sensor Systems* 12.2 (Aug. 8, 2023). Publisher: Copernicus GmbH, pp. 215–223. ISSN: 2194-8771. DOI: 10.5194/jsss-12-215-2023. URL: https://jsss.copernicus.org/articles/12/215/2023/ (visited on 2025-07-17) (cit. on p. 9).

[24] Maximilian Koehne, Omar Tarek Penagos Carrascal, Michael Czerny, Gina Zeh, and Tilman Sauerwald. «A versatile development platform for odor monitoring systems». In: *Journal of Sensors and Sensor Systems* 14.1 (May 12, 2025). Publisher: Copernicus GmbH, pp. 75–88. ISSN: 2194-8771. DOI: 10.5194/jsss-14-75-2025. URL: https://jsss.copernicus.org/articles/14/75/2025/ (visited on 2025-09-12) (cit. on pp. 9, 19).

[25] Yannick Robin. «The potential of deep learning for gas sensor evaluation and calibration». PhD thesis. Universität des Saarlandes, 2024. URL: https://publikationen.sulb.uni-saarland.de/handle/20.500.11880/37908 (visited on 2025-07-17) (cit. on pp. 10, 13).

[26] Bingxin Yang, Dung Thi Hanh To, Dagmara Sobolak, Emily Resendiz Mendoza, and Nosang V. Myung. «High performance methyl salicylate gas sensor based on noble metal (Au, Pt) decorated WO3 nanofibers». In: *Sensors and Actuators B: Chemical* 413 (Aug. 2024). Publisher: Elsevier BV, p. 135741. ISSN: 0925-4005. DOI: 10.1016/j.snb.2024.135741. URL: https://linkinghub.elsevier.com/retrieve/pii/S0925400524004702 (visited on 2025-07-17) (cit. on p. 10).

[27] Tobias Baur, Johannes Amann, Caroline Schultealbert, and Andreas Schütze. «Field Study of Metal Oxide Semiconductor Gas Sensors in Temperature Cycled Operation for Selective VOC Monitoring in Indoor Air». In: *Atmosphere* 12.5 (May 19, 2021), p. 647. ISSN: 2073-4433. DOI: 10.3390/atmos12050647. URL: https://www.mdpi.com/2073-4433/12/5/647 (visited on 2025-05-12) (cit. on p. 11).

[28] Radislav A. Potyrailo. «Multivariable Sensors for Ubiquitous Monitoring of Gases in the Era of Internet of Things and Industrial Internet». In: *Chemical Reviews* 116.19 (Oct. 12, 2016), pp. 11877–11923. ISSN: 0009-2665, 1520-6890. DOI: 10.1021/acs.chemrev.6b00187. URL: https://pubs.acs.org/doi/10.1021/acs.chemrev.6b00187 (visited on 2025-06-25) (cit. on p. 11).

[29] Tobias Baur, Caroline Schultealbert, Andreas Schütze, and Tilman Sauerwald. «Device for the detection of short trace gas pulses». In: *tm - Technisches Messen* 85.7 (July 26, 2018), pp. 496–503. ISSN: 2196-7113, 0171-8096. DOI: 10.1515/teme-2017-0137. URL: https://www.degruyter.com/document/doi/10.1515/teme-2017-0137/html (visited on 2025-05-12) (cit. on p. 11).

[30] Tobias Baur, Caroline Schultealbert, Andreas Schütze, and Tilman Sauerwald. «Novel method for the detection of short trace gas pulses with metal oxide semiconductor gas sensors». In: *Journal of Sensors and Sensor Systems* 7.1 (May 28, 2018). Publisher: Copernicus GmbH, pp. 411–419. ISSN: 2194-8771. DOI: 10.5194/jsss-7-411-2018. URL: https://jsss.copernicus.org/articles/7/411/2018/ (visited on 2025-05-12) (cit. on pp. 11, 12).

[31] T. Baur, A. Schütze, and T. Sauerwald. «A4.2 - Detection of short trace gas pulses». In: *Proceedings Sensor 2017* (May 30, 2017), pp. 87–91. DOI: 10.5162/sensor2017/A4.2. URL: https://www.ama-science.org/proceedings/details/2497 (visited on 2025-11-24) (cit. on p. 12).

[32] Maximilian Koehne, Michael Henfling, Kristina Amtmann, Andreas Stenzel, Andrea Buettner, Sabine Trupp, Gina Zeh, and Tilman Sauerwald. «A concept for sensor system developments using raw-milk monitoring as a case study». In: *Journal of Sensors and Sensor Systems* 13.2 (Dec. 11, 2024), pp. 263–275. ISSN: 2194-878X. DOI: 10.5194/jsss-13-263-2024. URL: https://jsss.c

opernicus.org/articles/13/263/2024/ (visited on 2025-05-12) (cit. on pp. 12, 19).

[33] K. Sindelarova et al. «Global data set of biogenic VOC emissions calculated by the MEGAN model over the last 30 years». In: *Atmospheric Chemistry and Physics* 14.17 (Sept. 9, 2014), pp. 9317–9341. ISSN: 1680-7324. DOI: 10.5194/acp-14-9317-2014. URL: https://acp.copernicus.org/articles/14/9317/2014/ (visited on 2025-06-25) (cit. on p. 13).

[34] Werner Jud, J. Barbro Winkler, Bishu Niederbacher, Simon Niederbacher, and Jörg-Peter Schnitzler. «Volatilomics: a non-invasive technique for screening plant phenotypic traits». In: *Plant Methods* 14.1 (Dec. 18, 2018), p. 109. ISSN: 1746-4811. DOI: 10.1186/s13007-018-0378-4. URL: https://doi.org/10.1186/s13007-018-0378-4 (visited on 2025-05-26) (cit. on pp. 14–16).

[35] Alessandra Scala, Silke Allmann, Rossana Mirabella, Michel A. Haring, and Robert C. Schuurink. «Green Leaf Volatiles: A Plant's Multifunctional Weapon against Herbivores and Pathogens». In: *International Journal of Molecular Sciences* 14.9 (Aug. 30, 2013), pp. 17781–17811. ISSN: 1422-0067. DOI: 10.3390/ijms140917781. URL: https://www.ncbi.nlm.nih.gov/pmc/articles/PMC3794753/ (visited on 2025-05-19) (cit. on pp. 14–16).

[36] André Kessler and Ian T. Baldwin. «Defensive Function of Herbivore-Induced Plant Volatile Emissions in Nature». In: *Science* 291.5511 (Mar. 16, 2001), pp. 2141–2144. ISSN: 0036-8075, 1095-9203. DOI: 10.1126/science.291.5511.2141. URL: https://www.science.org/doi/10.1126/science.291.5511.2141 (visited on 2025-06-23) (cit. on p. 14).

[37] Maarten Ameye, Silke Allmann, Jan Verwaeren, Guy Smagghe, Geert Haesaert, Robert C. Schuurink, and Kris Audenaert. «Green leaf volatile production by plants: a meta-analysis». In: *New Phytologist* 220.3 (2018). _eprint: https://onlinelibrary.wiley.com/doi/pdf/10.1111/nph.14671, pp. 666–683. ISSN: 1469-8137. DOI: 10.1111/nph.14671. URL: https://onlinelibrary.wiley.com/doi/abs/10.1111/nph.14671 (visited on 2025-05-12) (cit. on pp. 14, 16).

[38] Ariel Sorg et al. «The airborne herbivore-induced plant volatile indole is converted to benzoxazinoid defense compounds in maize plants». In: *New Phytologist* 246.2 (2025). _eprint: https://nph.onlinelibrary.wiley.com/doi/pdf/10.1111/nph.70004, pp. 718–728. ISSN: 1469-8137. DOI: 10.1111/nph.70004. URL: https://onlinelibrary.wiley.com/doi/abs/10.1111/nph.70004 (visited on 2025-07-09) (cit. on pp. 14, 48).

[39] Sandrine P. Gouinguené and Ted C.J. Turlings. «The Effects of Abiotic Factors on Induced Volatile Emissions in Corn Plants». In: *Plant Physiology* 129.3 (July 1, 2002), pp. 1296–1307. ISSN: 1532-2548, 0032-0889. DOI: 10.1104/pp.001941. URL: https://academic.oup.com/plphys/article/129/3/1296/6110486 (visited on 2025-08-20) (cit. on pp. 15, 17, 47).

[40] Dariusz Piesik, Dariusz Pańka, Kevin J. Delaney, Agata Skoczek, Robert Lamparski, and David K. Weaver. «Cereal crop volatile organic compound induction after mechanical injury, beetle herbivory (*Oulema* spp.), or fungal infection (*Fusarium* spp.)» In: *Journal of Plant Physiology* 168.9 (June 15, 2011), pp. 878–886. ISSN: 0176-1617. DOI: 10.1016/j.jplph.2010.11.010. URL: https://www.sciencedirect.com/science/article/pii/S0176161710005584 (visited on 2025-05-12) (cit. on pp. 15–17).

[41] Ülo Niinemets, Francesco Loreto, and Markus Reichstein. «Physiological and physicochemical controls on foliar volatile organic compound emissions». In: *Trends in Plant Science* 9.4 (Apr. 1, 2004), pp. 180–186. ISSN: 1360-1385. DOI: 10.1016/j.tplants.2004.02.006. URL: https://www.sciencedirect.com/science/article/pii/S1360138504000524 (visited on 2025-08-22) (cit. on pp. 15, 16).

[42] Manuel Lerdau, Alex Guenther, and Russ Monson. «Plant production and emission of volatile organic compounds». In: *Bioscience* 47.6 (June 1997). Num Pages: 11 Place: Oxford, United Kingdom Publisher: Oxford University Press, p. 373. ISSN: 00063568. DOI: 10.2307/1313152. URL: https://www.proquest.com/docview/216464628/citation/A062CA6CF4AE45F7PQ/1 (visited on 2025-06-25) (cit. on p. 16).

[43] Wei Liu, Zhiyao Zhang, Xinliu Geng, Rong Tan, Songzhi Xu, and Lijun Sun. «Electrochemical sensors for plant signaling molecules». In: *Biosensors and Bioelectronics* 267 (Jan. 2025), p. 116757. ISSN: 09565663. DOI: 10.1016/j.bios.2024.116757. URL: https://linkinghub.elsevier.com/retrieve/pii/S0956566324007632 (visited on 2025-07-31) (cit. on pp. 16, 49).

[44] Gianna Vivaldo, Elisa Masi, Cosimo Taiti, Guido Caldarelli, and Stefano Mancuso. «The network of plants volatile organic compounds». In: *Scientific Reports* 7.1 (Sept. 8, 2017). Publisher: Nature Publishing Group, p. 11050. ISSN: 2045-2322. DOI: 10.1038/s41598-017-10975-x. URL: https://www.nature.com/articles/s41598-017-10975-x (visited on 2025-06-25) (cit. on p. 16).

[45] Ted C.J. Turlings and Matthias Erb. «Tritrophic Interactions Mediated by Herbivore-Induced Plant Volatiles: Mechanisms, Ecological Relevance, and Application Potential». In: *Annual Review of Entomology* 63.1 (Jan. 7, 2018). Publisher: Annual Reviews, pp. 433–452. ISSN: 0066-4170, 1545-4487. DOI: 10

.1146/annurev-ento-020117-043507. URL: https://www.annualreviews.org/doi/10.1146/annurev-ento-020117-043507 (visited on 2025-07-11) (cit. on pp. 16, 17, 45, 48, 53).

[46] T. C. J. Turlings, J. H. Tumlinson, and W. J. Lewis. «Exploitation of Herbivore-Induced Plant Odors by Host-Seeking Parasitic Wasps». In: *Science* 250.4985 (Nov. 30, 1990), pp. 1251–1253. ISSN: 0036-8075, 1095-9203. DOI: 10.1126/science.250.4985.1251. URL: https://www.science.org/doi/10.1126/science.250.4985.1251 (visited on 2025-07-01) (cit. on pp. 16, 53).

[47] Jarmo K. Holopainen and Jonathan Gershenzon. «Multiple stress factors and the emission of plant VOCs». In: *Trends in Plant Science* 15.3 (Mar. 1, 2010). Publisher: Elsevier, pp. 176–184. ISSN: 1360-1385. DOI: 10.1016/j.tplants.2010.01.006. URL: https://www.cell.com/trends/plant-science/abstract/S1360-1385(10)00018-X (visited on 2025-08-20) (cit. on p. 17).

[48] Ted C. J. Turlings, Urs B. Lengwiler, Marco L. Bernasconi, and Daniel Wechsler. «Timing of induced volatile emissions in maize seedlings». In: *Planta* 207.1 (Nov. 1, 1998), pp. 146–152. ISSN: 1432-2048. DOI: 10.1007/s004250050466. URL: https://doi.org/10.1007/s004250050466 (visited on 2025-07-17) (cit. on pp. 17, 45, 47, 48, 50).

[49] Mirian F. F. Michereff et al. «Variability in herbivore-induced defence signalling across different maize genotypes impacts significantly on natural enemy foraging behaviour». In: *Journal of Pest Science* 92.2 (Mar. 1, 2019), pp. 723–736. ISSN: 1612-4766. DOI: 10.1007/s10340-018-1033-6. URL: https://doi.org/10.1007/s10340-018-1033-6 (visited on 2025-08-20) (cit. on pp. 17, 47, 48).

[50] Mateus de Souza Sanches, Mirian Fernandes Furtado Michereff, Miguel Borges, Raul Alberto Laumann, Charles Martins de Oliveira, Marina Regina Frizzas, and Maria Carolina Blassioli-Moraes. «How Much, How Long and When: Density, Duration and Plant Stage Affect Herbivore-induced Plant Volatiles in Maize by the Corn Leafhopper». In: *Journal of Chemical Ecology* 51.3 (May 14, 2025), p. 53. ISSN: 1573-1561. DOI: 10.1007/s10886-025-01600-7. URL: https://doi.org/10.1007/s10886-025-01600-7 (visited on 2025-08-20) (cit. on pp. 17, 47).

[51] Marcel Dicke and Ian T. Baldwin. «The evolutionary context for herbivore-induced plant volatiles: beyond the 'cry for help'». In: *Trends in Plant Science* 15.3 (Mar. 1, 2010). Publisher: Elsevier, pp. 167–175. ISSN: 1360-1385. DOI: 10.1016/j.tplants.2009.12.002. URL: https://www.cell.com/trends/plant-science/abstract/S1360-1385(09)00300-8 (visited on 2025-08-22) (cit. on pp. 17, 48).

[52] Andrea Clavijo McCormick, Sybille B. Unsicker, and Jonathan Gershenzon. «The specificity of herbivore-induced plant volatiles in attracting herbivore enemies». In: *Trends in Plant Science* 17.5 (May 1, 2012). Publisher: Elsevier, pp. 303–310. ISSN: 1360-1385. DOI: 10.1016/j.tplants.2012.03.012. URL: https://www.cell.com/trends/plant-science/abstract/S1360-1385(12)00073-8 (visited on 2025-09-25) (cit. on p. 17).

[53] Daniel Rüffer, Felix Hoehne, and Johannes Bühler. «New Digital Metal-Oxide (MOx) Sensor Platform». In: *Sensors* 18.4 (Apr. 2018). Number: 4 Publisher: Multidisciplinary Digital Publishing Institute, p. 1052. ISSN: 1424-8220. DOI: 10.3390/s18041052. URL: https://www.mdpi.com/1424-8220/18/4/1052 (visited on 2025-05-18) (cit. on pp. 19, 30, 38).

[54] Sensirion. *Datasheet SHT3x-DIS*. Version 7. Dec. 2022. URL: https://sensirion.com/media/documents/213E6A3B/63A5A569/Datasheet_SHT3x_DIS.pdf (cit. on p. 19).

[55] Caroline Schultealbert, Johannes Amann, Tobias Baur, and Andreas Schütze. «Measuring Hydrogen in Indoor Air with a Selective Metal Oxide Semiconductor Sensor». In: *Atmosphere* 12.3 (Mar. 2021). Publisher: Multidisciplinary Digital Publishing Institute, p. 366. ISSN: 2073-4433. DOI: 10.3390/atmos12030366. URL: https://www.mdpi.com/2073-4433/12/3/366 (visited on 2025-09-12) (cit. on p. 19).

[56] Sensirion. *Datasheet SGP40*. Version 1.2. Feb. 2022. URL: https://sensirion.com/media/documents/296373BB/6203C5DF/Sensirion_Gas_Sensors_Datasheet_SGP40.pdf (cit. on p. 19).

[57] nilok. *Raspberry Pi Breadboard Case by nilok | Download free STL model*. Printables.com. Creative Commons Attribution-NonCommercial-ShareAlike 4.0 International (CC BY-NC-SA 4.0). Mar. 4, 2020. URL: https://www.printables.com/model/24751-raspberry-pi-breadboard-case (visited on 2025-10-20) (cit. on p. 21).

[58] TheOneTruePatrick. *Lever Wire Connector Mount (Parametric) by TheOneTruePatrick | Download free STL model*. Printables.com. Nov. 6, 2023. URL: https://www.printables.com/model/639009-lever-wire-connector-mount-parametric (visited on 2025-10-20) (cit. on p. 21).

[59] Arjen Lommen. «MetAlign: Interface-Driven, Versatile Metabolomics Tool for Hyphenated Full-Scan Mass Spectrometry Data Preprocessing». In: *Analytical Chemistry* 81.8 (Apr. 15, 2009). Publisher: American Chemical Society, pp. 3079–3086. ISSN: 0003-2700. DOI: 10.1021/ac900036d. URL: https://doi.org/10.1021/ac900036d (visited on 2025-11-27) (cit. on p. 28).

[60] Y. M. Tikunov, S. Laptenok, R. D. Hall, A. Bovy, and R. C. H. de Vos. «MSClust: a tool for unsupervised mass spectra extraction of chromatography-mass spectrometry ion-wise aligned data». In: *Metabolomics* 8.4 (2012), pp. 714–718. ISSN: 1573-3882. DOI: 10.1007/s11306-011-0368-2. URL: https://pmc.ncbi.nlm.nih.gov/articles/PMC3397229/ (visited on 2025-11-27) (cit. on p. 28).

[61] Sensirion. *SGP Design-In Guide*. Aug. 2020. URL: https://sensirion.com/media/documents/C87B1A6C/616452A3/Sensirion_Gas_Sensors_Datasheet_GAS_SGP4x_Design-In_Guide_D1.pdf (cit. on pp. 30, 37).

[62] Paula S. Brok, Stéphanie M. Jost, and Niels O. Verhulst. «Selection of sheep skin bacteria to reduce blood feeding by biting midges under laboratory conditions». In: *Entomologia Experimentalis et Applicata* 172.11 (2024). _eprint: https://onlinelibrary.wiley.com/doi/pdf/10.1111/eea.13503, pp. 1062–1071. ISSN: 1570-7458. DOI: 10.1111/eea.13503. URL: https://onlinelibrary.wiley.com/doi/abs/10.1111/eea.13503 (visited on 2025-08-27) (cit. on p. 39).

[63] A. Skoczek, D. Piesik, A. Wenda-Piesik, B. Buszewski, J. Bocianowski, and M. Wawrzyniak. «Volatile organic compounds released by maize following herbivory or insect extract application and communication between plants». In: *Journal of Applied Entomology* 141.8 (2017). _eprint: https://onlinelibrary.wiley.com/doi/pd pp. 630–643. ISSN: 1439-0418. DOI: 10.1111/jen.12367. URL: https://onlinelibrary.wiley.com/doi/abs/10.1111/jen.12367 (visited on 2025-08-18) (cit. on pp. 45, 47, 54).

[64] André Kessler. «Detecting the enemy or being manipulated by your attacker? Herbivore-derived elicitors of plant responses: an introduction to a Virtual Issue». In: *New Phytologist* 247.2 (2025). _eprint: https://nph.onlinelibrary.wiley.com/doi/pdf pp. 431–435. ISSN: 1469-8137. DOI: 10.1111/nph.70289. URL: https://onlinelibrary.wiley.com/doi/abs/10.1111/nph.70289 (visited on 2025-07-09) (cit. on p. 47).

[65] M. R. Kant et al. «Mechanisms and ecological consequences of plant defence induction and suppression in herbivore communities». In: *Annals of Botany* 115.7 (June 2015), pp. 1015–1051. ISSN: 0305-7364. DOI: 10.1093/aob/mcv054. URL: https://www.ncbi.nlm.nih.gov/pmc/articles/PMC4648464/ (visited on 2025-07-04) (cit. on p. 47).

[66] *Spodoptera littoralis. EPPO datasheets on pests recommended for regulation.* 2025. URL: https://gd.eppo.int (cit. on pp. 47, 48).

[67] Marja van der Straten, Jean-François Germain, and Bart Van de Vossenberg. *PM 7/124 (1) Spodoptera littoralis, Spodoptera litura, Spodoptera frugiperda, Spodoptera eridania*. Vol. 45. Journal Abbreviation: EPPO Bulletin Publication Title: EPPO Bulletin. Dec. 1, 2015. DOI: 10.1111/epp.12258 (cit. on pp. 47, 48).

[68] Kaimei Wang, Shaoyong Ke, Wei Fang, Fang Liu, and Zhigang Zhang. «Agroactive volatile organic compounds from microbes: Chemical diversities and potentials of application in crop protection». In: *Advanced Agrochem* 2.1 (Mar. 2023), pp. 39–57. ISSN: 27732371. DOI: 10.1016/j.aac.2022.12.004. URL: https://linkinghub.elsevier.com/retrieve/pii/S2773237122000491 (visited on 2025-11-26) (cit. on p. 51).

Dedications

Alla mia famiglia, che non ha mai smesso di sostenermi.

A mio padre Giuseppe, per i suoi consigli e la sua saggezza.

A Matilde, per dieci anni di amore, pazienza e felicità